Programming and Sensing with Deep Brain Stimulation Arrays

A Dissertation
SUBMITTED TO THE FACULTY OF
UNIVERSITY OF MINNESOTA
BY

Simeng Zhang

IN PARTIAL FULFILLMENT OF THE REQUIREMENTS
FOR THE DEGREE OF
DOCTOR OF PHILOSOPHY

Advisor: Dr. Matthew D. Johnson

August 2017

Acknowledgements

I would first like to emphasize that the work in this dissertation was a team effort. I could not have done it without the help from my labmates and collaborators.

I would next like to thank all the non-human primates for the contributions and sacrifices they have made for the advancement of science and the well-being of mankind.

I especially would like to thank my advisor: Dr. Matthew D. Johnson for taking me on as a graduate student half way through my PhD process, for believing in me and encouraging me, helping me with my experiments and analyses, and being a wonderful mentor who has taught me about science, engineering, positivity, passion and patience. Coming to your lab was one of the two biggest decisions that I have made in my life (the other one being coming to America), and it turned out to also be the best decision I have made in my life.

I would like to thank my dissertation committee: Dr. Jerrold Vitek, Dr. Hubert Lim, and Dr. Scott Cooper for reading this thesis and offering me suggestions and guidance. It is my pleasure to have some of the brightest minds working in neural engineering and movement disorders be on my committee. Interacting with you at multiple professional and personal settings have not only taught me how to be a good researcher who can integrate works from both the engineering and the clinical perspectives, but also have taught me to how to be a leader and well-rounded human being.

I would also like to thank all of the past and current members of the Neuromodulation Research and Technology Lab, especially: Allison, Ben T., Laura, Joe, Filippo, Edgar, Ed, Logan, Alex, Julia, MariPen, Steve, Jordan, and Kelton, for your help, love and support. Many of you became my coauthors, collaborators, and friends. I enjoyed working with all of you, and I owe part of my success to you.

I would next like to thank the members of the Neuromodulation Research Center: Dr. Baker, Luke, Claudia, Jianyu, Jing, Ying, David, Lexi, Shane, Ben, Michelle, Sinta, Hannah and Leila for your support and friendship and numerous weekend work parties,

and especially Dr. Greg Molnar, for offering me career guidance and helping me with my personal and professional development.

I would like to thank my other collaborators at CMRR: Dr. Noam Harel, Dr. Essa Yacoub, Dr. Gregor Adriany and Dr. Shalom Michaeli; and my previous lab members and collaborators at the VA: Dr. Jim Ashe, Dr. Xiaofeng Lu, Dr. Pat Fahey, Steve, Dean, Dale, Derek, Harris, Rachael, Dr. Matt Chaffee, Dr. Giuseppe Pellizzer. I am thankful to your help and guidance.

I would like to give a special shout-out to many of my closest friends: Katia, Joe, Natha, Ian, Yoko, Mozi, Jing, Zhuoran, Doug, Zaw, Kit, Maggie, Skye, Michelle, Woo, Supriya, Jamie, Pantea, Andrew, and Rachel, who have unconditionally supported me through six years of graduate school, among which were some of the toughest times of my life. I could not imagine how my life would have been without you. I am so honored to have shared many of life's adventures with you, and I want to thank you for making me a better person.

I would like to thank my family: my mom Xuecen Ma and my dad Liming Zhang, who made a sacrifice for sending me to America to chase after my dreams, and for supporting me and loving me; my late grandpas Zhenquan Ma and Naixi Zhang for inspiring my love for biology, science and art; and my grandmas and uncles and aunts and cousins who love me and whom I love deeply.

I would like to give a special thank you to the undergraduate students who have worked under my mentorship: Ben H., Diana, Lauren and Shale. You have brilliant minds, kind hearts, and loads of dedication. My work was made so much easier with your help, and I thank you for it. I have no doubt that you will continue to succeed in work and life, and I hope that I have made a positive impact in your professional and personal development, just like many of my mentors have done for me.

Last, I would like to thank Lana Del Rey for your music. Both the non-human primates and I have enjoyed your talented work.

Dedication

This thesis is dedicated to my family and my friends.

Abstract

Deep brain stimulation (DBS) is a neurosurgical therapy for movement disorders that relies on both precise neurosurgical implantation of a DBS lead of electrodes and systematic optimization (or programming) of stimulation settings to achieve beneficial clinical outcomes. One recent advance to improve the targeting of stimulation is the development of DBS arrays with electrodes segmented both along and around the DBS lead. However, increasing the number of independent electrodes creates the logistical challenge of how to efficiently optimize stimulation parameters to target one or more pathways within the brain. This doctoral dissertation advanced the programming capabilities of DBS arrays by: (1) developing a multi-objective Particle Swarm Optimization (PSO) algorithm to program DBS arrays in the motor thalamus, and (2) investigating the PSO algorithm's capacity to target DBS therapy within the globus pallidus (GP) and subthalamic nucleus (STN) for treating parkinsonian motor signs. With increased numbers of electrodes and decreased inter-electrode spacing, DBS arrays also open up opportunities to record local field potential (LFP) activity with improved spatial resolution, which could expand the feature set of neurophysiological feedback for closed-loop approaches to DBS therapy. This dissertation also (3) investigated the spatial resolution of local field potential (LFP) signals in the GP and STN in both resting state and during an active task in two non-human primates in both naïve and parkinsonian conditions. The primary findings of this dissertation suggest that the PSO algorithm produced solutions with accuracy, robustness, and consistency, and further that the PSO algorithm applied to targeting the STN in a parkinsonian non-human primate showed superior performance in reducing rigidity in comparison to conventional clinical monopolar review settings. Furthermore, it was demonstrated that segmented DBS arrays with higher density and smaller contacts were able to provide more spectral information within both GP and STN than could be sensed using grouped macroelectrode configurations consistent with commercial DBS leads. Together these results suggest that future translation of DBS array technology to the clinical setting will benefit both spatial and temporal optimization of DBS therapy on a patient-specific basis.

Table of Contents

List of Tables

List of Figures

List of Abbreviations

A	Anterior
AR	Augmented reality
CSF	Cerebrospinal fluid
CST_{arm}	Arm representation in the corticospinal tract of the internal capsule
CT	Computerized tomography
DBS	Deep brain stimulation
DBSA	Deep brain stimulation array
EEG	Electroencephalogram
EMG	Electromyography
ET	Essential tremor
FDA	Food and Drug Administration
GP	Globus pallidus
GPe	Globus pallidus externus
GPi	Globus pallidus internus
L	Lateral
LA	Lateral anterior
LFP	Local field potential
LP	Lateral posterior
M	Medial
MA	Medial anterior
MAF	Modified activating function
MAFT	Modified activating function threshold
MP	Medial posterior
MPTP	1-methyl-4-phenyl-1,2,3,6 tetrahydropyridine
MRI	Magnetic resonance imaging
mUPDRS	Modified Unifed Parkinson's Disease Rating Scale
OCD	Obsessive-compulsive disorder
P	Posterior
PD	Parkinson’s disease
PSO	Particle swarm optimization
ROA	Region of activation
ROI	Region of interest
SNc	Substantia nigra pars compacta
SNr	Substantia nigra pars reticulata
STN	Subthalamic nucleus

TTL	Transistor-transistor logic
Vim	Ventral intermediate nucleus
VPLc	Ventral posterolateral pars caudalis
VPLo	Ventral posterolateral pars oralis
VR	Virtual reality

Chapter 1
Introduction

1.1 Background on Parkinson's Disease

Parkinson's disease (PD) is a progressive neurodegenerative disorder that was named after Dr. James Parkinson, who first described the disease as a "shaking palsy" in 1817. PD is the second most common progressive neurodegenerative disorder, affecting 0.1-0.2% of the population worldwide [1]. While traditionally viewed as a movement disorder – given that the most overt symptoms manifest as tremor, bradykinesia, akinesia, rigidity, postural instability, and gait dysfunction – PD also has many non-motor symptoms including olfactory problems, sleep disturbance, autonomic dysfunction, depression, and psychosis [2]. Though the cause of PD remains unclear [3], the pathology of PD is characterized by the appearance of abnormal α-synuclein aggregates in the form of Lewy bodies and Lewy neurites in conjunction with degeneration of neurons within several deep brain targets including dopaminergic neurons within the substantia nigra pars compacta (SNc) [4]. Currently, there are no treatments to slow or stop this disease progression [5,6] although several therapies exist to mitigate the motor signs of PD.

1.2 Background on Deep Brain Stimulation

The earliest attempt to treating PD was pallidotomy and thalamotomy [7,8]. However, these invasive procedures, which have potential for serious side effects if the lesions were made too large or off target, were eventually supplanted by dopamine replacement therapy in the form of levodopa medication. Dopamine replacement therapy still remains the most common treatment for PD; however, after years of exposure to levodopa, patients often

experience significant motor fluctuations and drug-induced dyskinesia [9]. This led to the reexamination of pallidotomy [7] and the experimental use of high frequency electric stimulation to alleviate the motor symptoms of PD [10,11]. In the latter case, passing electric stimulation into deep structures of the brain was referred to as Deep Brain Stimulation, or DBS. Stemming from experience with targeting lesions to the globus pallidus internus (GPi) [12] and the subthalamic nucleus (STN) [13], the GPi and STN were similarly found to be highly effective targets for DBS to treat motor symptoms of PD as well as manage levodopa-induced motor fluctuations and dyskinesia. DBS therapy in comparison to surgical lesions is reversible and adjustable. DBS therapy for PD has been shown to be effective in large-scale clinical studies, including controlled studies [14] and in randomized trials comparing DBS to best medical therapy [15,16].

To date, DBS therapy also has FDA approval for treating essential tremor (ET) [17] and has gained a mark for Humanitarian Devices Exemption status for treating other brain disorders including dystonia [18] and obsessive-compulsive disorder (OCD) [19] in the United States. Currently, DBS is also indicated for other brain disorders in Europe including epilepsy [20]. In terms of treating PD, DBS targets have been extended to the globus pallidus externus (GPe, [21]), pedunculopontine nucleus [22–24], and at the STN–SNr border [25,26]. To date, over 120,000 DBS leads have been implanted in patients suffering from various disorders, and most of these patients have experienced a significant increase in the quality of life after receiving DBS therapy.

1.3 Challenges with DBS Therapy

However, a major challenge with implementing DBS therapy is achieving the desired therapeutic effect without spreading suprathreshold current to other pathways within the brains that elicit side effects when stimulated. The process of DBS therapy typically involves using the Medtronic DBS system model 3387 or model 3389, which consist of a stack of four 1.5 mm tall cylindrical shell electrodes distributed along a 1.27 mm diameter lead with electrode separation of 1.5 mm (model 3387) or 0.5 mm (model 3389). For both

of the DBS leads, stimulation is limited omnidirectionally around the DBS lead, which can be particularly challenging as many of the targets of DBS are non-spherical in shape [27], have complex sub-regions [28–31], and are surrounded by multiple oscillatory networks [32–39]. In the case of targeting the STN for treating PD, for example, activation of corticobulbar tracts on the anterior border can lead to speech impairment, while activating the corticospinal tract on the lateral border can induce sustained muscle contractions [6].

Another key to successful DBS therapy is the accurate electrode placement within the desired target. A stereotactic technique is commonly used to deliver a DBS lead along a preplanned implantation trajectory to the correct depth. High-precision instruments and improved medical imaging aid this process. Yet, due to intra-operative brain shift and operation errors, the end location of the electrodes often deviates from the pre-planned location or trajectory by 1-2 millimeters, resulting in a DBS lead misplacement [40–42]. If a lead displacement is too large, the DBS implantable neurostimulator is not able to provide the desired therapy, and a DBS revision surgery is often performed to explant the original DBS lead and re-implant a new DBS lead along a different trajectory.

In the case of the Medtronic 3387 or 3389 DBS leads, multiple electrodes exist along the implant trajectory, and this provides the opportunity to select the best electrode for stimulation. The optimal electrode and stimulation configuration is selected for a patient initially through a “monopolar review”, where a clinician systematically increases the stimulation amplitude for each electrode while assessing therapeutic effects and side effects. Other stimulation parameters including pulse width and pulse frequency can also be varied. This process is called “programming” the DBS system. The clinician might also explore bipolar settings where multiple electrodes are enabled in anode-cathode configurations if the monopolar review did not yield the desired therapy. This process can require hours of meticulous and tedious trial-and-error evaluation and multiple visits in some cases [43]. In addition, therapeutic effects of DBS might not reach equilibrium immediately, further confounding the programming process [44–46].

1.4 Advancements of DBS Lead Technology

Current steering involves passing various current intensities through multiple electrode simultaneously to sculpt and shape the volume of neuronal tissue activated by stimulation [47]. Current steering could partly mitigate the issues caused by complex target geometry or lead misplacement by guiding the current to the direction of the target of interest while controlling the size of the activation volume. The four cylindrical electrodes in the Medtronic 3387 and 3389 leads offer current steering abilities along the length of the lead; however, there is no flexibility to steer current around the axis of the DBS lead. As such, DBS leads with segmented contacts around the lead circumference and along the length of the lead could further improve current steering [48].

Within the past few years, several DBS lead designs with segmented electrodes have been advanced with either European CE Mark (Boston Cartesia, Abbott 6172) or FDA approval (Abbott 6172) (**Fig. 1.1**). These segmented DBS leads are anticipated to improve patient outcomes by allowing clinicians to better customize stimulation to individual patients and better compensate for suboptimal DBS lead placements.

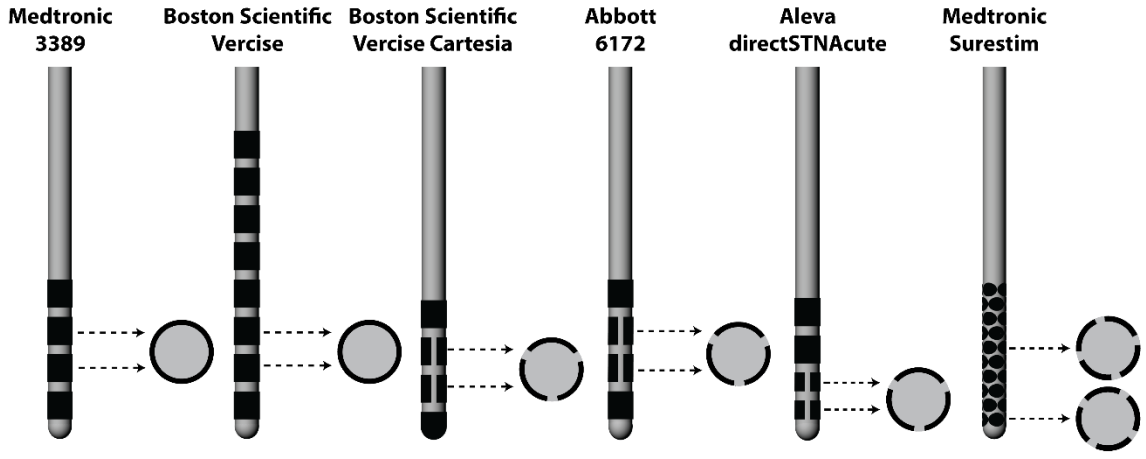

Figure 1.1: *Different design schematics for commercial and investigational DBS leads*

In this dissertation, an investigative DBS array (**Fig. 1.2**) with a narrower diameter (600 µm versus 1.27 mm in the human case) was used in lieu of the commercial DBS leads

[49]. The DBS array contained four columns of electrodes around the axis of the shank and eight rows of electrodes along the shank, resulting in a total of 32 electrodes. This high-density lead design was modeled previously in a computational study [50] and was evaluated previously *in vivo* in proof-of-concept studies in non-human primates [51].

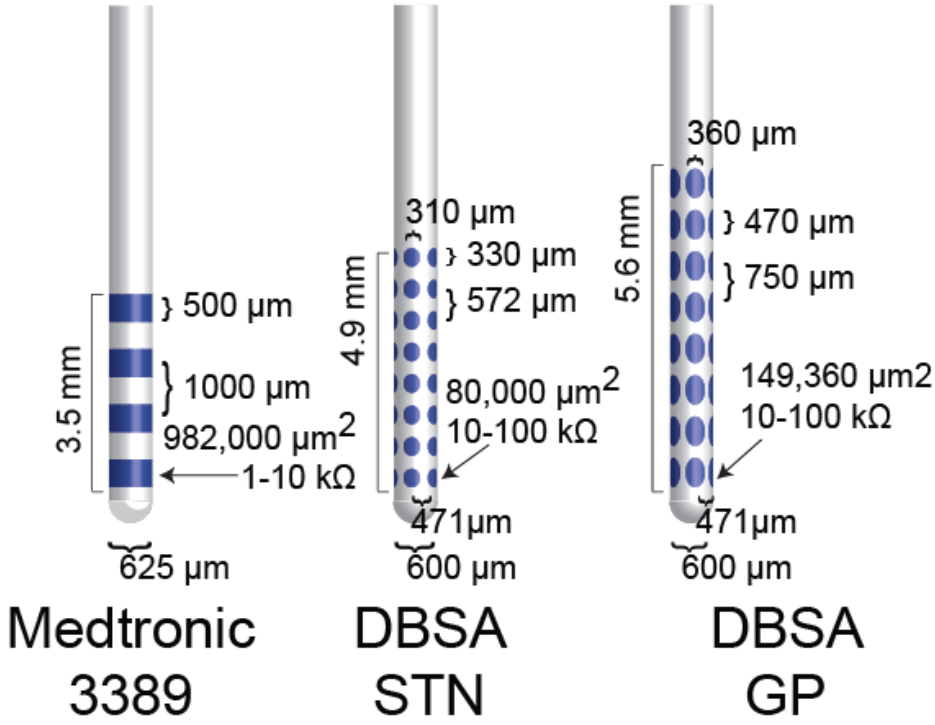

Figure 1.2: *Schematic and dimensions of the DBSAs*

However, with increased number of electrodes and more complex geometry of the segmented DBS leads, the already tedious programming process becomes a significant and costly challenge for clinicians to sift through every combination of monopolar stimulation settings let alone employ current steering techniques that leverage multiple current amplitudes along the DBS array. Thus, for segmented DBS leads, especially leads with higher density electrode arrays (such as the Medtronic Surestim lead or the DBS array used in this dissertation), selection of stimulation parameters will require new approaches. This dissertation advances computational models constructed from principles of volume conductor theory and biophysical axonal cable theory that together simulate neuronal behaviors to electrical perturbations [46,52,53]. Further, to be useful on a subject-specific

basis, the dissertation advances the computational models to fit to patient imaging data [54–57] and couple with efficient algorithms to identify stimulation parameters on a subject-specific basis [55,58].

There have been limited studies that attempt to solve the programming issue. One previous study used a machine-learning approach and trained a classifier on thousands of computational neuron model simulations [59] that were based on biophysically realistic axon models [60]. The trained algorithm could then predict stimulation settings based on a new target volume of tissue that one wished to activate. This approach, however, required a large number of upfront simulations to train the classifier resulting in a significant computational time investment for each patient. Another study implemented a simpler approach by optimizing a less complex model of neural activation (without actually simulating multi-compartment neuron models). In that study, Xiao and colleagues showed that one could maximize the sum of the activating function [61] values within a region of interest using convex optimization to automate programming of DBS arrays [62]. In this dissertation, a novel optimization algorithm was developed and tested in computational models of ventral posteriolateral pars oralis (VPLo, equivalent to ventral intermediate nucleus, or Vim, in humans) for treating essential tremor, and in computational models of the GPe/GPi and STN for treating PD using subject-specific imaging data. Additionally, the efficacy of the algorithm was evaluated in the STN of a parkinsonian non-human primate.

1.5 Sensing with DBSA and Local Field Potentials

In additional to current steering, another advantage of segmented DBS leads is that they offer increased spatial resolution for recording (or sensing) electrophysiological signals within the brain. Electrophysiological signals arise in many spatiotemporal forms, can be sensed across a wide spectrum of frequency scales, and derive to a large extent from different neural processes depending on the spatial scale of the recording. With DBS

electrodes, which typically have an impedance of 10-100 kΩ (at 1000 Hz), the local field potential (LFP) signal is typically the most readily available signal to detect.

The exact neural correlates of LFP signals are not clear, but the current consensus is that LFPs reflect synaptic activity in a volume of tissue several hundred microns to 5+ mm surrounding the electrode [63,64]. LFPs are often supplementary to action potential information in that LFPs are thought to reflect synchronous neuronal firing [65–67]. Synchronous firing of neuronal processes arranged topographically and adjacent to the DBS lead are thought to result in increased spectral power in the recorded LFP signals due to field potential summation [68,69]. LFP signals are thus dependent on neural interface parameters such as volume conduction through inhomogeneous and anisotropic tissue [70] and DBS lead geometry [71]. LFP signals are considered to reflect the state of the local oscillatory networks surrounding the DBS lead. Thus, certain features of oscillations in the LFP signals are often used as biomarkers, and spectral content of the LFP signals could be helpful in aiding the DBS programming process including applications of closed-loop algorithms. LFPs also show relatively good spatial and temporal resolution compared to other oscillatory signals such as EEG; and it has much better signal reliability over time than spike recordings [72–74].

One of the hypotheses addressed in this dissertation is that the spatial resolution of unique LFP signals in the basal ganglia are at a spatial scale that is smaller than what is currently available from commercially-available DBS leads with cylindrical electrodes stacked along the lead body. In this dissertation, the DBS array allows for sensing in four radial directions in comparison to the omnidirectional sensing in the clinical Medtronic 3387 or 3389, whose cylindrical electrodes in theory summate oscillatory activities around the DBS lead. Modeling studies of DBS leads have confirmed that the geometry of the sensing electrode can have a significant effect on the LFP amplitude and spatial reach [71]. Furthermore, as the DBS targets such as GP and STN often contain multiple small subcircuits [28–31] and oscillatory networks [32–39] in spatial scales less than one millimeter, using a segmented lead such as the DBS array can ensure that the small dipoles in those local networks are not shorted simply because of the large geometry of the electrode contacts and the large spacing between electrodes.

1.6 Objectives and Research Goals

This dissertation addresses the programming challenges that arise with high density segmented DBS leads through development of a non-convex optimization algorithm that leverages subject-specific computational models, evaluation of the algorithm predictions in a parkinsonian non-human primate, and further exploring the use of higher-density LFP recordings for future use in closed-loop DBS systems.

Chapter 2 describes the development of a semi-automated optimization algorithm, called particle swarm optimization (PSO) that provides a computationally efficient way to program DBS systems using a swarm of individual particles representing electrode configurations and stimulation amplitudes. Using a finite element model of motor thalamic DBS, the PSO algorithm can efficiently optimize a multi-objective function that maximizes predictions of axonal activation in a region of interest (ROI, cerebellar-receiving area of motor thalamus), minimizes predictions of axonal activation in a region of avoidance (ROA, somatosensory thalamus), and minimizes power consumption.

Chapter 3 describes an updated version of the PSO that was developed to enable selections of multiple ROIs and ROAs. The updated PSO was then applied in the GPe/GPi and STN, traditional DBS targets for treating PD. In addition, the ability of the PSO to identify STN-DBS settings that would effectively reduce parkinsonian motor signs including rigidity, bradykinesia, akinesia, and gait dysfunction was tested *in vivo* in a non-human primate. The performance of the PSO settings was compared to both a randomized PSO setting and conventional monopolar stimulation settings using grouped electrode configurations. The results showed that the PSO selection was as good as or better than the monopolar stimulation settings and randomized PSO settings. This is notable as the selection of settings was purely based on subject-specific imaging and computational models without *a priori* knowledge of therapeutic configurations.

Chapter 4 describes the sensing ability of the DBS array, which in future studies could aid in the selection of PSO-based programming solutions as well as could facilitate

recording of electrophysiological biomarkers of DBS therapy and side effects for closed-loop control of the programming process. LFP signals were recorded from DBS arrays in the GPe/GPi and STN in both resting state and during a reach-and-retrieval task in two non-human primates in both naïve and parkinsonian conditions. The recorded LFPs and the spatial heterogeneity in the frequency domain were compared to virtual macroelectrodes -- a spatial summation of electrodes that were made to mimic those of cylindrical electrodes in conventional DBS leads for human use. The results showed that there is significant heterogeneity in spectral information of bipolar signals at a spatial resolution that is much smaller than what is used in human patients with conventional DBS leads.

Chapter 2
Particle Swarm Optimization for Programming Deep Brain Stimulation Arrays

2.1 Introduction

Deep brain stimulation (DBS) therapy has shown tremendous promise and growth over the past decades as an invasive neurosurgical technique for treating numerous brain disorders [75]. The clinical success of DBS relies on both accurate implantation of one or more leads of electrodes into deep brain target(s), and identification of stimulation parameters that alleviate symptoms without inducing adverse side effects. One recent advance in the field of DBS that can address both factors is the development of DBS leads with electrodes distributed both along and around the shank of the lead [76–80]. With this increase in number and distribution of electrode sites, these so-called DBS arrays (DBSAs) expand the programming options for steering, shifting, and sculpting volumes of neural activation [77,81]. Such functionality may be especially important when DBS leads are positioned in a brain region with a non-uniform target morphology [82], or when DBS leads are implanted in close proximity to nuclei or fiber pathways that, when stimulated, evoke adverse side effects [77,79,80].

However, increasing the number of independent electrodes creates the logistical challenge of identifying (or programming) the stimulation settings that optimize therapy for a patient. DBS leads with four cylindrical electrode contacts are known to require hours of meticulous and tedious trial-and-error programming in some cases [83], and the increase to eight [78] or thirty-two electrodes [76] is likely to create an intractable problem to optimize electrode configurations and stimulation parameters within a clinical setting. One

solution to decrease the high-dimensionality of this programming problem is to construct computational neuron models of DBS that are fit to patient imaging data [84–87] and then apply efficient algorithms to identify stimulation parameters on a subject-specific basis [58,88].

One previously developed algorithmic approach is based upon machine learning and training a classifier on thousands of computational neuron model simulations [88] that are based on biophysically realistic axon models [89]. These axon models are distributed across a range of orientations relative to a DBS lead, and finite element models are used to solve for the tissue voltage across a range of electrode configurations and stimulation settings [90,91]. Geometrical features that describe the resulting volume or tracts of tissue activated from these neuron model simulations are then used to train a machine learning algorithm. The trained algorithm can then predict stimulation settings based on a new target volume of tissue that one wishes to activate. While comprehensive in formulation, the machine learning approach requires a large number of upfront simulations to train the classifier.

A more computationally efficient approach for automating the DBS programming process is to optimize a less complex model of neural activation without actually simulating multi-compartment neuron models. In such models of electrical stimulation, one typically estimates the stimulus-induced currents applied to each neuronal membrane compartment through an activating function [92], driving function [52], or weighted driving function [93] that is calculated from extracellular voltages obtained from solving finite element models. For example, Xiao and colleagues showed that one can maximize the sum of the activating function values within a region of interest using convex optimization to automate programming of DBS arrays [58]. Similarly, genetic algorithms have been developed for programming stimulation settings through peripheral nerve cuff electrodes [94]. The challenge, however, with this overall approach is knowing how well the less complex model simulations actually compare with the more detailed multi-compartment neuron models that incorporate more biophysically realistic elements and parameters.

In this study, we formulate the problem of predicting neural activation within regions of interest and regions of avoidance as a non-convex, discrete-valued objective

function with local minima. To solve such a problem, we developed a particle swarm optimization (PSO) methodology, which works by iterative exploration of the electrode configuration and stimulation amplitude parameter space. The PSO approach has been successfully applied in a number of optimization problems [95], which range from permutations [96], inversion of ocean color observations [97], training multi-layer neural networks [98], predicting tremor onset [99], and tracking human motion without markers [100]. In addition to implementing the PSO approach to solve the non-convex, threshold-based problem we have formulated, we also extend the optimization problem to a multi-objective one that optimizes for three separate clinically relevant objectives: (1) maximize activation of the therapeutic target volume, (2) minimize activation of side effect volumes, and (3) minimize overall power consumption.

2.2 Methods

2.2.1 Finite Element Modeling (FEM)

A three-dimensional finite element model (COMSOL Multiphysics v5.2) was developed for a DBS array [101], which consisted of 32 elliptical electrodes (0.53 mm major axis, 0.3 mm curved minor axis, 0.1 mm thick) arranged in eight rows and four columns along the cylindrical lead (0.5 mm diameter). Conductance values for lead insulation ($\sigma = 1\times10^{-12}$ S/m) and electrodes ($\sigma = 1\times10^{6}$ S/m) were set according to a previous model from our group [58], approximating the conductance of silicon carbide and polyimide insulation and conductive platinum electrodes, respectively. Though more complex tissue conductance models of DBS have been developed [102–105], for the purposes of demonstrating the PSO algorithm, we assigned simple isotropic conductance values to the encapsulation layer (0.1 mm thick; $\sigma = 0.18$ S/m) [106] and to the bulk tissue (100 mm diameter; $\sigma = 0.3$ S/m) [107]. Quadratic tetrahedral mesh elements were generated by Delaunay triangulation with variable resolution mesh refinements set such that further refinement of the mesh yielded

less than 5% changes in the activating function measure. The resulting mesh consisted of 4,104,421 domain elements, 204,990 boundary elements, and 12,708 edge elements [58,108].

While there are myriad number of electrode configurations and stimulation amplitudes that could be modeled, we leveraged the principle of superposition and solved the Poisson equation in COMSOL to calculate the tissue voltage map individually for each of the 32 electrodes. In this case, for each simulation, a single electrode was set as the boundary current source with a cathodic current of 1 mA (current density 8.63×10^3 A/m^2) and the outer surface of the bulk tissue was set to ground. These single boundary current source simulations resulted in tissue voltage maps, which were then scaled and superimposed to generate finite element modeling solutions for more complex electrode configurations with independent current sources.

2.2.2 Predictions of Thalamocortical Axon Model Activation

2.2.2.1 Motor and Somatosensory Thalamus Reconstructions

For this study, we modeled stimulation targeting the rhesus macaque cerebellar-receiving area of motor thalamus (VPLo: ventral posterolateral pars oralis) [58], which is equivalent to the ventral intermediate nucleus (Vim) in humans and primary DBS target for treating essential tremor. Of note, clinical DBS implants targeting this nucleus can be difficult to program because of low-threshold side effects such as paresthesia, which are thought to result from the spread of stimulation into the somatosensory thalamus (VPLc: ventral posterolateral pars caudalis) [80,109]. Surface reconstructions of the region of interest (ROI; in this case, VPLo thalamus) and the region of avoidance (ROA; VPLc thalamus) were generated from the rhesus macaque brain [58,110]. A DBSA was placed within the VPLo volume at 77° above the horizontal plane and at 10° from the sagittal plane in an anterior to posterior trajectory **(Fig. 2.1A**). VPLo and VPLc volumes were populated with 4,549 and 5,937 thalamocortical axon models (0.2 mm internodal spacing, with each axon

arranged in a grid 0.72 mm away from adjacent neighbors) with simplified linear trajectories running from ventromedial to dorsolateral at 45° from the axial intercommissural plane (**Fig. 2.1B**). The linear trajectory and 45° angle were approximated from a previous investigation of efferent thalamic fibers in non-human primates [111]. Axon models that overlapped the DBSA were removed from subsequent analysis.

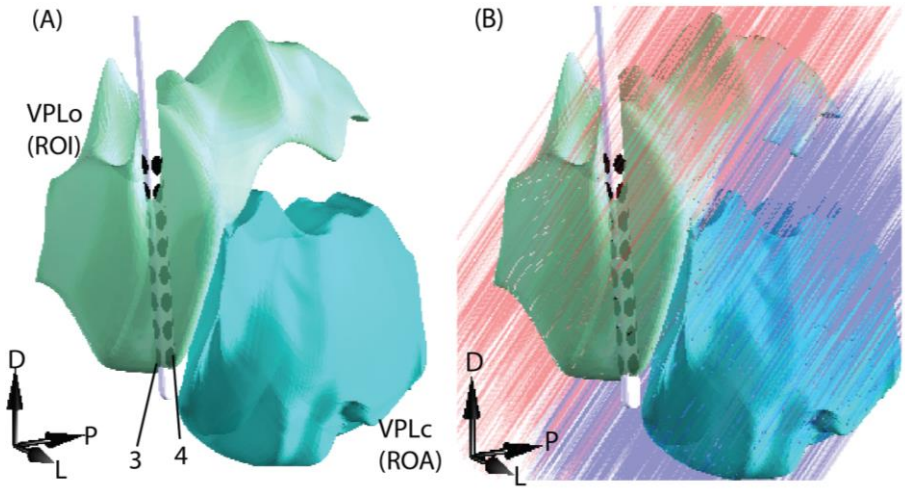

Figure 2.1: *Models of thalamic DBSA stimulation. (A) Reconstructions of the cerebellar-receiving area of motor thalamus (VPLo, green) and somatosensory thalamus (VPLc, blue) from the rhesus macaque, showing DBSA placed 77° above the horizontal plane and at 10° from the sagittal plane in an anterior to posterior trajectory* [58]. *(B) Trajectories of thalamocortical axons (VPLo axons: red, VPLc axons: blue) extending from both thalamic nuclei.*

2.2.2.2 Modeling Myelinated Axon Activation

One way to estimate axonal activation resulting from extracellular stimulation is to solve the inhomogeneous cable model equation of a myelinated axon [112–114]:

$$\lambda^2 \frac{\partial^2 V_m}{\partial x^2} - \tau_m \frac{\partial V_m}{\partial t} - V_m = -\lambda^2 \frac{\partial^2 V_e}{\partial x^2} \quad (1)$$

where λ is the axon space constant that is dependent on the axon dimensions and geometry, V_m is the membrane voltage, τ is the time constant of the axonal membrane, and V_e is the interpolated extracellular potential calculated from the finite element model solution. For simplicity, the source term can be approximated with the difference approximation:

$$\frac{\partial^2 V_e}{\partial x^2} \approx \frac{V_{e,n-1} - 2V_{e,n} + V_{e,n+1}}{\Delta x^2} \tag{2}$$

where $V_{e,n}$ corresponds to the extracellular voltage at node n, and Δx is the distance between adjacent nodes of Ranvier. This source term or "activating function" has been shown to provide a reasonable approximation of the non-faradaic transmembrane currents that result from the initial onset of an extracellular stimulation pulse [92,112].

Here, we use a modified activating function (MAF) to predict axonal activation. We compute the second spatial difference using extracellular potentials from non-adjacent nodes of Ranvier:

$$MAF = V_{e,n-2} - 2V_{e,n} + V_{e,n+2} \tag{3}$$

Notably, this approach is fundamentally the same as the activating function, except that it yields a smoother version of the activating function. Because this modified spatial difference is a linear function of the extracellular potentials, the superposition principle can be used to efficiently predict MAF values for an arbitrary electrode configuration [58]. For each axon, we constructed an N-by-32 matrix (denoted as the "C matrix") containing the MAF value for all N nodes of Ranvier when stimulating through each electrode individually. This enabled computing the MAF value at every node for arbitrary electrode configurations by multiplying the C matrix with the 32-by-1 vector of currents going through each electrode of the DBSA.

2.2.2.3 Defining MAF Thresholds for Axonal Activation

An axon was considered activated if, for a given electrode configuration, the MAF value exceeded a predefined threshold (MAFT) at one or more of its nodes. Because the choice of MAFT is dependent on the specific axonal geometry, we tuned our MAFT empirically to maximize its predictive accuracy for our thalamic fiber geometry. We simulated the axonal fiber geometries as multi-compartment myelinated axon models in NEURON (v7.4). Axon models consisted of 2 µm diameter fibers with compartments representing nodes of Ranvier, myelin attachment segments, paranode main segments, and internode segments connected through an axial resistance [89]. Axonal membrane compartments were each driven using the extracellular mechanism in NEURON (e_extracellular) [80,82,115]. We applied a waveform with a 90 µs cathode-leading phase, 400 µs interphase delay, 3 ms charge-balanced anodic phase, and 135 Hz pulse rate [116]. The specific extracellular potential localized to each axonal node from current-controlled DBS inputs (0 to -1 mA per electrode) was estimated with the FEM and superposition. After running 30 primer simulations with a range of electrode configurations, we computed a best fitting MAFT value by minimizing the mean squared error between MAFT predictions and the 30 primer NEURON simulations. The obtained MAFT value (0.0023) was used for all subsequent PSO runs.

2.2.2.4 Estimating Axonal Activation

The MAFT value was then used to construct functions that predicted the number of axons activated in ROI, *R(x)*, and the number of axons activated in ROA, *S(x)*. These threshold-based functions were described as follows:

$$R(\vec{\boldsymbol{x}}) = \sum_{i=1}^{U} H(\max(C_{ROI,i}\vec{\boldsymbol{x}}) - \alpha) \quad (4)$$

$$S(\vec{\boldsymbol{x}}) = \sum_{j=1}^{V} H(\max(C_{ROA,j}\vec{\boldsymbol{x}}) - \alpha) \quad (5)$$

where x is a vector of size 32 corresponding to the current through each electrode; $C_{ROI,i}$ and $C_{ROA,j}$ are the C matrices for ROI axon i and ROA axon j, respectively; $H(\bullet)$ is the Heaviside function; and α is the MAFT value. Using a MAFT value of 0.0023 (obtained as described in Section 2.2.2.3), the discrepancy between MAFT-based predictions and NEURON model predictions was less than 1% of the total axons in either ROI or ROA (**Fig. 2.2**). Given this low discrepancy, the MAFT value and the functions $R(x)$ and $S(x)$ were used in all subsequent PSO simulations.

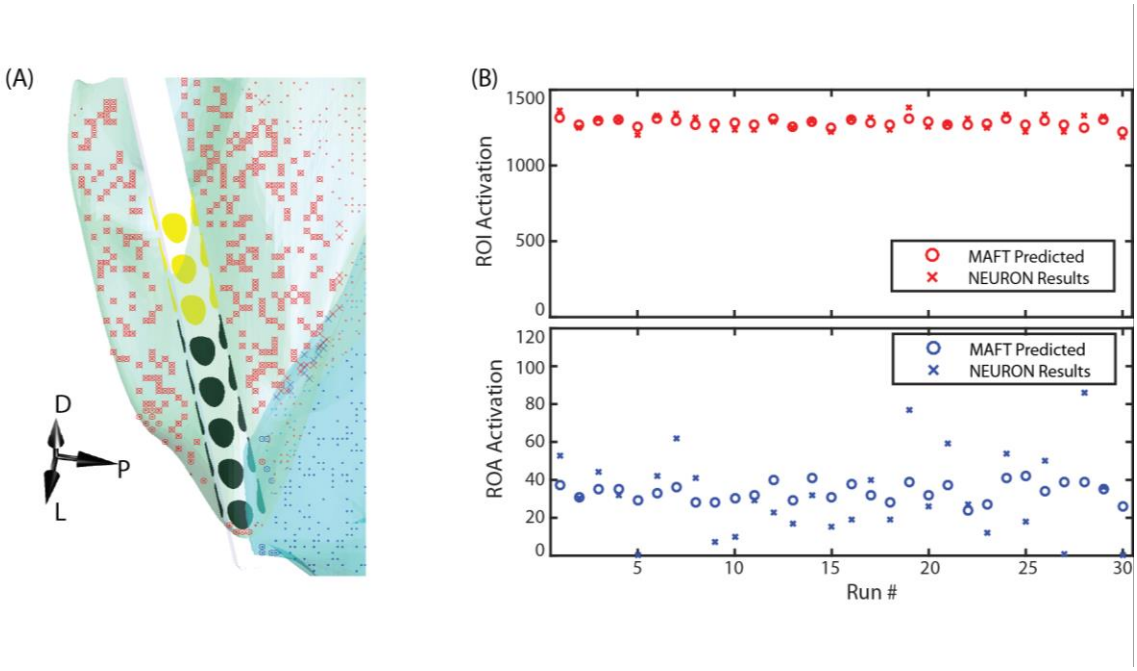

Figure 2.2: *Comparison of MAFT predictions and NEURON model predictions in the ROI and ROA. (A) Spatial cross sectional view of a subset of axons illustrated overall agreement between the MAFT (o) and NEURON predictions (x). (B) Comparison of MAFT and NEURON predictions in terms of number of axons activated. Results indicated a discrepancy of -1.3 ± 38 axons (slight MAFT underestimate) for ROI, and 1.6 ± 20 axons (slight MAFT overprediction) for ROA. This constituted a discrepancy of less than 1% of all axons.*

2.2.3 Optimization Problem

For the simplified thalamocortical axon geometry modeled, the optimization algorithm's objectives were to (1) maximize the number of activated axons in the ROI, (2) minimize the number of activated axons in the ROA, and (3) minimize the power dissipated by the stimulator. These three distinct objectives reflect the desired clinical outcome, in which robust therapy is delivered with little to no side effects and with low power consumption. Additionally, we constrained the stimulus waveform through each electrode contact to have a cathode-leading phase (between 0 to -0.5 mA), which was within the current density safety limits based on the electrode size. Conceptually, this optimization problem can be denoted as follows:

$$\text{maximize} \quad R(\vec{x}) \tag{6}$$

$$\text{minimize} \quad S(\vec{x}) \tag{7}$$

$$\text{minimize} \quad P(\vec{x}) = \sum_{k=1}^{32}({x_k}^2) \tag{8}$$

$$\text{subject to} \quad -0.5 \leq x_k \leq 0,\ k = 1, \dots, 32 \tag{9}$$

where *P(x)* is the power in mA^2 (not scaled by impedance).

To solve this multi-objective optimization problem, we employed a standard approach known as linear aggregation, which involves creating a single scalar objective function from the weighted sum of the three distinct objectives. We chose a weighting based on our ranking of importance of the objectives:

$$\text{minimize} \quad -R(\vec{x}) + (2)S(\vec{x}) + (0.5)P(\vec{x}) \tag{10}$$

$$\text{subject to} \quad -0.5 \leq x_k \leq 0,\ k = 1, \dots, 32 \tag{11}$$

However, one limitation of the linear aggregation approach, from the clinical perspective, is that it assumes that there is one correct prioritization between the three objectives. This limits the user who seeks to prioritize outcomes in a different, subject-specific manner. Ideally, we would be able to solve the optimization problem for every possible combination of weightings. To efficiently obtain solutions for a range of weighting combinations, we mixed the aggregation-based method with elements of a Pareto dominance-based method. Specifically, we leveraged the fact that exploratory optimization algorithms like particle swarm optimization evaluate many intermediate solutions in search of the "best" solution. We collected these intermediate solutions, and labeled as 'Pareto dominated' any candidate solution for which there was at least one 'better' solution (i.e. better in all three objectives). By collecting these intermediate solutions and getting rid of solutions that were Pareto dominated, we were able to construct a set of solutions known as the *Pareto front* (**Fig. 2.3**). Solutions on that Pareto front are considered *Pareto optimal* because they were not Pareto dominated by any other solution. As such, each solution on the resulting Pareto front represents the best electrode configuration possible given the specified tradeoffs. The Pareto front obtained from such a mixed approach enables the user to readily select among multiple Pareto-optimal electrode configurations without having to directly solve the problem for different weighting combinations. A schematic flow of this approach is illustrated in **Figure 2.4**.

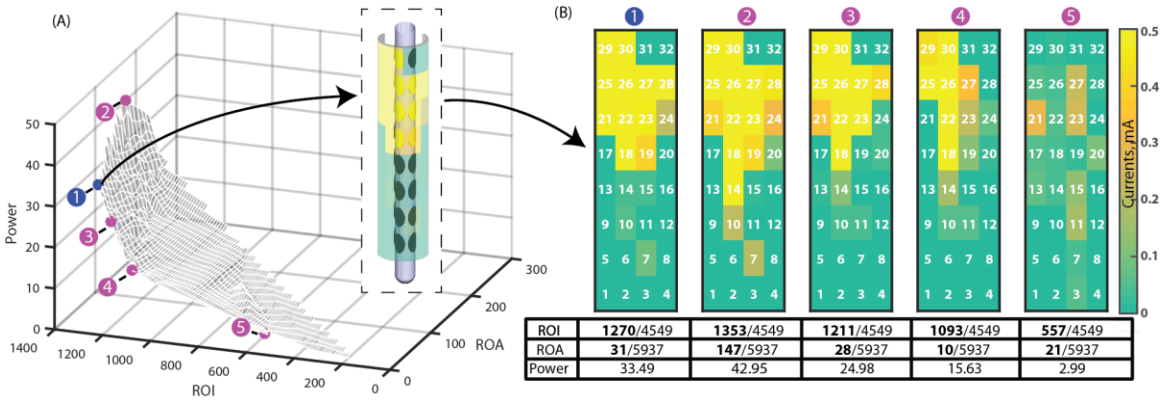

Figure 2.3: *Typical output from a PSO run. (A) A three-dimensional Pareto front showing five unique points on the Pareto front, where each point corresponds to a different predicted ROI and ROA activation (i.e. number of axons activated) and power consumption (in mA^2 without the impedance). Among them, point number 1 achieved the lowest objective function value (Equation 10). (B) Electrode configurations for each of the five highlighted points. Depending on a user's desired prioritization between ROI, ROA, and Power, a different point along the Pareto front can be selected for stimulation. The table shows the PSO-predicted axonal activation (bold, in number of axons) in relation to the total number of axons in ROI and ROA, as well as the PSO-predicted power consumption (in mA^2 without the impedance) for each electrode configuration.*

2.2.4 Particle Swarm Optimization

In this study, axons were considered activated when MAF exceeded a certain threshold (MAFT) at any point along the axon. Mathematically, this type of discrete function does not meet the criteria for convex optimization techniques. Therefore, to solve this problem without relaxing the parameters of the problem, we implemented a particle swarm optimization (PSO) approach in MATLAB (v2014b).

2.2.4.1 PSO Behavior

PSO solves optimization problems through a series of searches performed by a collection of interacting individuals [117]. Each individual (particle) exhibits three simple behaviors that enable it to search through the solution space, and to communicate its findings to neighboring individuals (swarm). The most fundamental of these behaviors is the particle's persistent and somewhat random movement through solution space, which enables it to explore different potential solutions over time (i.e. inertia). The second behavior is the particle's tendency to move toward a point that the swarm considers to be the best so far

(i.e. the "social" or "global" best). The third behavior is the particle's tendency to move towards the best point the particle itself has found (i.e. the "cognitive" best).

Mathematically, a particle's position in the solution space at a given time can be described as follows:

$$x_i(t+1) = x_i(t) + v_i(t+1) \tag{11}$$

$$\text{where } x_i(0) \sim U(X_{min}, X_{max}) \tag{12}$$

where x is the position (i.e. electrode current) bounded between X_{min} and X_{max}, i is the particle number, t is iteration, and v is the "velocity" term (i.e. change in current). The three simple behaviors of the particle are included in this velocity term by three components: inertial, social, and cognitive [118]. Hence, velocity is defined as:

$$v_{ij}(t+1) = w \cdot v_{ij}(t) + c_1 \cdot r_{1ij}(t) \cdot [y_{ij}(t) - x_{ij}(t)] + c_2 \cdot r_{2ij}(t) \cdot [\hat{y}_j(t) - x_{ij}(t)] \tag{13}$$

where j is the electrode number, w is the inertial component, c_1 is the cognitive component, c_2 is the social component, y is the particle-specific best as of iteration t, and $\hat{y}$ is the global best as of iteration t. Meanwhile, r_{1ij} and r_{2ij} are additional weighting factors that allow for randomness, which promotes exploration. In our implementation, we set r_{1ij} to be randomly distributed between 0 and 1 (inclusive), while r_{2ij} was set to 1 for all i and j. As such, the random component of motion was solely due to the cognitive component. Finally, we defined w as follows:

$$w(t) = -\frac{w(0) - w(n)}{n} t + w(0) \tag{14}$$

where n is the maximum number of generations. We set w such that it decreased linearly from 0.9 to 0.4 in order to promote initial exploration followed by a tendency to converge toward the end [118] (**Table 2.1**).

2.2.4.2 Cognitive vs. Social Velocity Components

PSO exploration is driven by social and cognitive components, such that the choice of c_1 (cognitive) and c_2 (social) significantly influences the effectiveness of exploration in a problem-specific way. To determine appropriate c_1 and c_2 values for our thalamic geometry, we performed a parameter sweep by running the PSO algorithm five times for every possible combination of c_1 and c_2 across a range of values (0.025, 0.05, 0.1, 0.2, 0.4, 0.9, 1.8, 2.7, 3.6, 4.5, 5.4, and 6.3). We then assessed each combination based on (1) the optimality and consistency of its objective function value (i.e. mean and standard deviation of objective function value), and (2) its termination status (i.e. convergence vs. stalling vs. generation limit reached).

2.2.4.3 Number of Particles

The number of particles affects how effectively and efficiently the swarm can explore the search space. More particles increase the extent of exploration, but also increase computational demand. To select an appropriate number of particles for the modeled thalamic geometry, we assessed the performance of PSO with respect to 50, 100, 200, and 400 particles. Accuracy was measured using the minimum objective function value achieved, while computational demand was measured by the number of objective function calls by the program.

2.2.4.4 Stimulation Current Constraints

In our implementation of PSO for DBSA programming, each electrode configuration was represented as a particle in 32-dimensional space (corresponding to the 32 electrodes). Each dimension was bounded between 0 mA to -0.5 mA, corresponding to current constraints below typical current density limits (**Table 2.1**). We generated 100 particles, 68 of which were initialized to have random current through each electrode (within 0 to -

0.25 mA). The remaining particles were initialized to have exactly -0.25 mA going through only a single electrode. This so-called "multi-start initialization" approach promoted exploration of the search space [117]. Constraints were enforced by checking for any out-of-bounds particles at each iteration. Particles that exceeded the current constraints at any given electrode were stripped of their velocity (i.e. v=0) in that electrode's dimension, and that electrode's max stimulus waveform current was set to either 0 mA or -0.5 mA, depending on which bound was exceeded. Notably, these current bounds were the only constraints applied to the particles.

2.2.4.5 Generations and Termination Criteria

Similar to genetic algorithm approaches, the PSO algorithm involves the exploration of a state space over the course of multiple "generations" in order to find optimal solutions. We established three termination criteria: (1) convergence, (2) stalling, and (3) reaching the generation limit. The criteria for convergence, stalling, and generation limits were tuned by trial and error. Specifically, we considered particles to be converged if the particles' currents were close to each other in at least 30 out of 32 electrodes, as measured by a given electrode having a the standard deviation less than 0.004 mA across all particles. In addition, we considered particles to be stalled if the objective function score did not improve for 100 consecutive generations (**Table 2.1**). Meanwhile, we set the generation limit to be 200 generations (**Table 2.1**) since we found this enabled enough iterations for convergent runs to terminate while also enabling non-convergent runs to explore the space and improve Pareto front estimates. If any of the termination criteria were met, the PSO algorithm terminated and returned the estimated Pareto front (**Fig. 2.4**).

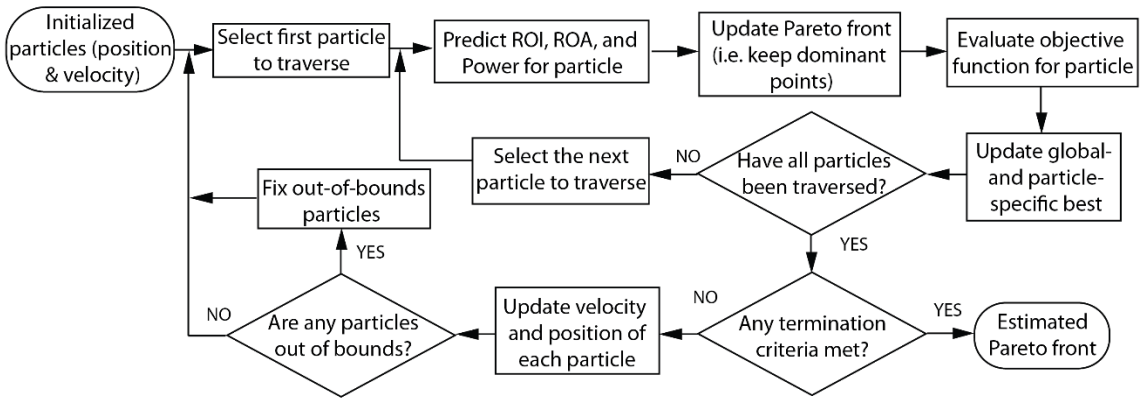

Figure 2.4: *Flowchart for the aggregated-based PSO algorithm*

2.3 Results

2.3.1 PSO Variable Parameter Sweeps

Consistently low objective function values were obtained when c_1 was 3.6, 4.5, or 5.4 and when c_2 was 0.1, 0.2, or 0.4 (white outlined boxes in **Fig. 2.5A-B** and black outlined box in **Fig. 2.5C**). We used low objective function values as a measure of accuracy because such values were obtained by having either (1) increased ROI activation, (2) decreased ROA activation, or (3) decreased power. As such, the lowest objective function value also corresponded to the most favorable electrode configuration possible. While the stochastic nature of our algorithm did not guarantee that it would find the lowest possible objective function value on any given run, we took a lower objective function value to mean that the algorithm had more closely approached this "true" best. Thus, from the set of c_1 and c_2 combinations that had low objective function values, we selected center values for c_1 as 4.5 and c_2 as 0.2 for all subsequent PSO runs (**Table 1**). With respect to number of particles, an increase from 50 to 400 caused computational demand to increase linearly, while generating only a small improvement in accuracy (**Fig. 2.5D**). We chose a balanced tradeoff by selecting 100 particles for the remaining simulations (**Table 2.1**).

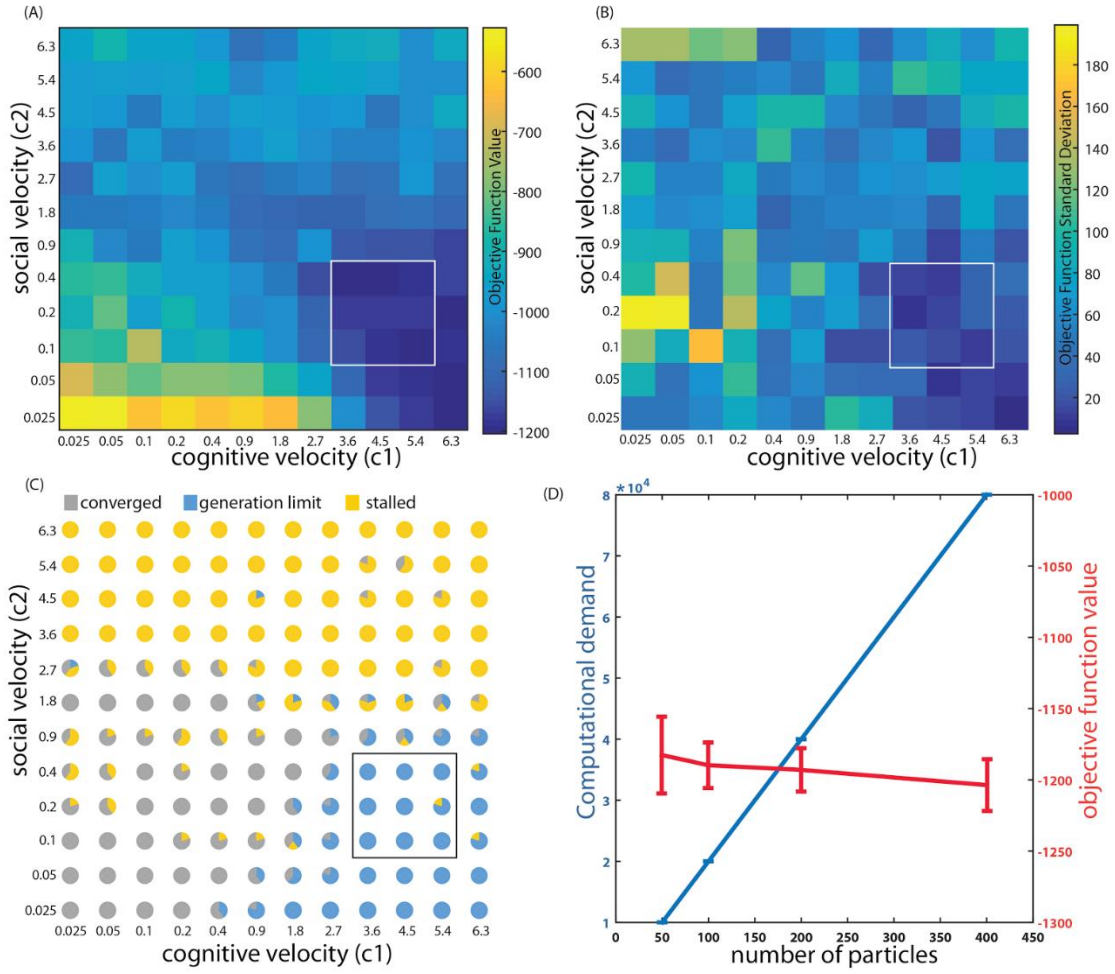

Figure 2.5: *PSO algorithm parameter sweeps across cognitive and social velocities. Plots show (A) mean objective function values across 5 runs, (B) standard deviation of objective function values across 5 runs, and (C) termination behavior. The boxes highlight a range of c_1 and c_2 values that consistently yielded low objective function values with little stalling. (D) Effects of number of particles on objective function value and computational demand.*

Table 2.1: *PSO Algorithm Parameter Values*

Parameter	Value
Number of Particles	100
Generation Limit	200
Stalling Generation Constant	100
Cognitive Attraction Weight, c_1	4.5
Social Attraction Weight, c_2	0.2
Upper Inertia	0.9
Lower Inertia	0.4
Velocity Limit	Infinite
Additional Cognitive Weighting, r_{1ij}	[0,1] (random)
Additional Social Weighting, r_{2ij}	1
Lower Bound Current per Contact	-0.5 mA
Upper Bound Current per Contact	0 mA
Total Bounded Current	none

2.3.2 Consistency of PSO Solutions

We measured the PSO algorithm's consistency by quantifying the variation in Pareto fronts across 30 independent runs (**Fig. 2.6**). In addition, we compared each estimate to a "combined" Pareto front that was constructed from all 30 Pareto front estimates. For each point *Y* on each of the 30 Pareto fronts, we computed the discrepancy between *Y* and the closest "combined" Pareto front point. As shown in **Figure 2.6A** for five sample Pareto fronts, the fronts exhibited considerable overlap, and their respective "best" electrode configurations had in common 8 out of 11-13 active electrodes (**Fig. 2.6B**). Furthermore, predicted ROI activation variation was within 2.0% across all 30 runs. Constructing a "combined" Pareto front (**Fig. 2.6C**) and comparing its distribution of values to the all 30 runs (uncombined), we observed a relatively small difference in median ROI activation (19 axons), median ROA activation (-20 axons), and median power (-4.11 mA^2) (**Fig. 2.6D**).

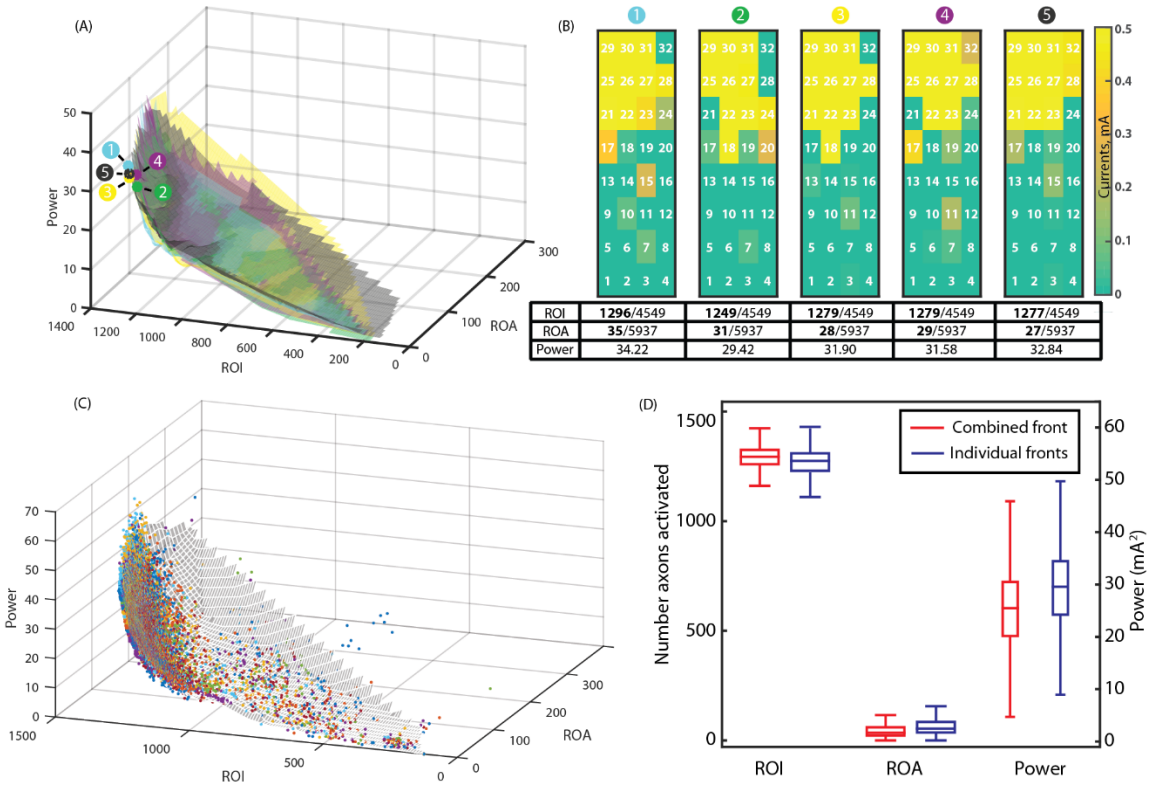

Figure 2.6: *Pareto fronts from multiple PSO algorithm runs. The point that minimized the objective function is highlighted on each of the five independent Pareto front (A) and the corresponding electrode configurations are provided (B). The table shows the PSO-predicted number of axons activated in relation to the total number of axons in ROI and ROA, as well as the PSO-predicted power consumption for each electrode configuration. Pareto fronts and electrode configurations exhibited consistent topographies across runs. The "combined" Pareto front (C) was obtained from all points from 30 independent Pareto fronts. (D) Comparing the distribution of ROI, ROA, and Power across all runs to the distribution across the combined Pareto front in (C), there was a relatively small difference in axons activated and power. ROI and ROA are in units of "number of axons" and power is in unit of "mA^2" without the impedance.*

2.3.3 Robustness

We evaluated robustness by measuring ROI, ROA, and Power under three conditions: (1) the existence of open electrode sites (i.e. those unusable because of very high impedances); (2) low per electrode current limit (e.g. low battery); and (3) lead shifts by 1 mm anterior, posterior, medial, and lateral relative to the DBSA trajectory. The PSO was able to accommodate for disabling 3 or 12 active electrodes, with ROI activation reduced by only 1.8% and 14%, respectively (**Fig. 2.7A**). Reducing the maximum per-electrode current by 50% and 80% reduced ROI activation by 5.6% and 16%, respectively (**Fig. 2.7B**). Lead displacement by 1 mm in the anterior, posterior, medial and lateral directions relative to the center location resulted in relatively small changes in ROI activation (-7.5%, -3.6%, -6.9%, +9.2%) without significantly changing ROA activation (<1% change in any direction) (**Fig. 2.7C-D**).

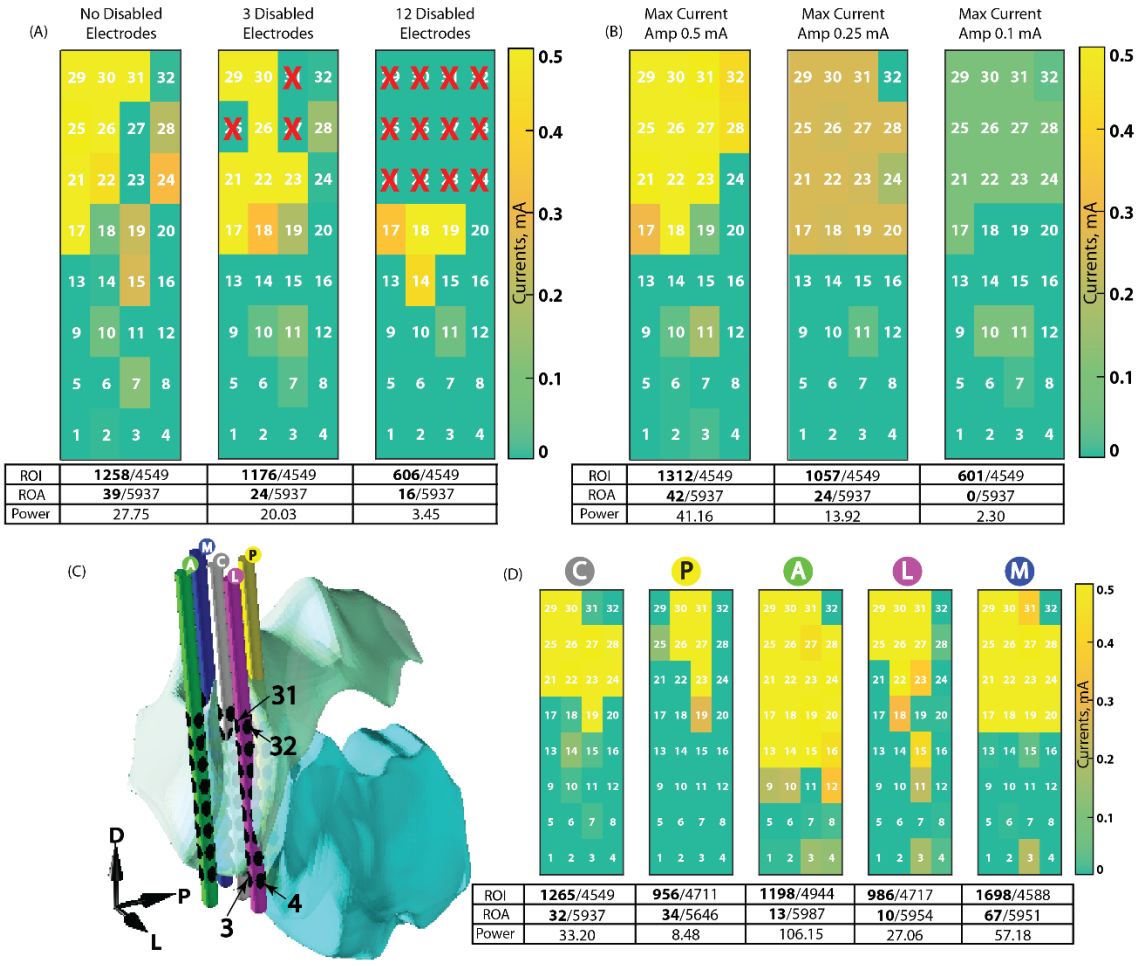

Figure 2.7: *Three tests for PSO algorithm robustness. (A) When three select electrodes near the ROI were disabled, the algorithm maintained relatively stable activation of ROI. Disabling additional electrodes resulted in ineffective targeting. (B) The algorithm exhibited similar robustness when reducing the upper bound current. (C-D) When shifting the DBSA lead from original center position "C" to 1 mm posterior "P", anterior "A", lateral "L", and medial "M" relative to the DBSA trajectory, the algorithm adjusted stimulation to reflect the new location of the spatial target. The tables show the PSO-predicted number of axons activated in relation to the total number of axons in ROI and ROA, as well as the PSO-predicted power consumption for each electrode configuration. ROI and ROA are in units of "number of axons" and power is in unit of "mA^2" without the impedance.*

2.3.4 Efficiency

Efficiency was measured as the average runtime for constructing a Pareto front and obtaining a best electrode configuration. We assessed this by running the PSO algorithm five times on a PC with eight cores, 64-bit operating system, 24.0 GB RAM, and an Intel Core i7 processor at 3.40 GHz. The algorithm took 3.19 seconds per generation, resulting in an average of 10.6 minutes per run. These times reflected the duration for obtaining a solution after segmentation of the brain volume, positioning of the DBSA within the volume, incorporation of axonal tract morphologies, and identification of the MAFT for the ROI and ROA.

2.4 Discussion

In this study, we developed a particle swarm optimization approach to identify DBS electrode configurations and stimulation amplitudes that generate the most selective and efficient activation of a region of interest around a DBS array. This multi-objective problem incorporated a Pareto front, which offers a range of optimal electrode configurations from which a user can choose based on patient-specific programming goals. For example, a programmer may decide that activation within an ROA above 10% is undesirable for a given patient, whereas in another case, this value can be higher or lower. Thus, while the PSO is an automated algorithm, the user can select and test a set of optimized solutions along the Pareto front as needed, making the overall programming process more intuitive despite the complex geometries and nontrivial electrode configurations involved.

2.4.1 Particle Swarm Optimization

Particle swarm optimization algorithms employ cognitive and social components that adapt across multiple iterations, much like genetic algorithms and other evolutionary algorithms [94,119]. In the case of the PSO algorithms, the individuals (or particles) survive throughout all iterations and continue to refine the solution to the overall problem [117]. This iterative refining process enables PSO to efficiently and effectively search the solution space. For multi-objective PSO, there are a number of approaches for selecting best solutions and subsequently updating particle positions. We used a mix between the linear aggregation-based approach and a Pareto dominance-based approach. Specifically, we used a linear aggregation objective function to guide exploration of the particles, and we used Pareto dominance criteria to construct an archive of Pareto-optimal points from all explored candidate solutions.

The linear aggregation-based approach combines all the objectives of a multi-objective problem into a single objective function with fixed weights. This is the simplest approach to multi-objective PSO [95]. However, this approach gives only one solution, and does not consider the range of the solutions that could be obtained by altering the weighting of the objectives. To address this, we coupled a Pareto dominance-based method to keep track of all the Pareto-optimal points at every intermediate iteration [120]. Notably, the Pareto front estimate was fundamentally independent of the final solution obtained from the aggregate-based approach, which yielded Pareto front estimates that were robust to choice of weighting for ROI, ROA, and power consumption. In other words, assigning a different weighting to each of the objectives (ROI, ROA, power) would yield a comparable Pareto front estimate in spite of the algorithm evolving differently across iterations.

In addition to linear aggregation-based approaches, there are also a number of more complex Pareto dominance-based methods [121] that may yield more efficient Pareto front estimates (e.g. in fewer generations or with fewer particles). These Pareto dominance-based approaches rely on selecting non-dominated “leader” solutions to guide the algorithm. Employing such methods for DBSA programming would require testing and tuning several different parameters, such as leader selection schemes, swarm diversity, particle front spread, and archive maintenance [95].

Also important to PSO algorithms in general is the topological network of connections amongst particles and neighborhoods, which govern the convergence behavior of the algorithm. Here, we fully connected all particles to one another such that all particles in the swarm were directly informed of the global best solution at each iteration. Using such a global network enables the swarm to converge more rapidly than using a local network (e.g. ring, tree, wheel, von Neumann networks), since a locally connected network is slower to propagate the information of the global best solution. The global network's faster convergence, however, may be undesirable if it leads to premature convergence on local optima [120]. As a result, using a local neighborhood approach may improve the diversity of exploration and consistency of the Pareto front estimates [122,123].

To avoid premature convergence and facilitate exploration, we employed three strategies: (1) we implemented a multi-start initialization approach (see Section 2.2.4.4); (2) we chose low social velocity relative to cognitive velocity, which promotes exploration [120]; and (3) we set the convergence criteria to be very strict, as the particles are considered converged only when the standard deviation of current was less than 0.004 mA (<1% of max current) in at least 30 electrodes.

Notably, while exploration is essential to obtaining consistent Pareto front estimates, convergence is not necessary. We found that similar and comparable results were obtained from non-converging runs that reached the generation limit. This finding enabled us to specify a generation limit (see 2.4.5) such that non-converging runs continued to make small improvements before terminating. Such a strategy produced more exploration at the cost of additional generations of the PSO. Future studies may wish to try different topological network organizations to aid the PSO algorithm in optimizing its parameter space exploration and convergence.

2.4.2 PSO Performance

2.4.2.1 Consistency

Across 30 independent runs, the means and standard deviations of the best points on the Pareto fronts were 1281 ± 22 (1.7%) for ROI activation, 34 ± 5 (14.7%) for ROA activation, and 34.0 ± 4.6 mA^2 (13.5%) for Power. Furthermore, visual inspection of five sample Pareto fronts indicated a significant overlap between the fronts. This level of consistency meant that one could expect the PSO algorithm to provide fairly similar outputs across runs (particularly for ROI activation) in spite of varying initial conditions.

The discrepancies between the "combined" Pareto front and the 30 individual fronts were 19 axons for median ROI activation, -20 axons for median ROA activation, and -4.11 mA^2 for median power. The signs reflect the fact that the "combined" Pareto front had higher ROI activation, lower ROA activation, and lower power, which was consistent with expectations. Considering these discrepancies in terms of the total number of axons for each region (4,549 for ROI and 5,937 for ROA) and the maximum power attained (60.04 mA^2), these discrepancies corresponded to <1% for ROI and ROA axons, and 6.8% for power. The overall small discrepancies further suggested that the PSO algorithm could come up with similar estimates of the Pareto front across runs. However, despite this overall low discrepancy, there were still points on the individual Pareto fronts that reached high discrepancies (e.g. up to ~300 axons, or ~7% of maximum ROI activated). Future implementations involving purely dominance-based Pareto front estimation (section 2.4.1) may help reduce the incidence of such deviations.

2.4.2.2 Robustness

The PSO was also robust to translation of the lead trajectory in relation to the ROA, which was located posterior, lateral, and slightly ventral to the ROI. As a result, shifting the lead 1 mm in the posterior direction positioned the lateral and posterior portions of the lead closer to the ROA. This caused a reduction in stimulation through the posterior electrodes (21, 25, 29) and the lateral electrodes (24, 28). The ventral electrodes (21, 22, 24) also had less current because the shape of the ROA at the new lead location had a greater ventral

extent. The consequence of fewer electrodes being active and the lead being closer to the ROA was lower Power consumption, lower ROI activation, and relatively unchanged ROA activation. This result aligned with our objective function weightings in which low ROA activation was more highly prioritized (Equation 10). Shifting the lead 1 mm in the lateral direction had a similar impact as the posterior shift, since it positioned the lead closer to the ROA. As a result, the posterior electrodes (site 21) and lateral electrodes (sites 24, 28) experienced a reduced current. In contrast to the posterior shift, however, the ventral electrodes were still active since the ventral end of the lead in the lateral shift still remained surrounded by ROI axons. The resulting solution had lower ROI activation, lower ROA activation, and lower Power (though Power was not as low as in the posterior shift). Shifting the lead 1 mm in the anterior direction had the opposite effect of the posterior shift. Since the lead at that location was further away from the ROA, there was less ROA activation. In addition, virtually every electrode in the ROI was sourcing current, resulting in an overall larger Power consumption. However, since this shift also caused the lead to have fewer surrounding ROI fibers, there was a reduction in ROI activation relative to the original location. Shifting the lead 1 mm in the medial direction positioned the lead farther away from the ROA in all directions, as well as positioning it deeper in the ROI. This resulted in more active ventral electrodes (sites 17-20), which increased Power (though not as much as in the anterior shift) and increased ROI activation. Notably, ROA activation was also increased, reflecting a tradeoff between the large increase in ROI activation and the relatively smaller increase in ROA activation (Equation 10).

Additionally, the PSO showed robustness to disabling ‘bad’ electrodes on the lead as well as modifying maximum current amplitudes resulting from a low battery, for instance. In the PSO runs, disabling posterior electrode 25 and anterior electrodes 27 and 31 led to an increase in current through the neighboring anterior electrode 23. Disabling the three most dorsal rows of electrodes (21-32) resulted in relatively higher current through the ventral electrodes 14, 17, 18, and 19. Overall, we observed the expected trend of reduced ROI, ROA, and Power as more electrodes were disabled. When employing more stringent current constraints, we also observed that the electrode configurations did not appreciably change in topology as current limits were reduced. As expected, lower current

limits were associated with lower activation of ROI and ROA, as well as lower Power consumption. This was consistent with the idea that a higher power consumption would allow for more activation, all else being equal. Notably, if we had instead set constraints that force the algorithm to budget a total amount (e.g. sum) of current across all electrodes, the reduced current limits may have evoked more complex changes in electrode configuration patterns.

2.4.3 Models for Predicting Axonal Activation

The PSO approach relies on accurate prediction of neural modulation from electrical stimulation. We used a modified version of the activating function (MAFT-predicted activation) to demonstrate the PSO approach. This MAFT-predicted activation tracked the multi-compartment NEURON models well (**Fig. 2.2**). While one could solve the nonlinear differential equations governing a multi-compartment neuron model as performed in NEURON and as we have shown here for a thalamocortical axon model, the computational time required for these calculations is high. This limitation led several groups to develop other simplified and more computationally efficient axonal excitability prediction models. These models have ranged from a discrete difference approximation of transmembrane current induced by extracellular stimulation (i.e. the so-called 'activating function') [92,112], to variations in the activating function that account for redistribution of current via space constants [124], to inclusion of additional source terms at other points along an axon that can affect a given node through intracellular ohmic conductance [52], to a weighted distribution of source terms [93]. It is important to note that the PSO algorithm as described here can utilize other computational approaches for modeling axonal excitability resulting from DBS, as long as the predictive functions are specified (Equations 4 and 5).

It is also important to acknowledge that predicting axonal activation depends on a variety of factors including axon diameter, distance between nodes of Ranvier, ion channel density at the nodes and surrounding compartments, current waveforms, and geometry of the axons relative to the induced electric field [89]. In terms of the latter, the MAFT value

was found to vary slightly amongst axonal orientations, which means that one would need to identify an activating function threshold *a priori* and for each axonal pathway that one wishes to evaluate with the PSO. Along these lines, it would be possible to introduce more complex axonal geometries, such as non-linear axonal trajectories, while keeping intact the fundamental framework of PSO for programming DBSA's (equations 10 and 11). However, the activation prediction functions, R(x) and S(x), would need to be tuned to obtain reasonable predictions for the new, non-linear geometries. Future developments in activation predictions could be readily deployed into the PSO programming algorithm to facilitate robust prediction across stimulation parameters.

Because of this limitation on axonal geometry, biophysical models for the axonal geometry of interest must be constructed and run once as a primer for identifying an appropriate MAFT value. Since accurate prediction of axonal activation relied on the appropriate selection of a MAFT value, a poor choice of MAFT value would lead to suboptimal predictions. While this need for a small-scope biophysical model simulation adds an extra setup step in applying the PSO approach, the overall process remains computationally efficient. Another important limitation in the application of the PSO in this study is that we modeled only a single axonal pathway between thalamus and cortex. There are indeed several pathways that are likely activated during thalamic DBS, including the reticular nucleus to VPLo, the cerebellothalamic tract, and corticothalamic tract. Their activation as well as the dynamic synaptic modulation resulting from the activation may underlie components of the therapy.

2.4.4 Practical Considerations

The results on robustness highlight an important practical point for DBS lead placement and the capabilities of current steering algorithms. While the simulations in **Figure 2.7C-D** suggest that current steering is able to compensate for off-target placement, this ability of directional DBS leads may be limited to displacements of a couple of millimeters or less [108]. At larger displacements, current steering through a single lead of electrodes may not adequately compensate for off-target lead placement, depending on the size of the target.

For the VPL example demonstrated in this chapter, applications of the PSO to lead displacements of 3 mm yielded little to no activation of the ROI.

For proof-of-concept and consistency with other ongoing work in our group, the PSO approach presented here was implemented for a 32-electrode DBS array with four radial electrodes per row. However, PSO programming is readily applicable to the eight-electrode directional DBS leads that have recently emerged on the market, such as the Vercise and Infinity DBS systems. While any given row of these commercial DBS leads only has three radial electrodes, this reduced number of radial electrodes does not significantly diminish steering capabilities when current is allowed to be non-uniformly distributed across the electrodes [108]. As such, the PSO approach can be readily integrated into a system that uses such DBS leads, enabling the development of a system for efficient, subject-specific DBS programming.

The PSO approach was observed to be efficient by running in a matter of minutes. However, it is important to acknowledge that running the PSO algorithm requires a series of preparatory steps that include segmenting the target structures from subject-specific anatomical images, as well as specifying the trajectory of the axonal pathways. Ultimately, the PSO approach for DBS programming is intended for use in subject-specific contexts. As such, widespread use of the algorithm will require that DBS systems become streamlined for anatomically-informed, subject-specific DBS. We anticipate that this streamlining process will occur in tandem with the current developments in directional DBS, due to the complementary nature of these two technologies. For the time being, centers that already have the technical expertise to implement prospective subject-specific models can leverage the PSO approach to enable optimized programming of directional DBS leads.

2.4.5 Future Applications

The PSO algorithm demonstrated here was applied to a pathway thought to be involved in DBS therapy for treating Essential Tremor [80,125]. However, it could readily be applied to other known DBS targets. A number of DBS targets have been characterized in terms of

their relevant fiber tracts and morphologies using probabilistic tractography and/or histological processing in the context of computational neuron models of DBS. For instance, in Parkinson's disease, STN-DBS therapy is thought to stem from a combination of modulating pathways in and adjacent to the STN [84,85,126], and a similar combination of therapeutic pathways is thought to occur with GPi-DBS [127,128]. There is also ongoing research to characterize targets for other indications, such as in Major Depressive Disorder, where retrospective modeling suggests that the forceps minor, uncinate fasciculus, and cingulum bundle may play a critical role in the therapeutic DBS mechanisms [87]. It is important to note that the PSO approach presented here can be readily extended to cases in which there are multiple ROIs. In this case, the PSO algorithm could provide the user with a set of electrode configurations that intuitively demonstrate the tradeoff between stimulating one target vs. another target (i.e. via the Pareto Front).

In addition, one could also consider including other stimulation parameters such as bipolar/multipolar stimulation, a range of pulse widths, and potentially different stimulation pulse train patterns. The key to incorporating additional parameters would be to have a mathematical representation of how these factors influence axonal excitability. While this study used a simplistic homogeneous and isotropic model of tissue conductance to obtain extracellular potential values at the axonal nodes of Ranvier, one may consider using more complex models of brain tissue with the PSO algorithm. For example, studies have shown that finite element models that incorporate inhomogeneous and anisotropic tissue properties (assigning different conductance values to various tissue types) improve modeling results and may better reflect the physiological properties of the brain [85,104,129]. Finally, while the implementation presented here was designed for programming a set of electrodes that have already been implanted, it is conceivable to leverage the efficiency of this approach for pre-surgical planning of DBS lead placement. By simulating different lead placements (e.g. location, angle of attack, etc.) and aiming for the one that best achieves the objectives, one may be able to optimize lead placement and therefore improve targeting and functional outcomes of DBS.

2.5 Conclusion

We have shown particle swarm optimization to be an efficient, consistent, and robust method for programming DBS arrays. The proposed implementation provides the end-user flexibility to select among alternative configurations and objective function specification along the Pareto front to accommodate subject-specific needs.

Chapter 3
Particle Swarm Optimization for Deep Brain Stimulation Array Programming in the Globus Pallidus and the Subthalamic Nucleus

3.1 Introduction

Deep brain stimulation (DBS) lead technology for treating Parkinson's disease (PD) typically consists of four cylindrical electrode contacts stacked along a cylindrical carrier lead. When DBS leads are implanted in sub-optimal locations [78,86], or when target nuclei have non-spherical shapes [76], suprathreshold current can spread to adjacent structures and induce adverse side effects such as tetanic motor contractions [130], cognitive-motor difficulties [131], and impulsivity [132] that can present at lower amplitudes than those which are necessary to reduce parkinsonian motor symptoms. DBS leads with segmented electrodes around the lead circumference, and along the lead axis, have strong potential to improve current steering and focusing to potentially compensate for implantation at sub-optimal locations [133–135]. However, such segmented leads have substantial programming complexity that will result in unmanageable clinical visits to efficiently identify the ideal stimulation settings for each implant and user [136].

To aid the programming process of DBS arrays, a semi-automated particle swarm optimization (PSO) programming method was presented in Chapter 2. This algorithm is capable of performing non-convex, multi-objective optimization for maximizing prediction of activation in a single region of interest (ROI), minimizing prediction of activation in a single region of avoidance (ROA), and minimizing predicted power consumption [137]. In that study, we implemented the PSO algorithm with a high-density

32-channel DBS array in a thalamic model for treating essential tremor with a structure that is relatively simple in geometry. However, the algorithm could have strong impact if applied to DBS arrays for treating Parkinson's disease through stimulation of the subthalamic nucleus (STN) and globus pallidus (GP). These nuclei have complex fibers of passage, subcircuits [138–141], and oscillatory networks [142–149] that are likely to be critically important for the successful application of DBS therapy to treat PD [128,150–156].

The PSO algorithm described in Chapter 2 [137] implements in part an aggregate-based method that requires a formulation of an "objective function" to guide the evolution process. The objective function is a weighted linear sum of predicted activation of the ROI, ROA, and power. While adding more regions of interests and avoidances to the objective function is feasible, determining the weighting of each of the regions is non-trivial and subjective. For example, in a case where the region of interest has a significantly smaller number of cells compared to regions of avoidances, the weighting has to be heavily biased towards the ROI in order for it to be comparable to the ROAs. Therefore, the previous method of PSO implementation might not be suited to handle the complex geometry of the STN and GP, where potentially multiple ROIs and ROAs are required. In this chapter, we develop an updated version of the PSO algorithm using a Pareto dominance-based method [157], which allows multiple ROIs and ROAs to be simultaneously optimized without having to assign weights to form an explicit objective function.

In this study, we applied the algorithm to the globus pallidus internus (GPi) [158] and the dorsal lateral STN [159] as ROIs, while using the associative and limbic regions of the STN (ventral medial STN), and the arm representation in the corticospinal tract of the internal capsule (CST_{arm}) as ROAs. In addition to modeling the PSO with STN- and GPi-DBS, we also tested the performance of the PSO algorithm in a non-human primate by performing a collection of qualitative and quantitative measures of rigidity and gait metrics. We compared the results obtained from the PSO to four traditional monopolar review settings, as well as a sub-optimal random stimulation setting.

3.2 Methods

3.2.1 Animal Subject

One rhesus monkey (macaca mulatta, female) was used in this study (18 years old, 6.0 kg). All procedures were approved by the Institutional Animal Care and Use Committee of the University of Minnesota and complied with the United States Public Health Service policy on the humane care and use of laboratory animals. The monkey underwent a pre-operative 7T MRI and CT scan, and these data were imported into a preclinical neurosurgical navigation software called Preclinical Cicerone [160] to plan for two cranial chamber implants and two DBS lead implants. In a procedure under isoflurane anesthesia, the animal was implanted with two cranial chambers oriented primarily in the coronal (for GPe/GPi) and in the sagittal (for STN) planes over the right hemisphere. Electrophysiological mapping of the targets was performed to identify trajectories that included sensorimotor territories of the GPe/GPi and the STN (see next chapter for details).

Two versions of a segmented DBS array were fabricated by NeuroNexus Technologies as described previously [101]. The DBS arrays consisted of eight rows and four columns of electrodes wrapped around a hollow carrier tube (see **Fig. 1.2**). DBS arrays were advanced to the target with a stylet and anchored with epoxy to a c-ring that fit within a groove in the chamber. The connecting cable, which included an omnetics connector, were then externalized from within the cranial chamber and routed to a dry chamber on the headcap. A DBS array was placed within the STN volume in the sagittal plane at 35° above the horizontal plane, 4.8 mm lateral and 6.6 mm anterior to the stereotactic midpoint. This resulted in an implant through the STN and slightly medial to its centroid. The DBS array targeting the GPe and GPi was placed in the coronal plane 32° from the sagittal plane into the right hemisphere, 0.9 mm lateral, and 14.8 mm anterior to the stereotactic center. This resulted an implant in a coronal plane that spanned both GPe and GPi.

Subsequent to DBS array implantations, systemic MPTP injections were administered to the animal first over three consecutive days (0.5 mg/kg total), next over two consecutive days (0.6 mg/kg total), and finally over two consecutive days (0.6 mg/kg

total). Through these systemic MPTP injections, the subject was rendered into a stable, moderately severe parkinsonian condition as assessed by a modified Unified Parkinson's Disease Rating Scale (mUPDRS) [79].

3.2.2 Anatomical Segmentation and Fiber Tractography

Anatomical segmentation of the STN, GPe/GPi, and arm representation of the corticospinal tract of internal capsule (CST_{arm}) were performed on the pre-operative 7T MRI data. The STN, GPe, and GPi were segmented based on the 7T T2-weighted imaging, which has been shown previously to distinguish basal ganglia structures [161]. We further parcellated the STN into a dorsal-lateral (motor) region and ventral-medial (associative/limbic) region according to a 3D atlas [162]. Probabilistic tractography (in FSL) was used to segment the CST_{arm} region, guided by seed and way masks that were both segmented from the T2-weighted imaging data. These data were transformed into diffusion tensor space, and segmented in reference to an atlas [163] and fiber tract maps [164] of the rhesus macaque brain. A seed mask was created in the right hemisphere arm representation of the precentral gyrus associated with primary motor cortex, and a way mask was created within the right hemisphere peduncle at a point caudal to the STN.

We reconstructed the relative location of the DBS lead implant by coregistering the 7T pre-operative MRI scans to the post-operative CT scans in Avizo. The orientation of the DBS arrays were determined based on (1) fiducial markers on the DBS array that provided an estimate of the distal electrode orientations, (2) stimulation thresholds through a monopolar review of individual electrodes for inducing transient muscle contractions in the arm, and (3) stimulation artifact size on the DBS array in the GPe/GPi during monopolar review of stimulation through each electrode. The location and the orientation of the DBS arrays and the segmented volumes of STN and GPe/GPi were imported into preclinical Cicerone for visualization and into MATLAB for subsequent population of the volumes with cells and axons for modeling the effects of stimulation on individual fibers.

The STN, GPe, GPi were populated with cells and axons consistent with previous modeling studies [154,165]. The template STN cell contained an axon that traversed from

the STN towards the globus pallidus, whereas the GPi cell contained an axon that traversed from the GPi towards the thalamic fasciculus immediately dorsal to the STN. Two formulations of GPe cells were populated with one passing en passant through GPi en route to STN (Type II) and the other passing directly through the internal capsule en route to STN (Type III). If any part of a cell body, dendritic tree, or axon overlapped with a DBS array, the entire cell/fiber was removed from subsequent analysis. The STN was populated with 379 cells in the dorsolateral STN and 726 cells in the ventromedial STN [154]. Within the globus pallidus, 977 cells were populated within GPi and 952 cells were populated within GPe (Type II: 412 cells, Type II: 540 cells [165]). The CST_{arm} tract segmentation was randomly populated with 1000 splines that were segmented into myelinated axon cable models with a diameter of 10 μm [89] in alignment with measurements taken from the internal capsule in the rhesus macaque [167].

3.2.3 Subject-Specific Finite Element Models (FEMs)

Anisotropic tissue conductivity models were constructed from the 7T diffusion-weighted imaging data in the context of the DBS array locations and orientations within the STN and GPe/GPi. Specifically, the tissue conductance model was constructed using the "normalized volume" method [104,152]. In the model, a symmetric tensor representing the tissue conductance was calculated using eigenvectors calculated from each diffusion tensor

$$\Sigma = V\sigma V^T \quad (1)$$

where Σ is the tissue conductance tensor of a given voxel, V is the matrix of the orthonormal eigenvectors from a given diffusion tensor, and σ is the diagonal matrix containing tissue conductance in the primary, secondary, and tertiary directions where $\sigma_1 \leq \sigma_2 \leq \sigma_3$.

The approach also normalizes the volume of the diffusion tensor ellipsoid then scales the result by the isotropic conductance of the tissue type associated with that voxel. This method relies on the diffusion tensor eigenvalues and the known scalar tissue conductance for calculation of tissue conductance eigenvalues. Each diffusion tensor eigenvalue was normalized by the diffusion tensor ellipsoid and scaled by the isotropic

tissue conductance for each voxel as dictated by the subject-specific brain tissue segmentation.

$$\sigma_i = \frac{d_i}{\sqrt[3]{d_1 d_2 d_3}} \sigma_{iso} \quad (2)$$

where σ_i is the conductivity in the primary, secondary, or tertiary direction as indicated by the subscript; d_i is the diffusion tensor eigenvalue in the primary, secondary, or tertiary direction as indicated by the subscript; and σ_{iso} is the isotropic conductance of the tissue in which the diffusion tensor voxel resides. The tissue types modeled included white matter [168], gray matter [168], and cerebrospinal fluid (CSF) [169]. The isotropic conductivities used in equation (2) were 0.108 S/m for gray matter, 0.066 S/m for white matter, and 1.79 S/m for CSF. The permittivity was modeled as isotropic for all tissue types, and was selected to be 49600 for gray matter, 23734 for white matter, and 0 for CSF.

3.2.4 Axonal Cable Models

Extracellular voltages from the FEM solution for any given electrode configuration and stimulation parameter settings were extracted for each membrane compartment of each modeled cells and axons. These voltages were subsequently used in two contexts.

First, to predict the thresholds for eliciting action potentials within the modeled cells and fiber tracts, multi-compartment membrane cable models were constructed for the neural pathways described in Section 3.2.2. Membrane cable model biophysics for the STN, GPe, and GPi were consistent with those described previously [154,165]. Membrane cable model biophysics for CST_{arm} were consistent with those modeled previously [128]. DBS perturbations to these cable models used membrane compartment extracellular voltages from the FEM solutions in COMSOL and coupled them with the e_extracellular function in NEURON to approximate the driving function at each membrane compartment.

The second approach leveraged a simplified activating function [92,170] that estimated stimulus-induced transmembrane currents as a second spatial difference of the extracellular voltages at each adjacent compartment (e.g. adjacent nodes of Ranvier within an axon model). This approach was further modified as described previously using a

modification that skipped one node of Ranvier on either side of the node under study in the calculation of the activating function. The modified activating function thresholds (MAFTs) were adjusted to match the stimulus thresholds for the STN, GPe, GPi, and CSTarm pathways as defined by the NEURON model simulations. The process for this calibration was identical to that described by Peña, Zhang, et al. [137]. The MAFT factors for the dorsal-lateral STN, ventral-medial STN, GPi, and both GPe cell types were all determined to be 0.01357, while the CST_{arm} axons were determined to be 0.00248.

3.2.5 Pareto Dominance-Based PSO Algorithm for Identifying DBS Array Settings

The MAFT approach provides an efficient metric to estimate axonal activation adjacent to DBS arrays, and this approach was used in the context of a PSO algorithm for identifying DBS array settings that have the highest likelihood of activating an ROI, limiting activation in an ROA, and minimizing overall power consumption. A previous version of the PSO algorithm for programming DBS arrays leveraged an aggregate-based method in which the social velocity pointed towards the global best as determined by the aggregate objective function [137]. To enable optimization for multiple ROIs and ROAs, the PSO algorithm was modified such that the social velocity pointed towards a random point on the Pareto front [157]. All other parameters and termination criteria for the PSO were selected based on the algorithm described previously [137], with the exception that the social attraction weight was lowered to 0.1 to promote more exploration, and the max cathodic current bound per contact was capped at -0.2 mA to ensure that stimulation stayed within safe charge density limits (<30 $\mu C/cm^2$) for platinum electrode sites on the STN-DBS array [171].

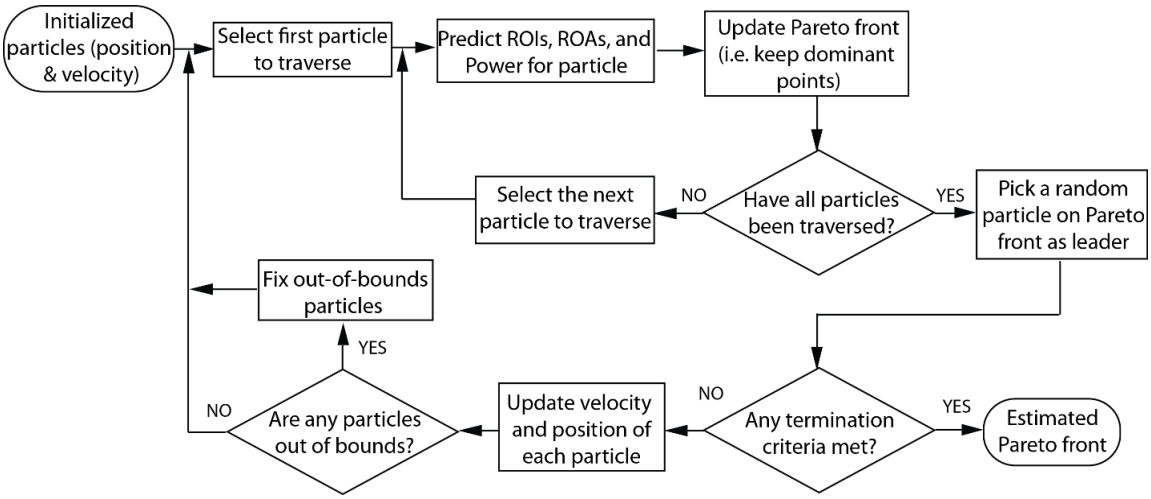

Figure 3.1: *Dominance-based PSO algorithm. The algorithm involves building a Pareto front based on dominant particle positions within the multi-dimensional space of ROIs, ROAs, and power consumption.*

Table 3.1: *Dominance-based PSO Algorithm Parameter Values*

Parameter	**Value**
Number of Particles	100
Generation Limit	200
Stalling Generation Constant	100
Cognitive Attraction Weight, c_1	4.5
Social Attraction Weight, c_2	0.1
Upper Inertia	0.9
Lower Inertia	0.4
Velocity Limit	Infinite
Additional Cognitive Weighting, r_{1ij}	[0,1] (random)
Additional Social Weighting, r_{2ij}	1
Lower Bound Current per Contact	-0.2 mA
Upper Bound Current per Contact	0 mA
Total Bounded Current	none

3.2.6 Determination of Test Stimulation Amplitudes and Electrode Configurations

Behavioral evaluation of the STN-DBS array stimulus settings was performed in the context of both grouped monopolar electrode settings and PSO-derived electrode settings. The latter consisted of maximizing ROI activation and matching all monopolar review settings in terms of overall power. Each monopolar review setting contained eight active electrodes (to match the surface area of a scaled-down version of the human DBS lead with cylindrical electrodes, [101]) and had equal current distributed through each electrode. The monopolar settings were named C0 (distal), C1, C2, and C3 (proximal). In cases of non-functional electrodes in the monopolar review settings, the next adjacent electrode along the same column was used. In addition, we also generated a random setting that had matching power to the final PSO setting and the monopolar review settings by assigning currents to random contacts based on the number of contacts and the relative amplitudes used in the final PSO setting.

For each experimental session, electrical stimulation was delivered to either the monopolar review settings, PSO setting, or randomized PSO setting in increasing stimulus amplitudes to identifying stimulus thresholds for evoking muscle contractions about the upper and lower extremities (TDT system, 50-200 μA, 130 Hz, 90 μs cathodal leading pulse for 1 sec). The threshold at which an arm movement was elicited was defined as the side effect threshold. A so-called test threshold was set to be 75% of the recorded side effect threshold. This process resulted in seven test settings (1 PSO setting, 4 monopolar review settings, 1 randomized PSO setting, and 1 sham stimulation setting). All experimental tests used 100 Hz and biphasic waveforms with a 100 μs cathodic phase followed by a 300 μs anodic phase.

3.2.7 Clinical Evaluation of Parkinsonian Motor Signs

For rigidity testing, two experienced evaluators, blinded to the test setting, first evaluated the rigidity of the animal on a scale of 0 (no rigidity) to 3 (severe rigidity) before the onset of stimulation or sham stimulation (lower amplitude). STN-DBS was then performed on any one of the test settings, and the evaluator assessed upper and lower limb rigidity after 6 minutes of continuous STN-DBS. Stimulation was turned off after the clinical evaluation (typically 10 minutes of total stimulation), and a 30 minute wash-out period occurred prior to evaluation of a subsequent setting. The animal also received a sham stimulation, which was set to be 10% (instead of 75%) of the side effect threshold of the therapy setting for C3. Rigidity testing was repeated again using either STN-DBS (including a randomized setting instead of sham). The evaluator then proceeded to evaluate upper and lower limb rigidity after 20 minutes of continuous STN-DBS. In this case, the subject received an hour-long wash-out period prior to testing a subsequent stimulation setting.

To test for self-initiated ambulation patterns, the subject was evaluated in an unrestrained environment. The habitrail consisted of two end compartments with food hoppers connected by a 2.43-meter-long tunnel, in which an HR Walkway 4 VersaTek system pressure walkway (Tekscan, Inc) was adhered to the floor. The pressure walkway contained 33,400 force sensors (4 sensors/cm^2) that rapidly quantified the kinematics of the animal's gait. Prior to entering the habitrail tunnel, the primate received STN-DBS for 30 minutes through a 16-channel, independent current-controlled neurostimulator (Precision, Advanced Bionics) that was attached to the subject's headpost and protected by a form fitting thermoplastic headcap. Stimulation amplitudes were set to 75% or 98% of the response threshold for eliciting motor contraction side effects. The stimulus pulse patterns consisted of 130 Hz, 100 μs cathode-leading biphasic pulses with a prolonged anodal phase (3 ms). Experimental session results with the same stimulation settings were combined across days. The animal performed 12, 10, 13, 11, 17, 11, and 26 ambulatory passes across the gait mat for C0-C3, PSO, random PSO, and DBS-OFF (control) settings respectively for the 75% side effect threshold experiment; and 8, 1, 8, 2, 12, 1, and 10 ambulatory passes across the gait mat for C0-C3, PSO, random PSO, and DBS-OFF

(control) settings respectively for the 98% side effect threshold experiment. The gait data were analyzed offline using Walkway Research (Tekscan Pressure Measurement System v7.66-05). Gait boxes were drawn around the sensed pressure area for each strike and demarcated into right/left front and right/left hind limbs. Gait cycle time, defined as the time for a complete gait cycle to pass (i.e. cycling through all four limbs) was calculated.

3.3 Results

3.3.1 DBS Array Locations and Orientations

Two multi-channel DBS arrays were implanted ipsilateral to each other targeting the right hemisphere STN and GPe/GPi (**Fig. 3.2**). In the STN-DBS array, columns 3 and 4 faced towards the internal capsule, whereas in the GPe/GPi-DBS array, columns 1 and 4 faced towards the CST_{arm}. The STN-DBS array was implanted along a parasagittal trajectory such that the DBS lead body passed through the ventral medial STN with electrode rows 1-5 in the STN. The GPe/GPi-DBS array was implanted along a pseudo-coronal trajectory with electrode rows 3-7 in GPe and rows 0-2 in GPi.

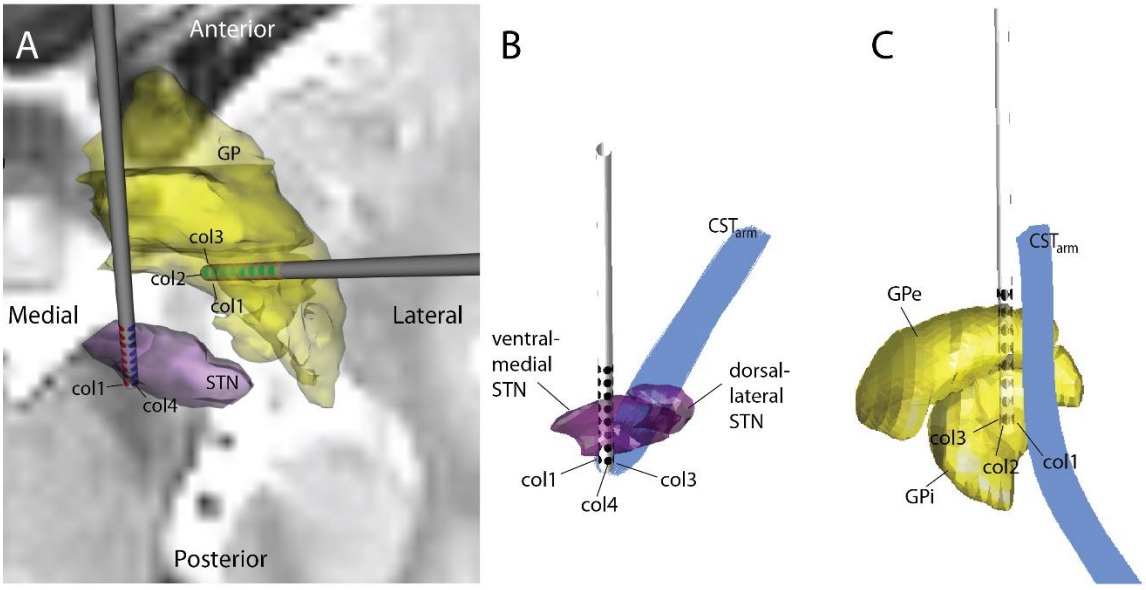

***Figure 3.2**: DBS array implants in the STN and GPe/GPi. (A) Axial view of STN- and GPe/GPi-DBS implant locations and orientations in relation to their structures. (B) Reconstruction of STN showing both the dorsal-lateral and ventral-medial regions with the DBSA implant as well as the arm representation of the corticospinal tract of internal capsule (CST_{arm}). (C) Reconstruction of the globus pallidus showing both GPe and GPi with the DBS array implant as well as CST_{arm}.*

3.3.2 Pareto Front Solutions

The PSO algorithm was run for the GPe/GPi-DBS array in the context of maximizing GPi activation, minimizing GPe/CST_{arm} activation and minimizing the overall current amplitude. The resulting output of the PSO algorithm was a collection of solutions arranged on a multi-dimensional Pareto front. This front contained predicted percent activation for the ROI and both ROAs as well as the corresponding currents through all electrodes, which can be a surrogate for power. While many dimensions can exist within a Pareto front, only three dimensions of the Pareto front are suitable for visualization. An example of the PSO-derived Pareto front is shown in **Fig. 3.3A** for the GPe/GPi-DBS array in Subject N. Two solutions along the Pareto front are shown with the first (**Fig. 3.3B**) exhibiting the strongest number of GPi cells affected (103/977) with minimal GPe cell activation (37/952) and a relatively large number of CST_{arm} fibers activated (351/1000). If one considers reducing the number of GPi cells activated, one can achieve a substantial reduction in CST_{arm} activation as shown in **Fig. 3.3C** for another PSO derived electrode configuration. In this case, 87/977 cell in GPi were activated within the model, whereas 32/952 GPe cells and 78/1000 CST_{arm} fibers were activated. For both electrode configurations, total current amplitude was consistent at 2.56 mA.

The PSO algorithm was also applied to the STN-DBS array in the context of maximizing activation within the dorsal-lateral STN (ROI) and avoiding activation within the ventral-medial STN and CST_{arm} regions (ROAs). An example of the Pareto front is shown in **Fig. 3.4** for the dorsal-lateral STN activation, CST_{arm} activation, and current amplitude. The monopolar review settings as well as the random setting were back-

projected onto the Pareto front. Comparing these results, the PSO setting resulted in the largest activation of the dorsal-lateral STN, while maintaining comparable activation of the ventral-medial STN and the CST_{arm} pathways to other monopolar review settings (Table 2). Notably, for the monopolar review settings, C1 had the largest activation of the dorsal-lateral STN and the electrodes engaged by C1 used rows on the DBS array that were comparable to those defined by the PSO algorithm. However, the C1 configuration also had larger ventral-medial STN and CST_{arm} activation that that found with the PSO setting.

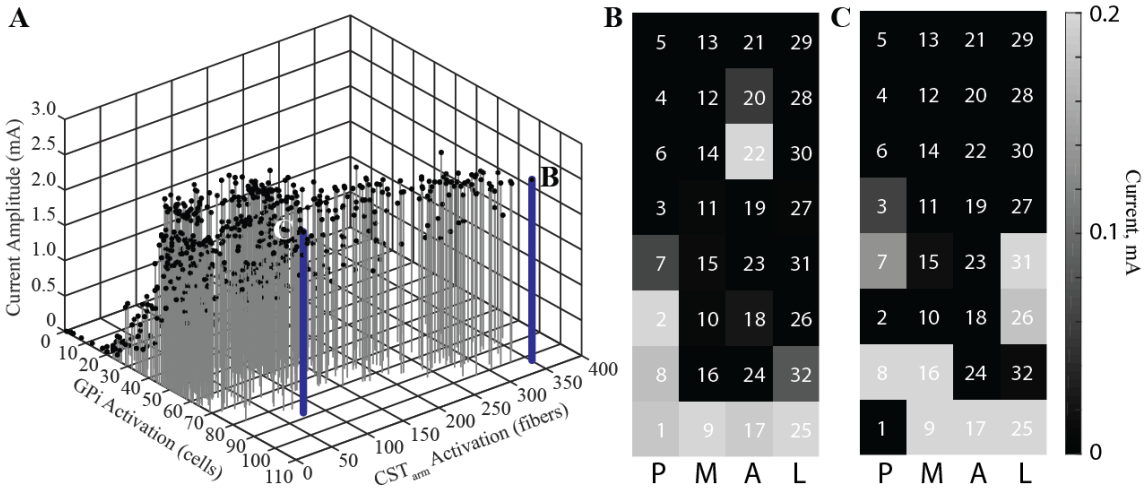

Figure 3.3: *Comparison of electrode configurations for the GPi-DBS array. (**A**) Pareto front of the PSO solutions. Electrode configurations are shown for two examples with strong GPi cell activation with one (B) having a larger activation of CST_{arm} than the other (C). P: posterior, M: medial, A: anterior, L: lateral.*

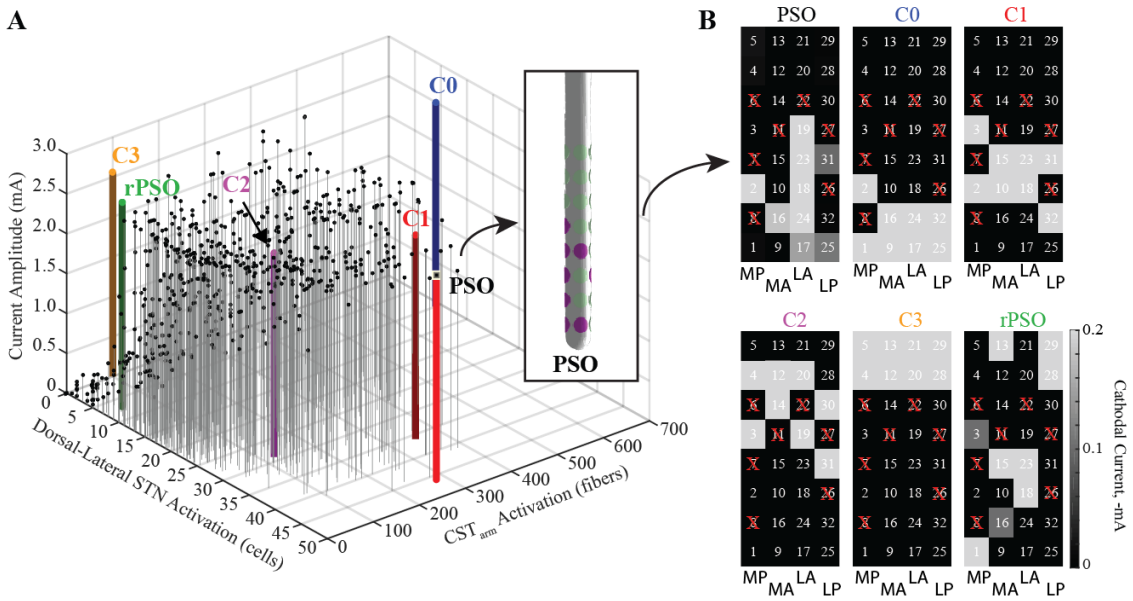

Figure 3.4: *Comparison of electrode configurations for the STN-DBS array.* ***(A)*** *Pareto front of the PSO solution with back-projected results from the monopolar review settings and the PSO random setting. (B) Final configurations for all setting with red "X" marking non-functional electrode sites. C. Pareto front of the PSO in GP. D. An example of a configuration off the Pareto front, showing the electrode configuration and orientation. MP: medial posterior, MA: medial anterior, LA: lateral anterior, LP: lateral posterior.*

Table 3.2: *Comparison of Predicted Pathway Activation for the STN-DBS Array*

Parameter	**PSO**	**C0**	**C1**	**C2**	**C3**	**rPSO**
Dorsal-Lateral STN (n=379)	46	10	36	29	0	7
Ventral-Medial STN (n=726)	224	222	250	306	187	139
CST_{arm} (n=1000)	282	689	350	122	100	41

3.3.3 Therapy Settings

While the model-derived stimulus settings leveraged the same total current amplitudes, in practice one can increase current amplitudes until the emergence of side effects resulting

in different current amplitudes for each electrode configuration. In the case of the models, if a specific proportion of CST_{arm} fibers activated was known to elicit a persistent muscle contraction, one could impose a limit of CST_{arm} activation such that the model solutions would not be able to exceed this value. In the case of the primate experiments, we used a comparable protocol by first identifying the maximum total current allowable before eliciting muscle contraction side effects for each electrode configuration and then used 75% of that stimulus intensity. Motor side effect thresholds were found to be 160, 170, 160, and 130 µA per electrode for C0, C1, C2, and C3 electrode configurations, respectively. The motor side effect thresholds for the PSO and random PSO settings were determined to be 157 and 136 µA per electrode, respectively. Thus, the actual per-electrode current (delivered through eight electrodes) used for the test settings for C0-C3 were scaled to be 120, 128, 120, and 98 µA, respectively (total of 0.96, 1.02, 0.96, 0.78 mA respectively). The current used for PSO setting was 106 µA through electrodes 2, 16, 18, 19, 23, 24 and 100 µA through electrodes 17, 25, 31 (total of 0.94 mA). The current used for the random PSO setting was 102 µA through electrodes 1, 13, 15, 18, 23, 28, 29 and 51 µA through electrodes 3 and 16 (total of 0.82 mA).

3.3.4 Blinded Evaluation STN-DBS Array Settings on Parkinsonian Rigidity

Parkinsonian rigidity was quantified with the mUPDRS on a scale from 0 (no rigidty) to 3 (severe rigidity) with the assessors (n=2) blinded to the stimulus setting: four STN-DBS array monopolar review electrode configurations, the STN-DBS array PSO electrode configuration, and a control condition. For the blinded evaluation 6 minutes after stimulation onset, the control condition consisted of a reduction in stimulus amplitude from the C2 configuration (0.96 mA total). For the evaluation 20 minutes after stimulation onset, the control condition consisted of a random selection of electrodes within the DBS array using current relative amplitudes consistent with the PSO-derived stimulus setting. With upper extremity rigidity, the PSO-derived setting resulted in the largest reduction in rigidity (-38% and -42%) for the 6- and 20-minute evaluation points, respectively. With lower

extremity rigidity, the PSO-derived setting resulted in comparable but slightly lower reduction in rigidity (-26%) to all the other monopolar review therapy settings (-21% to -32%) in the 6-minute evaluation, and a significantly better therapy compared to the sham setting (-6%). In the 20-minute blinded evaluation case, the PSO-derived setting resulted in the largest reduction (-30%) compared to all other settings.

***Figure 3.5**: Blind evaluation of parkinsonian rigidity across STN-DBS array settings. Rigidity reduction in the (A) upper and (B) lower extremities after 6 minutes of stimulation. Also shown is rigidity reduction in the (C) upper and (D) lower extremities after 20 minutes of stimulation.*

3.3.6 Quantitative Assessment of STN-DBS Array Settings on Gait

Gait cycle times for each of the stimulation settings were summarized in **Fig. 3.6**. In the 75% side effect threshold stimulation experiment, the gait cycle times were found to be 1.37, 1.28, 1.39, 1.21, 1.32, 1.24 and 1.81 seconds for C3-C0, PSO, random, and DBS-OFF (control) settings, respectively. In the 98% side effect threshold stimulation experiment, the gait cycle times were found to be 1.88, 1.81, 1.24, 1.38, 1.36, 1.81 and 3.77

seconds for C3-C0, PSO, random, and DBS-OFF (control) settings, respectively. PSO therapy setting did not show any significant difference from all the other settings in gait cycle time; however, the PSO was as effective at reducing the gait cycle time as all the other settings compared to control.

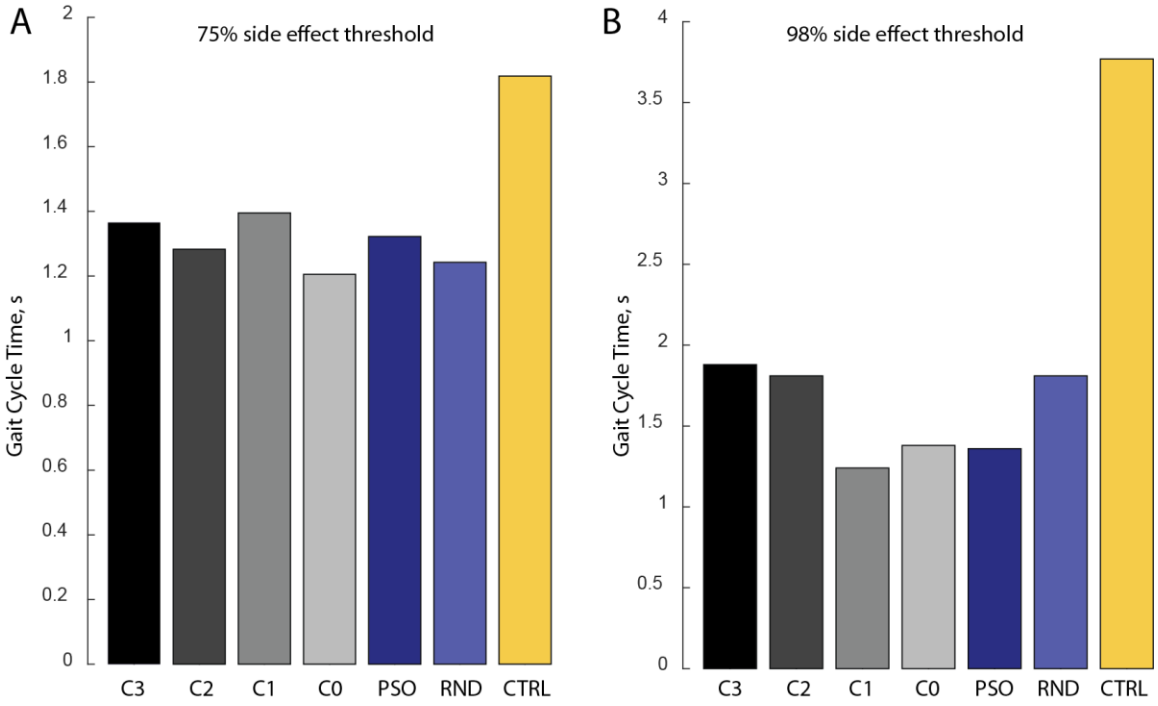

Figure 3.6: *Gait analyses showing (A) Gait cycle time for all therapy settings for stimulating at 75% of side effect threshold and (B) 98% of side effect threshold.*

3.4 Discussion

In this study, we described an improved method of dominance-based particle swarm optimization for programming DBS arrays in the STN and GP. This algorithm is now capable of handling multiple ROIs and ROAs simultaneously without the need of an objective function, and is as robust and reliable as the previously described method [121]. In addition, we tested the performance of one of the configurations obtained by the new algorithm against traditional monopolar review settings and a randomly chosen setting in

an STN-DBS array in a parkinsonian non-human primate. The result demonstrated that the PSO-derived setting was at least or more effective than all other settings tested for rigidity, especially in the context of relieving upper and lower extremity rigidity after a 20-minute wash-in period. We also tested gait parameters by training the non-human primate subject to walk across a platform with pressure sensors in a self-initiated manner. The data suggested that the PSO-derived setting showed comparable therapy levels to other settings in reducing gait cycle time.

3.4.1 Particle Swarm Optimization: Future Directions

It has been demonstrated that the orientation of a neuron has a large effect on neuronal activation caused by electric stimulation [172,173] and thus affecting the MAFT factors that the PSO rely on to determine activation. In this study, axon trajectories were set based on modeling studies [151,154] that had limitations on their orientations within the structure as well as their trajectories outside of the structure. For example, GPi axons often follow a long and tortuous course within the GPi before emerging either through the ansa lenticularis or the lenticular fasciculus, and the exact passage of the GPi axons based on their location in GPi is less studied and not well understood [174]. In addition, fiber pathways surrounding the basal ganglia such as the ansa lenticularis or the lenticular fasciculus mentioned above, the reciprocal STN-GPe projections, the putamen-GPe projections, STN-SNr projections, nigrostriatal fibers, medial lemniscus, and brainstem efferent fibers are also likely to be affected by GPe/GPi- and/or STN-DBS. These fibers were not modeled in the current study, although they could be incorporated into the PSO algorithm as ROIs or ROAs.

Additionally, similar to the STN's segmentation into motor and associative/limbic subregions in this study, GPe/GPi also contain several subregions where supplementary motor area receives projections from the dorsal region of GPi, premotor cortex from the ventral-lateral region of GPi, and primary motor cortex projections in between [138].

Further segregating these functional sub-territories within STN and GPe/GPi could provide more refined targeting of the PSO algorithm.

In the current generation of the PSO algorithm, we enabled simultaneously optimizing for multiple ROIs and ROAs; however, all the optimizations thus far have been limited to spatial parameters. Temporal parameters such as pulse waveform shape, pulse width, timing of pulses, bursting patterns can also have strong effects on clinical outcomes of DBS therapy. In future iterations of the PSO algorithm, temporal parameters could be incorporated to achieve spatial-temporal optimization of DBS therapy.

3.4.2 Optimization for Different Motor Signs

Numerous studies have suggested that in order to optimally treat different parkinsonian motor signs, different targets and neural pathways need to be stimulated [45,84,128,175–180]. There is a need to understand the relationship between these targets, sub-territories, or pathways to the motor signs. In our experiments, we observed that rigidity was improved most strongly with PSO-derived settings in comparison to all other DBS settings tested. For other motor signs such as akinesia and bradykinesia, the PSO approach did not substantially differ from other monopolar settings using grouped rows of electrodes. This suggests that there may not be a single stimulation setting that could alleviate all parkinsonian motor signs optimally. While we used GPi and dorsal-lateral STN as ROIs in this study, there is evidence that stimulation of the GPe [128,175,179,181] may be beneficial on bradykinesia and akinesia symptoms. Further supporting this dichotomy between high frequency stimulation of the GPe versus GPi was shown in the non-human primate model in which GPi-DBS inhibited activity within the pedunculopontine nucleus, a brainstem region involved in gait initiation [182,183] and known to partially degenerate in Parkinson's disease [184]. Additionally, there is evidence supporting the concept of targeting neural pathways outside the dorsal-lateral STN to treat specific motor signs of Parkinson's disease with DBS. Butson and colleagues showed through post-hoc modeling analysis of patient DBS lead locations and clinically optimized stimulation settings that the regions most strongly associated with improvement in rigidity and bradykinesia were

dorsal and medial to the STN, putatively within the thalamic fasciculus [84]. Notably, these target regions were slightly different for rigidity and bradykinesia with the former hotspot more lateral to the latter hotspot. There are also studies supporting the role of the cerebello-thalamic tract in the therapeutic mechanisms of STN-DBS for treating resting tremor [185]. The novelty of the algorithm in this study is that the dominance-based PSO approach is capable of specifying any ROI or multiple ROIs, and therefore, in future applications of the algorithm, one could augment multiple targets or ROIs into the implementation by modeling all the putatively therapeutic pathways around the target. This might increase the efficacy of the algorithm and may more broadly alleviate multiple parkinsonian motor sign.

3.4.3 PSO and Gait

Most PD symptoms including resting tremor, rigidity, bradykinesia are thought to stem from a loss of dopaminergic neurons in the substantia nigra pars compacta [158]. These motor signs can be alleviated by dopamine replacement treatment, and are typically more responsive to DBS [151]. Gait dysfunction and especially freezing of gait, on the other hand, is less consistently managed by current treatments [186,187]; yet, gait dysfunction is reported to be one of the most debilitating symptoms of the disease [188,189]. Parkinsonian gait in humans is characterized by stooped posture, shuffling steps, and can lead to freezing of gait and challenges with gait initiation. This has been quantified as a reduction in walking speed and stride length, an increase in the cadence of gait and high stride-to-stride variability of the gait cycle timing [187,190–192]. In both parkinsonian humans and research animals, sudden freezing of gait can lead to falling and difficulties when turning [193,194].

DBS in traditional targeting areas such as STN or GPi have shown mixed results [195], and benefit of DBS in the STN and GPi could be confounded by reduction in bradykinesia or rigidity of the limbs that facilitates a beneficial effect on gait [187]. Furthermore, gait improvement with DBS usually takes hours to wash in [151], which may stem from plastic reorganization of the gait network that takes longer to affect [196]. In our

experiment, we stimulated for half an hour before testing the subject with the ambulation task in the habit trail. However, it is possible that DBS therapy had not yet reached its full effect. In this study, PSO showed no superiority in reducing gait related motor signs than other stimulation settings in terms of temporal parameters such as gait cycle time in both the 70% and 98% side effect threshold experiments. Notably, the DBS-OFF condition produced the largest gait cycle time, consistent with the literature and our intuition that the animal will take longer to ambulate across the gait mat due to frequent freezing episodes and overall more severe rigidity, bradykinesia, and akinesia. All settings were able to produce better therapy than DBS-OFF (control) condition, largely due to the akinetic episodes happen less frequently. One additional parameter that the gait mat was not able to quantify was turning. In numerous control trials and monopolar reviewer therapy settings and the random setting, the subject was observed having difficulties turning at the end boxes (data not shown). In future studies, this phenomenon could be better quantified with the addition of end box camera recordings and additional gait mats.

Overall, gait is a complex motor task necessitating active communication amongst structures such as motor cortical areas, cerebellum, basal ganglia, thalamus, brainstem and the spinal cord, which involve other signaling pathways beyond just dopaminergic signaling. Further modeling and studies might help with pinpointing the structure or circuit that is involved in PD gait function. Once the circuit is identified, the PSO algorithm is poised to facilitate targeting stimulation to the relevant pathways for treating gait dysfunction.

3.4.4 PSO Result Selection

In this study, we chose the final solution based on the maximum ROI activation. However, one can choose any of the configurations arranged on the Pareto Front based on the priority of activating more ROIs, or avoiding more ROAs, or minimizing power. As thousands of points could be collected on a single Pareto front, results selection can quickly become another tedious and time-consuming task. One possible solution to this issue is utilizing the ability of the DBSA to simultaneously record physiological signals such as local field

potential (LFP) signals during stimulation and promote the selections of electrodes that showed the most robust biomarkers. However, another challenge with high density arrays is that the biomarker (for example, beta band power) might not be evenly distributed across the array. This adds a new layer of complexity to using electrophysiological signals to guide the PSO result selection. To investigate the distribution of the potential biomarkers and the sensing ability of the DBSA, more thorough studies need to be conducted, and this will be explored in the next chapter.

3.4.5 Limitations of the Current Study

In our *in vivo* experiment testing DBS settings, we matched the power of the monopolar review settings and the random setting to PSO setting. However, the amount of current used for the actual therapy setting was adjusted based on the threshold at which a motor response was observed in the arm via stimulation of CST_{arm}. This implies that the final settings used in providing therapy did not have equal power output. This experimental design was aimed at answering a more clinical question: what is the maximum therapy that monopolar review DBS settings could provide, and can a PSO setting do better than that? From a scientific perspective, one might also be interested in whether using the same stimulation current among all therapy settings (matching power) could show more improvements in PD motor signs. We did not explore this question in the current study.

Also in our *in vivo* STN stimulation experiment, we matched the simulation results of CST_{arm} activation to the actual threshold at which a motor response was observed by running both the NEURON simulations and the *in vivo* testing with the same stimulation parameters. However, matching the simulation and *in vivo* experiments required the diameter of CST_{arm} to be set to 10+ µm because lower diameters of CST_{arm} showed severe underprediction with any stimulation setting. Previous studies [197–202] have shown that CST_{arm} fibers have diameters ranging 2 to 10+ µm, and the large diameter fibers represent some of the most excitable neural elements around the STN region. A systematic study of CST_{arm} model predictions and evaluation of these predictions *in vivo* would help to improve the accuracy of CST_{arm} predictions. We also only modeled the arm section of the

corticospinal tract in this study. The leg and face regions of the corticospinal tract could also be modeled and incorporated into the ROAs, with their independent MAFT factors.

In addition, the stimulation setting with the most predicted dorsal-lateral-STN (ROI) activation that the PSO could achieve was 46/379 cells (12%). This was due to the medial location of the DBS array, making stimulation of dorsal-lateral STN hard to achieve without activating ventral-medial-STN cells. This could also explain why the therapeutic effect size on rigidity reduction in vivo in STN was relatively modest (-30%). Notably, modeling of C1 monopolar review setting predicted the largest dorsal-lateral STN activation (36/379 cells, or 9%), and C1 did show the second overall best rigidity reduction in both the upper and lower extremity.

3.5 Conclusion

In this study, we developed a dominance-based PSO algorithm to program DBS arrays in both STN and GPe/GPi targets. The algorithm was able to handle multiple ROIs and ROAs without having to assign a weight to each to form an "objective function." We also tested the clinical efficacy of the solutions obtained by the PSO algorithm in the STN of a non-human primate. The PSO stimulation setting exhibited greater reduction in rigidity compared to grouped electrode monopolar review settings and a randomized setting. The PSO setting also exhibited comparable therapy to the best of the monopolar review settings in reducing gait cycle time during ambulation over a gait mat.

Chapter 4

High-resolution Local Field Potentials Measured with Deep Brain Stimulation Arrays in the Naïve and Parkinsonian Subthalamic Nucleus and Globus Pallidus

4.1 Introduction

Closed-loop approaches to deep brain stimulation (DBS) therapy, in which neurophysiological feedback is used to adapt the parameters of stimulation, hold promise for improving treatment consistency, minimizing induction of side effects, and reducing the frequency of replacement surgeries for implantable pulse generators with primary cells. Recent applications of closed-loop approaches to DBS therapy for treating Parkinson's disease (PD) have relied on sampling local field potential (LFP) activity from a pair of millimeter-scale cylindrical macroelectrodes along the DBS lead and then using spectral features of those signals to determine when and how to stimulate [203,204]. While retrofitting DBS lead macroelectrodes for recording purposes has been convenient to date for implementing closed-loop DBS in clinical settings [135,205], the dimensions of and spacing between each macroelectrode in the bipolar recording pair very likely undersamples the spatial heterogeneity of the oscillatory sinks and sources within the target nucleus [206,207].

Previous studies using monopolar or bipolar electrode configurations have noted that typical targets of DBS therapy for PD, including the subthalamic nucleus (STN) and the globus pallidus internus (GPi) / externus (GPe), can exhibit notable spontaneous and

task-related oscillatory activity in the healthy [208–213] and parkinsonian conditions [149,207,209,214–220]. However, studies have also found significant inter-subject variability in the power and specific frequency bands of such oscillatory activity in human [206,219,221–224] and non-human primates [209,221–223]. Such variability could stem from physiological differences within the sampled target amongst subjects, but the differences could also reflect the degree to which recording electrode dimensions, locations, and configurations can faithfully limit electrical shunting of oscillatory dipole activity in the regions of interest [225] and at the same time remove interference from far-field oscillatory sources [224].

This study investigated the hypothesis that DBS leads with smaller, segmented electrodes will uncover increased heterogeneity of LFPs within basal ganglia targets of DBS therapy. Preliminary evidence from acute intraoperative human studies leveraging DBS arrays indeed suggests that oscillatory activities in the STN has a finer spatial resolution than what is detectable with commercially-available DBS leads with four cylindrical macroelectrode contacts [214]. What remains unclear, however, is the degree to which this concept varies amongst the primary DBS targets for treating PD – that is, the STN and GPe/GPi. Additionally, little is known on the degree of spatial heterogeneity of oscillatory activity in these targets across behavioral states (resting versus active) and between naïve and parkinsonian conditions. To investigate these questions, DBS arrays with electrodes segmented both along and around the lead body [101] were chronically implanted within the STN and within the GPe/GPi in two non-human primates rendered parkinsonian with MPTP (1-methyl-4-phenyl-1,2,3,6-tetrahydropyridine).

4.2 Materials and Methods

4.2.1 Animals

Two rhesus monkeys (*macaca mulatta*, female) were used in this study (Subject G, 17 years old, 9.0 kg; Subject N, 18 years old, 6.0 kg). All procedures were approved by the Institutional Animal Care and Use Committee of the University of Minnesota and complied

with the United States Public Health Service policy on the humane care and use of laboratory animals. The animal subjects were provided with environmental enrichment, water *ad libitum*, and a range of food options including fresh fruit and vegetables. All efforts were made to provide care and alleviate any discomfort for the animals during the study. Both animals underwent pre-operative 7T MRI at the Center for Magnetic Resonance Research at the University of Minnesota using a passively shielded 7T magnet (Magnex Scientific) using methodology described previously [110].

4.2.2 Cranial Chamber and DBS Implants

Under isoflurane anesthesia, each animal was implanted with a titanium headpost (Gray Matter Research) and two cranial chambers (Crist Instruments) over the right hemisphere. The orientation and position of each cranial chamber was guided by a preclinical neurosurgical navigation software called *Monkey Cicerone* [166] in Subject G and *Preclinical Cicerone* [160] in Subject N. This program enabled 3D visualization of prospective DBS lead implant trajectories with the goal of targeting the GPe, GPi, and STN and further avoiding trajectories through large sulci, ventricles, and primary motor cortex. A post-implant CT scan was used to verify chamber placement and plan for the DBS lead implantation in *Monkey Cicerone/Preclinical Cicerone*.

4.2.3 Microelectrode Mapping

A Narishige microdrive was attached to each chamber and used to guide a microelectrode (250 μm diameter, 0.8-1.2 MΩ, FHC) through a dura-penetrating cannula into the brain. Approximately five microelectrode tracks were performed for each target to locate and then map the sensorimotor territories of the GPe/GPi and the STN [226–228]. Firing rate and patterns of isolated neurons in each of the targets were used to localize the borders of each nucleus of interest. Sensorimotor territories within these nuclei were identified as those containing neurons whose firing rate was modulated by passive or volitional joint movements. The location of the recording tracks relative to the corticospinal tract of internal capsule was determined using microstimulation (50-200 μA, 300 Hz, 0.5 sec) to

evoke movement of the face, upper extremity, and lower extremity. For both subjects, the GPe/GPi target was mapped and implanted with a DBS array prior to the mapping and implantation of the ipsilateral STN.

4.2.4 DBS Array Implant

The same Narishige microdrive used for the initial mapping experiments was also used for the DBS array implant. Two versions of a segmented DBS array were fabricated by NeuroNexus Technologies as described previously [101]. The DBS arrays consisted of 32 ellipsoidal electrodes arranged in eight rows and four columns around a 600 µm diameter shaft, with electrode diameters of 360 µm x 460 µm for the STN implant and 370 µm x 470 µm for the GPe/GPi implant. Center-to-center electrode pitch along the axis of the DBS lead was 572 µm and 750 µm for the STN- and GPe/GPi-DBS arrays, respectively. Following the implant of the two DBS arrays, a CT scan was performed in each subject to localize the array positions within the context of the pre-operative MRI. DBS array orientation was determined using two approaches. First, each DBS array assembly had a flexPCB cable extending from the lead body within the cranial chamber. This assembly served as a fiducial for the alignment of electrode columns located distally along the lead shank. Prior to implantation, each DBS array was inspected under the microscope to confirm this alignment. Additionally, stimulus-induced muscle contractions resulting from putative activation of the corticospinal tract of internal capsule were measured. The threshold amplitudes along rows of electrodes were used to identify the electrode contact(s) that most closely faced the internal capsule and further confirmed results from the fiducial analysis. Additionally, for the STN-DBS array in Subject G, EMG surface electrodes were placed on the forearm and bicep, and capsule-evoked EMG potentials were measured directly in lieu of visual observation.

4.2.5 Impedance Spectroscopy Measurements

Prior to and following implantation of each DBS array, electrochemical impedance spectroscopy measurements were performed on each electrode site using an Autolab

potentiostat (PGSTAT12, Metrohm). Following implantation, electrode site impedances varied from approximately 10-300 kΩ at 1 kHz and 200-700 kΩ at 20 Hz. Sites that fell outside these ranges were deemed non-functional and were excluded from further analysis to avoid biasing LFP signal analysis.

4.2.6 Local Field Potential Recordings

Monopolar LFP recordings were sampled concurrently at 1.375 kHz from the 32 electrodes on the STN-DBS array and 32 electrodes on the GPe/GPi-DBS array through an Alpha Omega SnR system. The recordings were electrically referenced to the posterior titanium headpost, which was anchored to the cranium with 10-15 titanium bone screws. LFP recordings were performed during (1) resting state conditions with the animal seated in a primate chair with its eyes open and minimal movement, and (2) during a voluntary reaching task to retrieve pieces of fruit from a Klüver board. During the former, four or five sessions (30-60 seconds each) were recorded per animal per MPTP condition. During the latter, joint position data was collected from reflective markers placed on the limbs using infrared motion capture cameras (Vicon, T-series) and webcams (Logitech). Limb positions were reconstructed in Vicon Nexus software and kinematic parameters were extracted in MATLAB. The motion capture cameras were synced to the recordings via a TTL pulse delivered at the beginning of recording session, and the video cameras were synced to the LFP recordings by a large motion artifact induced by tapping on the wires at the end of the trials. Subject N performed 99 and 86 reaches for naïve and parkinsonian conditions, respectively. Subject G performed 62 and 36 reaches for naïve and parkinsonian conditions, respectively.

4.2.7 MPTP Injections

Following measurements in the drug naïve condition, systemic MPTP injections were administered to each animal, after which the LFP recordings were repeated. MPTP is a neurotoxin that, when delivered systemically, causes degeneration of dopamine neurons in the substantia nigra pars compacta [229] as well as neurons within the pedunculopontine

nucleus [230] and centromedian nucleus [231], among other structures that are known to degenerate in Parkinson's disease. Subject G was given systemic injections over two consecutive days (0.7 mg/kg total). Subject N was given three rounds of systemic injections, first over three consecutive days (0.5 mg/kg total), next over two consecutive days (0.6 mg/kg total), and finally over another two consecutive days (0.6 mg/kg total). Through these systemic MPTP injections, both subjects were rendered to a stable, moderately severe parkinsonian state as assessed by a modified Unified Parkinson's Disease Rating Scale (mUPDRS) [209].

4.2.8 LFP Signal Processing and Spectral Analysis

The recorded monopolar LFP data were analyzed offline using custom MATLAB scripts (v2016b, Mathworks) and the Chronux toolbox [232]. In post-processing, the LFP recordings were re-referenced into bipolar recordings by subtracting adjacent signals by columns or by rows. If an adjacent electrode was deemed non-functional, the next available channel down the row was used for bipolar calculation, and this calculation was adopted for all recordings for that particular DBS array to maintain consistency.

For resting state recordings, the first two seconds of the data were cropped to removing electronic settling offsets. A 1 Hz high pass filter and 100 Hz low pass filter were implemented on the device to remove baseline drift and hardware noise. Power spectra of resting state LFPs (20-30 seconds in duration) were calculated using the multi-taper method (Chronux) using 5 tapers [232]. Multitaper spectrograms were produced similarly, but using one taper, one second moving window with 100 ms step size, resulting in a 2 Hz multi-tapered frequency resolution. After removal of non-functional electrodes, recording data were further visually inspected for all recording sessions. If clear movement artifacts occurred, LFP time series around the movement were removed from analyses. The overall power spectrum for a given resting-state test condition was calculated by averaging over spectrogram windows. Bands of interest were defined as theta band (3-8 Hz), alpha band (8-10Hz), beta band (10–30 Hz) and gamma band (30–90 Hz).

Once a band of interest (e.g., beta-band activity) was identified, a bandpass filter (3rd order Butterworth) at the corresponding frequency range was applied to the bipolar LFP data, and the average band power was calculated by averaging the power spectrum of the frequency band of interest in the frequency spectrum, and converted to dB. A contour map of average band power of interest across all recording trials were then generated across the entire DBS array and spatially smoothed using a Gaussian filter. These contour maps were compared against electrode site impedances (see Section 2.5) using Pearson's correlation ($p<0.05$) under naïve and parkinsonian conditions.

LFPs during the reach and retrieval task were aligned to the time of movement initiation and spectrograms for each trial were calculated. Multitaper spectrograms were calculated using three tapers, 200 ms moving window with 20 ms step size, resulting in a 5 Hz multi-tapered frequency resolution. The spectrograms were then averaged triggering to all movement onsets and the average spectrograms were calculated by averaging the individual spectrograms for 30-70 reaches in the time-frequency domain, and normalized to a z-score against a baseline period 1.5 to 1 second before the reach onset [233]. Outliers of the normalized z-score spectrograms were identified as instances when power in all frequencies exceed five standard deviations from the mean and were excluded.

Once a z-score spectrogram was obtained, the standard deviation $\sigma_{z-score}$ of the z-score spectrogram map across the entire DBS array was calculated:

$$\sigma_{z-score}(t,f) = \sqrt{\frac{\sum_{i=1}^{N}\left(Z_i(t,f)-\overline{Z(t,f)}\right)^2}{N-1}} \quad (1)$$

where N is the total number of bipolar electrodes, $Z_i(t,f)$ is the individual z-score spectrogram, and $\overline{Z(t,f)}$ is the average of all z-score spectrograms across electrodes.

The z-score spectrograms were also directly subtracted to produce a difference z-score spectrogram:

$$Z_{diff}(t,f) = Z_1(t,f) - Z_2(t,f) \quad (2)$$

and the standard deviation of the difference spectrogram was also calculated:

$$\sigma_{z_{diff}}(t,f) = \sqrt{\frac{\sum_{i=1}^{N}\left(z_{diff_i}(t,f) - \overline{z_{diff}(t,f)}\right)^2}{N-1}} \quad (3)$$

The individual bipolar z-score spectrograms were compared to the virtual macroelectrode z-score spectrograms using Equation 2, and a standard deviation of the resulting z-score spectrogram values were calculated using Equation 3. This produced either three $\sigma_{z_{diff}}$ corresponding to each virtual macroelectrode (**Fig**. **4.6C**), or one overall plot reflecting the entire DBS array (**Fig. 4.6D**). We defined statistical significance as ±5 z-scores away ($p<3x10^{-7}$).

4.3. Results

4.3.1 DBS Array Implant Locations and Orientations

The implant trajectories for each subject's DBS arrays were identified by co-registration of pre-operative 7T MRI and post-operative CT imaging. The STN-DBS array in each subject was implanted along a parasagittal trajectory such that the DBS lead body passed through the medial STN with electrode rows 1-5 in Subject N and rows 5-7 in Subject G having at least one electrode within the subthalamic nucleus (**Fig. 4.1**). The implant angles were 35° and 52.5° off the vertical axis in the sagittal plane in Subjects N and G, respectively. The GPe-GPi-DBS arrays were implanted along a pseudo-coronal trajectory with electrode rows 5-6 in GPe and rows 0-2 in GPi in Subject N and rows 3-7 in GPe and rows 0-2 in GPi in Subject G. The implant angles were 32°and 62.5° off the vertical axis in the coronal plane in Subjects N and G, respectively. Histological confirmation of the DBS array positions was performed for Subject G [79,101], but no histology was available for Subject N who remains active on other studies.

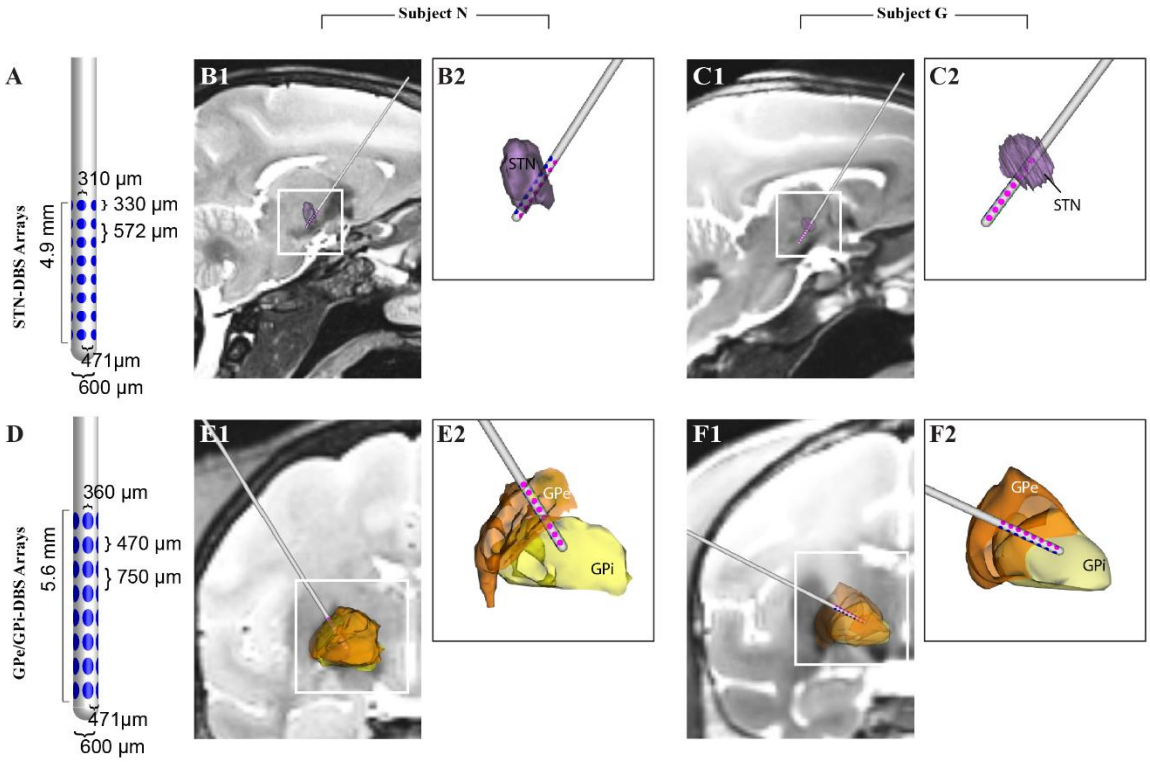

Figure 4.1: *DBS array implant locations. (**A, D**) DBS arrays consisting of 8 rows and 4 columns of macroelectrode sites were implanted in the STN (**B, C**) and GPe/GPi (**E, F**) in two rhesus macaques.*

While lead position was clearly visible using the co-registration process, DBS array orientation was determined by both visualization of the flexPCB cable with knowledge of how the cable was oriented with respect to the distal electrode columns. Additionally, biphasic stimulus pulse trains (300 Hz, 100-400 µA, 0.5 sec duration) were delivered through one or more electrodes along a single column of a DBS array to find stimulus thresholds at which muscle twitches first occurred. For all the DBS arrays, the contralateral hand first observed a twitch, followed by forearm and leg twitches upon ramping up stimulation amplitude. The stimulus threshold for the hand were found to be lower for electrode contacts facing internal capsule that for electrode contacts facing opposite to internal capsule for both STN-DBS and GPe/GPi-DBS arrays (**Fig. 4.2**). For the STN-DBS array in Subject G, evoked EMG potentials were measured in lieu of calculating a threshold

amplitude, and these potentials were found to be highest when stimulating through the lateral column of electrodes that were closest to internal capsule.

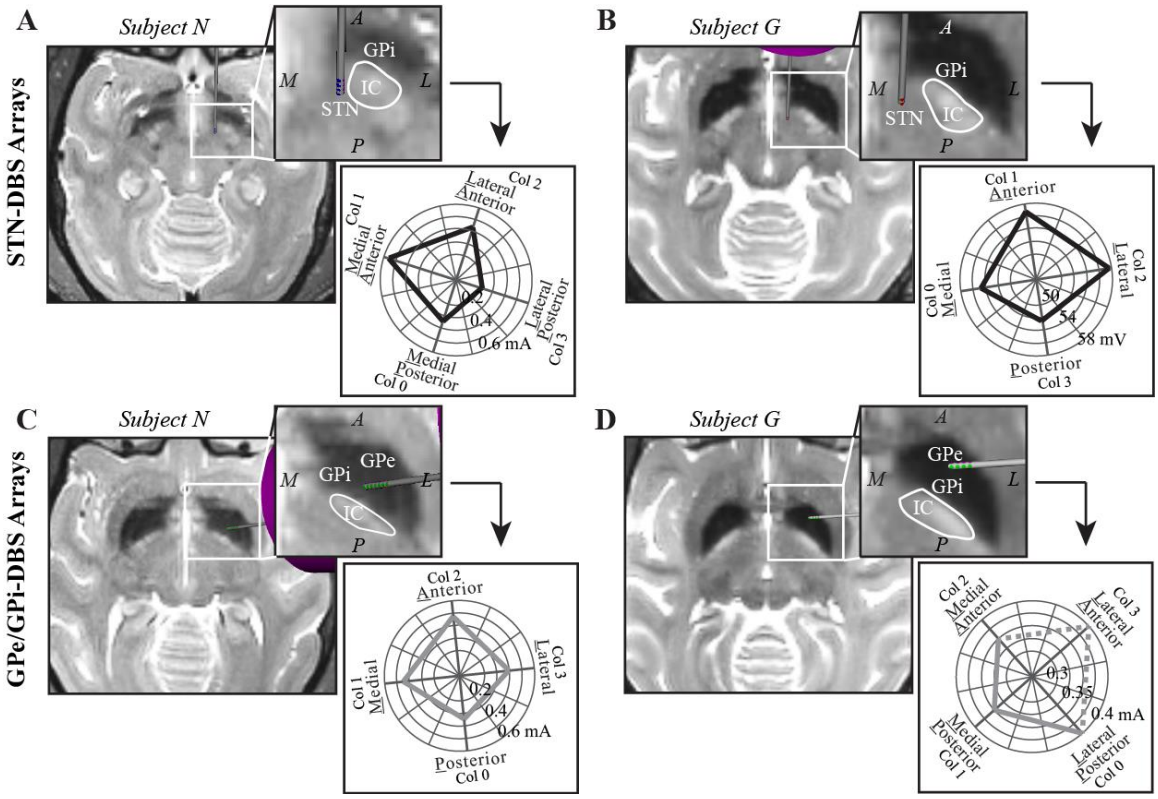

Figure 4.2: *Estimated orientation of the* ***(A, B)*** *STN-DBS arrays and* ***(C, D)*** *GPe/GPi-DBS arrays. DBS array implant locations and orientations are shown for each subject in the context of axial T2-weighted MR images and reconstructions of the internal capsule (IC). Also shown are polar plots for either current thresholds to evoke muscle twitches* ***(A, C-D)*** *or the resulting EMG peak voltages* ***(B)*** *when stimulating through electrodes along a single column. M-medial, L-lateral, P-posterior, A-anterior. Dashed lines in the polar plot indicate that a max current threshold could not be found to elicit a movement.*

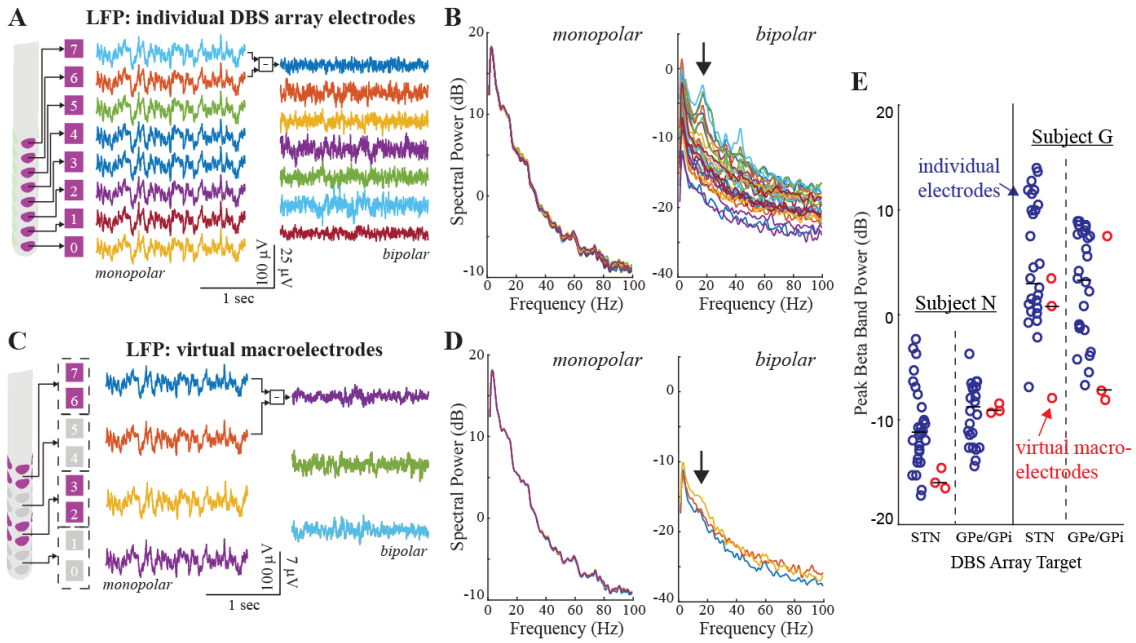

Figure 4.3: *Differences in peak beta band power amongst resting state LFP recording montages. Example monopolar and bipolar (row subtraction) recordings (**A**) and power spectra (**B**) from one column of DBS array electrodes in Subject N in the naïve condition. (**C, D**) Reanalysis of the same recordings using dual-row averaging to create virtual macroelectrodes with effective heights comparable to a primate scaled-down version of the 4-contact human DBS lead. (**E**) Summary comparison of peak beta band (10-20 Hz) power for all bipolar recordings (row subtraction) across DBS arrays using either individual electrode pairs or grouped virtual macroelectrode pairs.*

4.3.2 Resting State LFP Recordings through the DBS Arrays

Power spectra calculated from resting state LFP recordings exhibited much greater variability amongst bipolar than monopolar recording montages (**Fig. 4.3**). Bipolar recordings, which in this case involved calculating differences between monopolar recordings from two electrodes on adjacent rows, displayed greater variations in background spectral power as well as peak spectral power in the low beta band (~10-20 Hz) for both DBS arrays in the STN as well as DBS arrays in the GPe/GPi (**Fig. 4.3A-B**). Similar results were observed between monopolar and bipolar recording montages when

virtual macroelectrodes, defined by an averaging of two adjacent rows of electrode contacts, were used in the recording montage (**Fig. 4.3C-D**). As shown in the figure, in the naïve condition, the peak beta band power ranged for the STN-DBS arrays from -16 to -4 dB in Subject N and -8 to 9 dB in Subject G and for the GPe/GPi-DBS arrays from -18 to -1 dB in Subject N and -7 to 15 dB in Subject G, respectively. For all four DBS arrays, bipolar recording montages resulted in instances of higher peak beta band power than what was observed with bipolar recordings based on virtual cylindrical macroelectrodes. In Subject N, the latter exhibited similar peak beta band power amongst the three bipolar configurations for the STN-DBS array (-17 to -15 dB range) and the GPe/GPi-DBS array (-9 to -8 dB range). In Subject G, the range of peak beta band power for the three bipolar configurations was nearer to that observed for the individual electrode bipolar configurations (-8 to 4 dB range for the STN-DBS array and -9 to 8 dB range for the GPe/GPi-DBS array), but did not have as broad of spectral power as the bipolar montages with individual electrodes. Additionally, median peak beta band power was higher in Subject G (-12 dB, STN-DBS array and -8 dB, GPe/GPi-DBS array) than in Subject N (3 dB, STN-DBS array and 3 dB, GPe/GPi-DBS array).

4.3.3 Effects of Site Impedance on Bipolar LFP Power

Contour maps of average beta band power for both monopolar and bipolar configurations were constructed to investigate the extent to which spatial heterogeneity of beta power across the DBS arrays depended upon site impedances at comparable frequencies (**Fig. 4.4A-D**). For monopolar configurations, both subjects under the naïve and parkinsonian conditions had less than 25% correlation between their respective average beta power map and the site impedance map for all sessions (n = 4-5 daily sessions of 20 to 30-second resting state recordings per condition) (**Fig. 4.4E**). In addition, bipolar contour maps of beta power had minimal correlation with differential impedance maps ($r<0.25$) (**Fig. 4.4F**). None of the comparisons showed a statistically significant correlation coefficient by a Wilcoxon rank-sum test, therefore failing to reject the null hypothesis that the amplitude of average beta power in LFP were correlated with impedance.

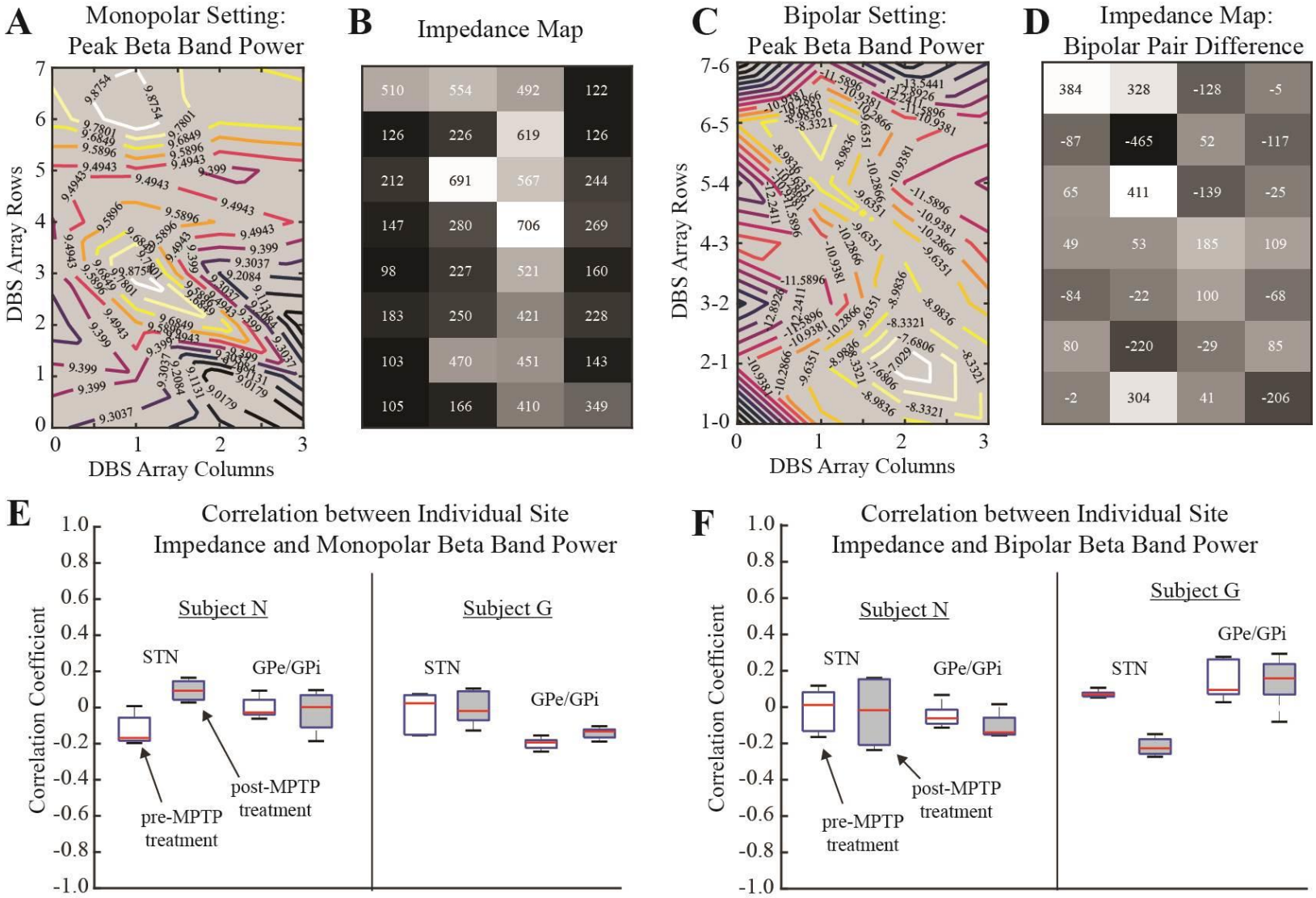
A
Monopolar Setting:
Peak Beta Band Power
DBS Array Rows
DBS Array Columns
B
Impedance Map
510 554 492 122
126 226 619 126
212 691 567 244
147 280 706 269
98 227 521 160
183 250 421 228
103 470 451 143
105 166 410 349
C
Bipolar Setting:
Peak Beta Band Power
DBS Array Rows
DBS Array Columns
D
Impedance Map:
Bipolar Pair Difference
384 328 -128 -5
-87 -465 52 -117
65 411 -139 -25
49 53 185 109
-84 -22 100 -68
80 -220 -29 85
-2 304 41 -206
E
Correlation between Individual Site
Impedance and Monopolar Beta Band Power
Correlation Coefficient
Subject N
Subject G
STN
GPe/GPi
pre-MPTP
treatment
post-MPTP
treatment
F
Correlation between Individual Site
Impedance and Bipolar Beta Band Power
Correlation Coefficient
Subject N
Subject G
STN
GPe/GPi
pre-MPTP
treatment
post-MPTP
treatment

Figure 4.4 *Effects of site impedance on spatial maps of beta band power. Example of an (**A**) monopolar and (**C**) bipolar contour map showing peak beta band power (in dB) and (**B, D**) their respective electrode site impedance maps at 20 Hz (in kΩ). Summary correlations for (**E**) monopolar and (**F**) bipolar electrode configurations based on row differences.*

4.3.4 'Fingerprints' of beta band activity in the STN and GPe/GPi

Across all DBS arrays in both naïve and parkinsonian conditions, beta band oscillations were observed in the 10-20 Hz range for bipolar recording montages. The spatial distribution of this beta band activity was compiled into contour maps (or 'fingerprints') for each DBS array and averaged over all recording sessions in a given condition (**Fig. 4.5**). In both naïve and parkinsonian conditions, the STN-DBS arrays in both subjects exhibited pronounced beta power distributed in columns. This spatial distribution was observed in column 2 (facing lateral-anterior) in Subject N with additional higher beta band power more dorsally in columns 0 and 3 (facing lateral-posterior and lateral-anterior) in the parkinsonian condition. The column-based distribution was also observed in more distal contacts Subject G, but shifted from column 1 (anterior facing) to column 2 (lateral facing) between naïve and parkinsonian conditions. Additionally, for the STN-DBS array in both Subjects N and G, there was an average of 6 dB power drop among all electrodes in beta oscillation power between the naïve and parkinsonian conditions. In the naïve condition in Subject N, the GPe/GPi-DBS array showed elevated beta power in the middle rows (effectively at the internal medullary lamina between GPe and GPi) and in columns 0 and 3, which faced posterior and lateral. In the parkinsonian condition, the spatial peak beta power increased and shifted dorsally to within GPe centered between columns 2 and 3, which faced anterior and lateral. In the naïve condition in Subject G, the GPe/GPi-DBS array spatial peak beta power was primarily located in the upper rows in column 2 (GPe, medial-anterior direction) and in the lower rows in columns 0 and 2 (GPi, lateral-posterior and medial-anterior). In the parkinsonian condition in Subject G, the contour map showed a similar pattern to the naïve condition except the overall average beta band power dropped

by ~10 dB and the stronger beta band power observed in the upper rows of column 2 was muted.

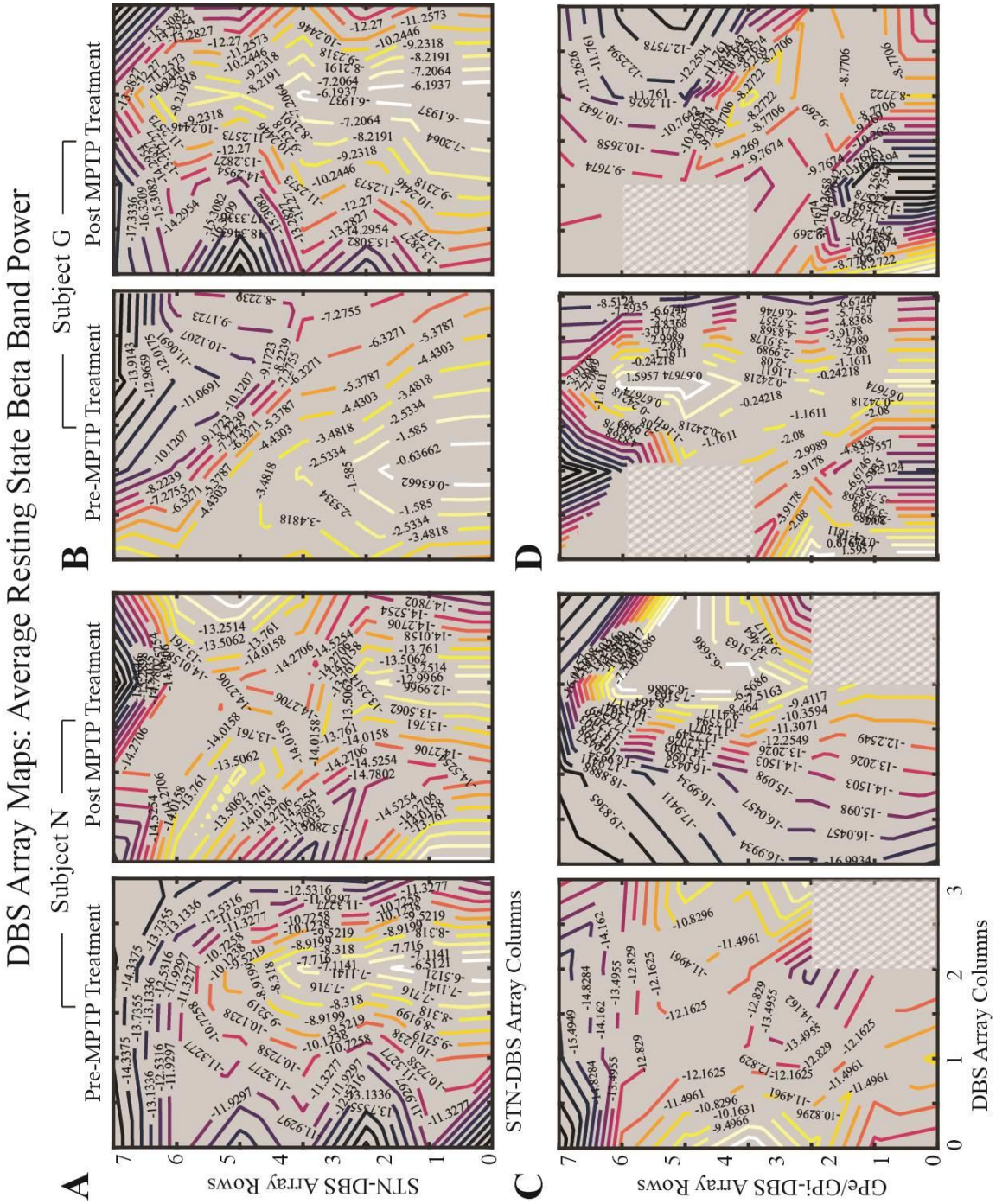

Figure 4.5: *Spatial 'fingerprints' of average resting state beta power amongst DBS arrays. Average bipolar beta band power contour maps for (**A-B**) STN-DBS arrays and (**C-D**) GPe/GPi-DBS arrays in Subjects N and G in the naïve and parkinsonian conditions. Cross-hatched locations on the contour map indicate locations where non-functional sites precluded calculation of bipolar recording montages. Contour line values are in dB.*

4.3.5 Spatial Resolution of Oscillatory Activity during Voluntary Reaching

Both subjects performed a reach and retrieval task in the naïve and parkinsonian states during which LFP recordings were collected on both DBS arrays. These recordings were processed in terms of individual electrodes (bipolar: adjacent row subtraction) or virtual macroelectrodes (bipolar: adjacent grouped row subtraction) (**Fig. 4.6A-B**). Spectrograms with z-score coloring showed significant decreases in beta band power immediately before and after the onset of the reach movement, but not necessarily consistently across all bipolar pairs. Additionally, there was pronounced low gamma band (30-50 Hz) activity immediately following the onset of the reach movement. An example comparison between spectrograms for individual bipolar electrodes and virtual bipolar macroelectrodes is shown in **Fig. 4.6A-B** for Subject G's GPe/GPi-DBS array in the parkinsonian state.

To investigate which time-frequency components of the spectrograms varied between individual and virtual macroelectrode bipolar pairs, the standard deviation of the differences between each of twelve individual bipolar spectrograms (**Fig. 4.6A**) and the complementary grouped bipolar spectrograms (**Fig. 4.6B**) for all combinations across the entire DBS array were calculated, and a single standard deviation map of the z-score differences was computed (**Fig. 4.6C**). The results of this single measure for all DBS arrays is summarized in **Fig. 4.6D**. In both Subject N and G's GPe/GPi-DBS array in the naïve condition, most of the variation between individual and grouped bipolar spectrograms was between 1-10 Hz and overlapped with, movement onset. In the parkinsonian state, an additional gamma band variation occurred immediately following reach onset in both subjects. For the STN-DBS arrays in the naïve condition, most of the variation between

individual and grouped bipolar spectrograms were localized in beta band (10-30 Hz) in both subjects, also overlapping with movement onset. Additionally, there was broadband variation following movement onset in Subject G in the naïve condition. In the parkinsonian condition in both subjects, individual and grouped bipolar spectrograms were more consistent in the beta band at movement onset, but also exhibited greater variation in 1-10 Hz band and gamma band (25-50 Hz).

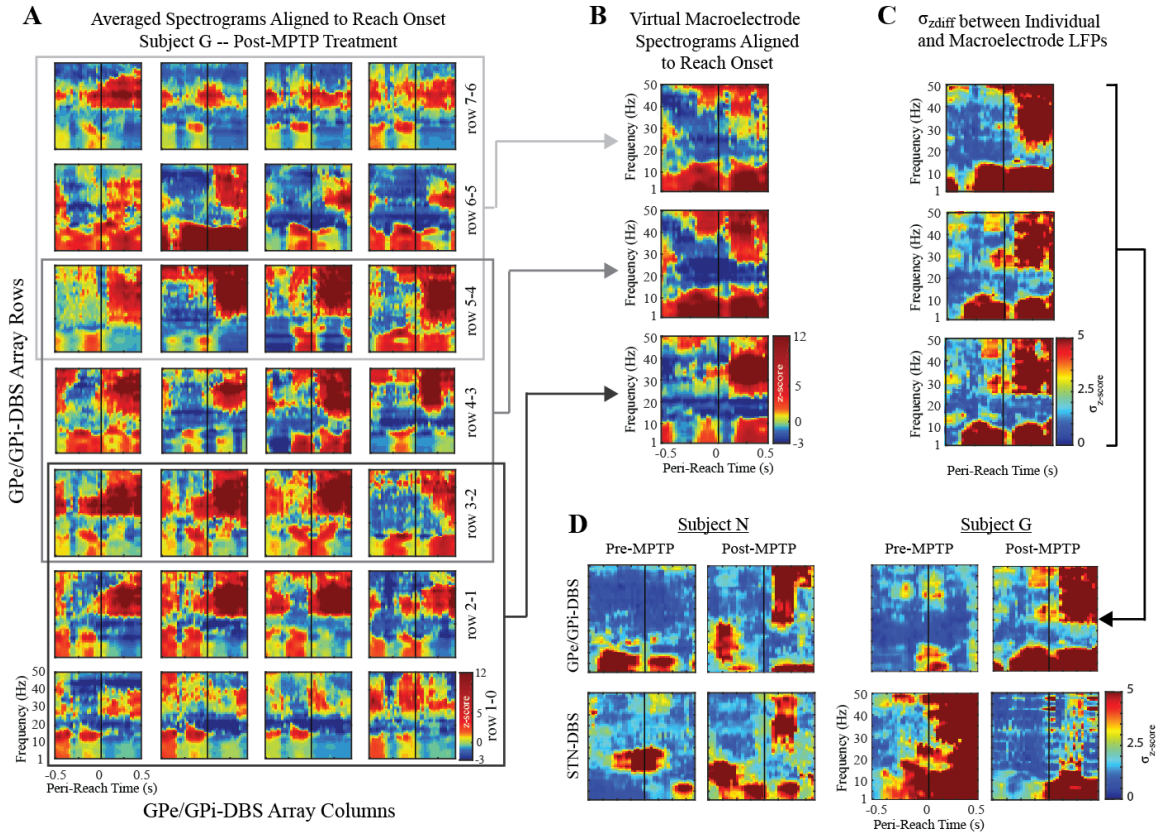

Figure 4.6: *Spectrogram analysis of DBS array LFP recordings in the context of a voluntary reach task. (**A**) An example of bipolar spectrograms recorded on a GPe/GPi-DBS array in Subject G in the parkinsonian condition. (**B**) The corresponding bipolar spectrograms based on the virtual macroelectrode montage. (**C**) Standard deviation map of the z-score difference between the individual DBS array electrode spectrograms and the corresponding virtual macroelectrode spectrograms. (**D**) Summary standard deviation*

maps of the z-score difference between individual and virtual macroelectrode spectrograms for all DBS arrays in both naïve and parkinsonian conditions.

4.3.6 Orientation of Bipolar LFP Signals in the STN and GPe/GPi

The DBS arrays provided an opportunity to investigate how referencing of the bipolar LFPs affected recordings in the resting state and during the voluntary reach task. Power spectra with prominent beta band spectral peaks were found for bipolar LFPs calculated horizontally across columns as well as vertically across rows of the DBS arrays (**Fig. 4.7**). In the resting state, there were no significant differences in average peak beta band power between row versus column referencing (**Fig. 4.7A-C**, Wilcoxin ranksum test). However, for any given recording and in a fraction of electrode pairs, low beta band activity could be detected more strongly in one referencing montage than in another. For instance, Subject N's GPe/GPi-DBS array in the naïve condition and resting state showed row bipolar configurations exhibiting the highest low beta band peaks, whereas the column bipolar low beta band peaks were not as prominent with stronger theta band activity.

Variation in spectral features of the LFP recordings between row versus column referencing was more notable in the context of the voluntary reaching tasks. Examples from two DBS arrays are shown in **Fig. 4.7D**. In this case, for the GPe/GPi-DBS array, the top row bipolar electrode configuration facing the medial direction exhibited significant low frequency desynchronization (1-10 Hz), which was not the case for the complementary column bipolar configurations between medial-anterior or medial-posterior facing electrodes. These differences are shown in a standard deviation map for a single row or column (**Fig. 4.7E**) indicating that most of the variation was in the low frequency band (1-10 Hz) immediately before and after the onset of movement. For the STN-DBS array electrodes shown in **Fig. 4.7D-E**, on the other hand, the strongest variation was found in the beta band coincident with the onset of movement for both rows and columns.

To investigate differences in spectrogram variation between row and column referencing, the standard deviation maps for adjacent rows and columns were subtracted from one another (**Fig. 4.7E**). A summary plot for all subjects across all DBS arrays and

conditions is shown in **Fig. 4.7F**. In Subject N's GPe/GPi-DBS array in both naïve and parkinsonian conditions, the column bipolar exhibited more variance in delta-beta bands (1-20 Hz) before the movement onset, while row bipolar exhibited more variance in delta-theta bands (1-8 Hz) after the movement onset. In Subject N's STN-DBS array, row bipolar exhibited more variance in delta-alpha bands (1-10 Hz) both before and after the movement onset, while column bipolar exhibited more variance in the beta band in the naïve condition. In Subject G in both DBS arrays, row bipolar contributed to beta-gamma band (20-40 Hz) variance in the parkinsonian condition, while column bipolar contributed more variance in delta-beta bands (1-20 Hz) and high gamma bands (40-50 Hz) in parkinsonian GPe/GPi and naïve STN.

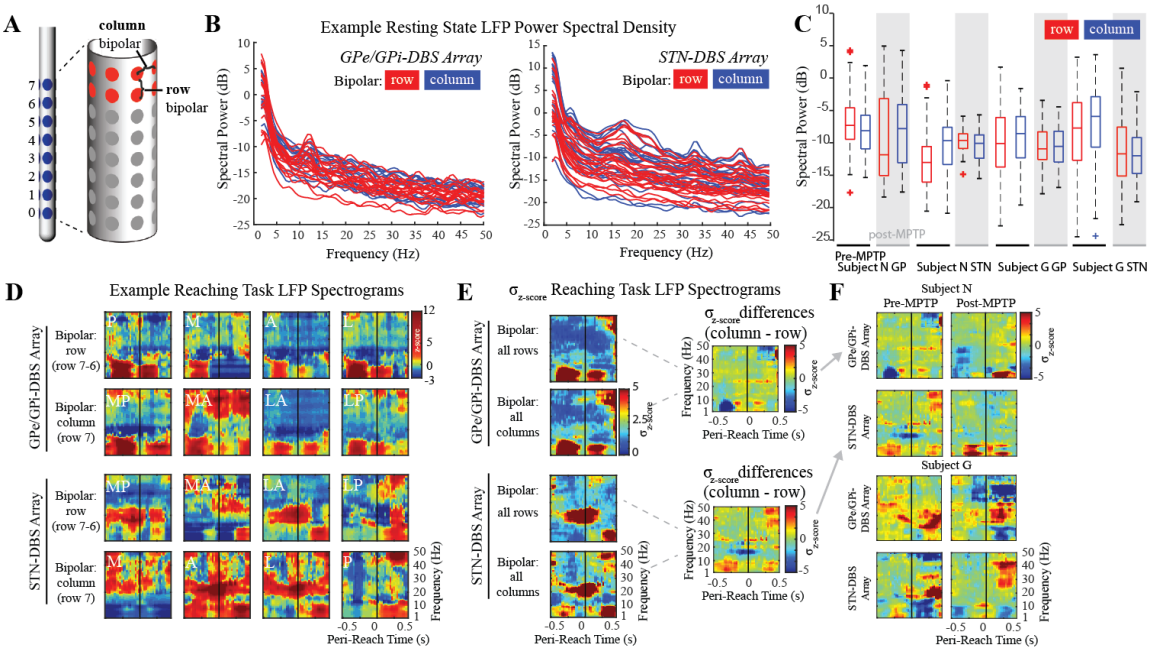

Figure 4.7: *Effects of bipolar electrode referencing on resting state and reaching task LFP recordings. (**A**) Montages including row and column subtraction. (**B**) Examples of resting state power spectra for row and column bipolar LFPs as shown for Subject N in the naïve condition. (**C**) In the resting state in each subject, peak beta band power did not differ between naïve and parkinsonian conditions. (**D**) Standard deviation maps of the z-score spectrograms across subsets of electrodes on the GPe/GPi-DBS array and the STN-DBS array as shown for Subject N in the naïve condition. (**E**) Resulting difference of z-score*

*standard deviation maps between row and column bipolar LFPs. (**F**) Summary of all differences in z-score standard deviation maps for both subjects, both DBS arrays, and naïve and parkinsonian conditions.*

4.4 Discussion

We demonstrated that LFP signals recorded with DBS arrays showed significant heterogeneity in the spatial distribution of oscillatory activity in the STN and GPe/GPi in naïve and parkinsonian non-human primates. The use of smaller segmented electrodes around and along the DBS array was shown to limit shunting of underlying oscillatory dipoles that occurred when grouping electrodes together to create virtual macroelectrode configurations that would be consistent with the large-scale cylindrical electrode LFP recordings available in commercially available DBS systems.

4.4.1 Electrode Dimensions and Underlying Anatomy

Standard DBS leads for human use contain cylindrical electrode contacts with 1.5 mm height and 2.0 to 3.5 mm center-to-center spacing between electrodes. Scaled-down versions of the DBS leads in preclinical non-human primate studies used previously consist of cylindrical electrodes with 0.5 mm height with 1.0 mm center-to-center electrode spacing [234]. In both human and non-human primate cases, the electrodes and the spacing between electrodes typically allows for only 2-3 cylindrical electrodes to be located within the target, such as the STN or GPi.

Anatomical projections from primary motor, premotor, and supplementary motor cortex are known to terminate in topographically distributed subregions within the sensorimotor STN. In the non-human primate, each subregion has dimensions less than 1 mm and a somatotopic arrangement along the long axis (dorsal-lateral to ventral-medial) of the nucleus [140,235]. Within the sensorimotor GPe and GPi, inputs from the sensorimotor striatum form a laminar structure parallel, and in some cases tangential, to

the internal medullary lamina with inter-lamina spacing ranging less than 1 mm in non-human primates [141]. Similar and convergent laminar structures have been observed in the GPe and GPi from axonal processes extending from the STN [236]. The organization of such axonal projections from the cortex into STN, GPe, and GPi suggests that synchronous input through these topographically arranged afferent processes should result in prominent oscillatory activity in the form of LFPs [68].

Two versions of a 32-contact DBS array were designed with one for targeting the STN and the other for targeting the GPe/GPi. The STN-DBS array consisted of electrode rows that spanned approximately 4 mm to allow for several rows of electrodes to be located within the STN and for several rows of electrodes to be located slightly dorsal and ventral to the STN. The GPe/GPi-DBS array consisted of electrode rows that spanned approximately 6 mm to enable LFP recordings from both the GPe and GPi. Segmentation of the electrode rows into four columns enabled sensing subregions within GPe and GPi within the same putative lamina.

4.4.2 DBSA Electrode and Macroelectrode Recordings

Basal ganglia field potentials have been recorded using wire microelectrodes [212,237,238], 250 µm diameter bipolar concentric electrodes [222], and clinical DBS leads with four cylindrical electrodes [239–243]. The different types of electrodes have various surface areas, and this could cause discrepancies between oscillatory activity seen in human and animal studies. The larger surface area in clinical DBS lead electrodes may short electric dipoles in the surrounding tissue and therefore under-detect salient oscillations that may be visible in microelectrodes [101]. Conversely, the volume of tissue contributing to an LFP from a microelectrode could be smaller than for a clinical electrode and under-detect an oscillation that can only be measured when recording from a large synchronous population of neurons.

In this study, the DBS arrays were designed to provide a balance in function between microelectrodes and clinical macroelectrodes. Segmenting the electrodes around the DBS lead perimeter also provided opportunities to sample from a singular radial

direction, offering more orientation resolution and allowing for more targeted sampling of heterogeneous tissue than traditional DBS electrodes, which summate over all radial directions around the DBS lead. We demonstrated that spectral information collected by virtual macroelectrodes (obtained by averaging two rows of recorded monopolar field potential signals to match the surface area of the scaled-down non-human primate version of clinical DBS electrodes [101]) showed smaller ranges in peak beta band power (**Fig. 4.3E**, Subject N and to some extent Subject G) and smaller maximum peak beta power across all electrodes (**Fig. 4.3E**, both subjects). Closed-loop DBS systems rely on the ability to record LFP signals faithfully from deep brain targets, and improving input signal power using DBS leads with smaller electrodes will no doubt help in the design of amplifiers for these systems. Additionally, these results indicate that virtual macroelectrode configurations not only short underlying dipole activity, but also that the strength of the dipole activity strongly depends on the electrode placement. For instance, for STN-DBS arrays in both subjects and GPe/GPi-DBS array in Subject N, the virtual macroelectrode beta power range was tighter than for the individual bipolar electrode configurations. The exception was the GPe/GPi-DBS array in Subject G, in which one virtual macroelectrode bipolar configuration reached the peak beta power level found in the individual electrode bipolar configurations. The virtual macroelectrode configurations also exhibited less variability in several frequency bands during the reach and retrieval tasks in comparison to bipolar electrode configurations with individual DBS array electrodes. This indicates that the conventional clinical DBS leads are not effectively capturing nuanced sub-regional activity within the STN and GPe/GPi that is engaged during task-based behaviors. This again has importance for future closed-loop DBS therapies that seek to adapt stimulation parameters during free-ranging behaviors in that DBS arrays with smaller electrode sites may be more capable of classifying behaviors in the context of disease pathophysiological processes.

4.4.3 LFP Recordings during Resting State and Voluntary Reaching Task Behaviors

Spontaneous LFPs within the sensorimotor basal ganglia are thought to represent informative information relevant to naïve versus parkinsonian conditions. Similar to a report from Bour and colleagues [214], we observed that the spatial distribution of beta band activity varied between individual rows and columns across the DBS arrays in both subjects, forming "fingerprint" maps. These maps showed stronger beta band activity along columns in the case of the STN-DBS arrays and within smaller isolated subregions for the GPe/GPi-DBS arrays. In the former case, the columns exhibiting the stronger beta band activity were directed towards the dorsolateral STN, which is consistent with higher beta activity reported in the sensorimotor territory of the STN [207,226,240,244]. Following the induction of a parkinsonian condition with MPTP treatment, the locations of the stronger beta band activity shifted slightly by one column in Subject G and extended to another column in Subject N suggesting that while beta activity is present in both naïve and parkinsonian conditions, the precise location of the strongest beta activity may differ further suggesting the internal network dynamics within the STN have changed.

Numerous animal studies in rats [212] and non-human primates have shown that LFP signals in the basal ganglia are modulated by voluntary movements [210,245,246]. There have also been studies in humans that have investigated these movement-related LFP oscillations in the context of Parkinson's disease motor signs and therapy [239–243], albeit limited to the operating room environment and to a limited number of patients. In our study, the non-human primate subjects performed a reach and retrieval task during which LFPs were recorded from both STN-DBS and GPe/GPi-DBS arrays. While in the resting state, both row and column bipolar contributed similar frequency information, during an active task row bipolar and column bipolar contributed different time-frequency information to the LFP measurements, reflecting the influence of the dipole locations in a structure on the heterogeneity of the LFP signals (**Fig. 4.7**).

4.4.4 Interpretation of LFP Oscillatory Activity

Impedance of electrodes typically increase days after implantation [247–249] due to the nervous system's foreign body reaction, which involves development of an encapsulation

layer around the implanted device [250–254]. After several weeks, impedances typically stabilize [247], but this stability can be perturbed with electrical stimulation [248,255]. In this study, all LFP recordings were performed before stimulation and after impedance following implantation had stabilized to avoid potential confounding factors of signal quality. However, signal quality of LFP recordings in relation to electrode impedance is less studied and not well understood. Kappenman and Luck [256] performed a study on the effect of EEG electrode impedance on signal quality and concluded that high impedance led to a poorer S/N ratio and produced an increase in the noise level in the lower frequencies (<4Hz) under warm and humid conditions, but this could be partially mitigated by high-pass filtering and artifact rejection. In our study, we only included electrodes with impedances less than 700 kΩ at 20 Hz because from visual inspection, electrodes with impedance higher than 700 kΩ showed visible broad-band noise across all frequencies, biasing the bipolar calculation. We correlated the resting state beta frequency power to the impedance in both the monopolar and bipolar case, and the resulting correlation was low and not significant, indicating that electrode impedance's effect on signal quality of LFP recordings were minimal as long as the electrodes were within a reasonable range. This suggests that the beta band power recorded in the bipolar LFP signals were likely reflections of intrinsic biological processes in the targets, instead of a result of impedance artifacts. To verify that the LFP signals were not affected by averaging in post-processing, we also recorded signals with hardware shorting of the electrodes. The results between the hardware and software shorting did not show any significant differences in frequency content or signal quality (data not shown).

4.5 Conclusion

We demonstrated that segmented DBS arrays with higher density and smaller contacts were able to measure nuanced spectral changes in LFP activity in the basal ganglia between resting state and during an active reaching task, as well as between naïve and parkinsonian conditions. These spectral changes exhibited a heterogeneity within the target nuclei that

could not be sensed using larger cylindrical electrode contacts. Future development of closed-loop DBS therapies that rely on sensing LFP activity will likely benefit from the use of smaller electrode sizes and interelectrode spacings that are more consistent with known anatomical subregions within target nuclei.

Chapter 5
Conclusions

Where the target for DBS therapy is relatively large and simple in morphology and when DBS lead placement is well positioned, segmented DBS arrays may not be necessary. However, current estimates are that 15-34% of DBS procedures are performed to revise DBS lead placement or remove the DBS system altogether [257], making DBS lead misplacement one of the most prevalent complications in DBS therapy. Additionally, most of the targets for treating PD have complex morphologies and contain several pathways that may elicit untoward side effects when stimulated. Thus, having the ability and choice to steer current through DBS leads with higher channel counts has promise to be widely adopted within the clinical community.

However, segmented DBS leads also pose tremendous burden on clinicians for programming with the increased number of electrodes and their three-dimensional geometries. This dissertation aimed to address this issue. This dissertation advanced the programming of high-density segmented DBS arrays by implementing a PSO algorithm (Chapter 2) and an updated version of the algorithm to handle multiple regions of interests and regions of avoidance (Chapter 3) using computational modeling and patient-specific imaging in the motor thalamus for treating ET (Chapter 2), and the STN and GPe/GPi for treating PD (Chapter 3). In addition, an *in vivo* validation of the performance of the PSO algorithm was conducted in the STN of a parkinsonian non-human primate (Chapter 3). This dissertation also systematically quantified the heterogeneity of LFP signals recorded with the DBS array in terms of spatial scale, bipolar orientation, and frequency content in both resting state and during reaching tasks across naïve and parkinsonian conditions (Chapter 4). These data provide a much richer understanding of how future closed-loop DBS systems for assisting with the programming process can leverage oscillatory signals within the STN and GPe/GPi.

5.1 Summary of Findings

In Chapter 2, the PSO algorithm solved the multi-objective programming problem using a swarm of individual particles representing electrode configurations and stimulation amplitudes. Using a finite element model of motor thalamic DBS, the PSO algorithm was shown to efficiently optimize a multi-objective function using an aggregate-based method that maximized predictions of axonal activation in an ROI (VPLo), minimized predictions of axonal activation in an ROA (VPLc), and minimized power consumption. The collection of the PSO solutions were arranged onto a Pareto front. ROI and ROA activation predictions were consistent across swarms (<1% median discrepancy in axon activation). In addition, the algorithm was able to accommodate for (1) lead displacement (1 mm) with relatively small ROI (≤9.2%) and ROA (≤1%) activation changes and irrespective of shift direction; (2) reduction in maximum per-electrode current (by 50% and 80%) with ROI activation decreasing by 5.6% and 16%, respectively; and (3) disabling electrodes (n=3 and 12) with ROI activation reduction by 1.8% and 14%, respectively. Additionally, comparison between PSO predictions and multi-compartment axon model simulations showed discrepancies of <1% between approaches.

In Chapter 3, a Pareto-dominance based PSO was developed to replace the aggregate-based method. This new PSO algorithm was made to handle multiple ROIs and ROAs, as the STN and GPe/GPi contain multiple cell types, pathways, and subregions with complex geometries. The results of the new PSO algorithm were arranged onto a multi-dimensional Pareto front. One of the settings obtained by the PSO algorithm was tested in the STN of a parkinsonian non-human primate. Specifically, the PSO-derived setting was compared against (1) grouped row configurations that mimicked the traditional monopolar review settings and (2) a control setting that either involved lowering the stimulus amplitude or randomizing the active electrodes from the PSO-derived stimulation setting. The PSO stimulation setting was able to show more reduction in rigidity compared to traditional monopolar review settings and the control settings. The PSO setting also exhibited comparable performance to monopolar review settings in reducing gait cycle times across a habitrail.

In Chapter 4, the sensing ability of the DBS array was explored. LFP signals were recorded from DBS arrays in the GPe/GPi and STN in both resting state and during a reach-and-retrieval task in two non-human primates in both naïve and parkinsonian conditions. It was demonstrated that segmented DBS arrays with higher density and smaller contacts were able to provide more nuanced spectral information within a target nucleus than could be sensed using grouped electrode configurations that mimicked the large cylindrical contacts on commercial DBS leads. The increased spatial resolution of sensing abilities could be used to aid the selection of PSO-based programming solutions, and could also be leveraged to provide multiple input streams for future implementations of closed-loop control in DBS systems.

5.2 Future Directions and Clinical Translation

5.2.1 DBS Array Programming: Spatial Parameters

In this dissertation, DBS array programming was approached from the perspective of optimizing spatial parameters, which includes the geometry of the targets, neurons, pathways, geometry of the DBS leads, electrodes, distribution of electrodes, and the current amplitude for each electrode. To improve the accuracy of programming based on these spatial parameters, several considerations should be taken into account when applying programming algorithms such as the PSO in the clinic:

(1) High-resolution imaging: The segmentation of the targets rely on clearly defined borders of the structure with high contrast and minimal distortion artifacts. Most DBS clinics use 3T or 1.5T imaging, making some of the smaller targets such as the STN difficult to visualize. High field MRI (7T+) can improve resolution of the images, and therefore result in more accurate segmentations of the targets.

(2) More accurate and efficient segmentation of targets: With high field imaging, the targets are usually segmented by hand. While automatic segmentation algorithms exist, modeling throughput improvements need to be made in order for them to work efficiently on a subject-specific basis and within the context of a clinical setting.

Additionally, other innovative techniques such as Virtual Reality (VR) or Augmented Reality (AR) could be incorporated in 3D, where structures could be reshaped and sculpted more accurately in space. The software program, Preclinical Cicerone [160], which was further developed through this dissertation, now has the framework to incorporate these functions.

(3) Improvements of pathway modeling: Orientation of a neuron has a large effect on neuronal activation caused by electric stimulation [172,173] and therefore affecting the MAFT factors that the PSO rely on to determine activation. Better DTI imaging and processing techniques could help isolate individual pathways more precisely through probabilistic or deterministic tractography. Unfortunately, DTI images acquired at 7T and higher field strengths show strong distortion artifacts due to field inhomogeneity. This could potentially be corrected with better distortion-correction algorithms. Further, additional pathways could be incorporated into the modeling framework. For example, surrounding the STN are the thalamic fasciculus and the superior cerebellar peduncle (putative ROIs), and the medial lemniscus and other sensory pathways of the corticospinal tract (putative ROAs).

(4) Refining and validation of computational models of DBS: accurate programming of DBS arrays also relies on accurate representations of the neuronal activation via computational models. Although certain aspects of these models have been validated, more studies need to be done to directly compare model predicted cellular responses to experimentally acquired measures of cellular responses during stimulation. Further refinements in computational models of DBS will likely enable models to have a greater impact on clinical programming and may largely replace the tediousness of the "monopolar review" process.

(5) Increasing the usability of the computational algorithms: Applying computational algorithms to DBS programming in a patient-specific manner becomes a major time-limiting step. While most of the steps require labor, several steps could be improved to increase the speed of the whole process. For example, the VR segmentation described in (2) could allow clinicians to define ROIs and ROAs in a more intuitive manner. Additionally, future computational algorithms should be capable of adapting based

upon real-time feedback of how the previous suggested stimulation setting actually worked in a given patient.

In addition, one has to consider not only programming of the spatial parameters described in this dissertation (which electrode to turn on at which amplitude), but also temporal parameters such as pulse waveform shape, pulse width, timing of pulses, bursting patterns, etc. that can have strong effects on clinical outcomes of DBS therapy. Several ongoing studies are being conducted on the optimization of the temporal parameters, including those employing closed-loop DBS in which neurophysiological and wearable sensor feedback provides one or more signals that can be used by a controller to adapt how and when stimulation is delivered to the brain.

5.2.2 DBS Sensing for Closed-loop Applications

The success of closed-loop DBS will likely depend on feedback signals that are stable and faithfully reflect the clinical or pathophysiological state of the patient. Most physiological signals to date have been heavily influenced by the site and behavioral contexts in which they are recorded [203,219,258]. The power in beta band oscillations, for instance, have been applied within closed-loop DBS experiments. While some data has shown that beta band power correlates with parkinsonian severity [222,223,259], other studies have found strong spontaneous beta oscillations in STN [219,260–262] and GP [260–263] in the naïve state or a lack of spontaneous beta oscillations in either target in the parkinsonian state. Similar mixed results have been reported with the use of MPTP in non-human primates [221,264,265].

Decreasing electrode size and adapting the orientation of the bipolar pair of electrodes with DBS arrays should help to spatially enhance and isolate salient biomarkers, provide improved spatial selectivity for triggering stimulation, and limit the confounds that may arise when summating oscillatory activity from multiple functional territories within the target nucleus (as would be the case for the macroelectrode contacts). Additionally, LFP signals could also be used to guide the selection process obtained by the PSO algorithm, as the PSO returns multiple points on the Pareto front as final solutions.

Incorporating electrophysiological signals could add additional information to complement the computational modeling and increase the predictive strength of the overall algorithm.

5.2.3 Translation to the Clinic

In this dissertation, all experiments were conducted in a pre-clinical non-human primate model of PD. To further evaluate the performance of the computational algorithms in this dissertation, the two iterations of the PSO approach could be tested in human clinical studies. Unfortunately, no high-density DBS arrays have gained FDA approval for investigational or clinical human use; however, as more segmented DBS arrays (such as the Abbott 6172 and Boston Scientific Vercise Cartesia, **Fig. 1.1**) are implanted into patients, the algorithm could be adapted to these DBS leads. The PSO approach is also built to leverage independent current-controlled stimulation across many channels, and to date only the Boston Scientific stimulator system incorporates this technological feature.

Lastly, the algorithms are poised to help test hypotheses about how targeting one neural pathway more selectively than others influences therapeutic outcomes on individual parkinsonian symptoms and the extent to which stimulus-induced side effects can be held at bay. Importantly, as discussed earlier, there may not be a single stimulation setting (or a single target) that could alleviate all PD motor signs at once. Motor signs such as tremor and rigidity are relatively easy to observe, therefore relatively easy for clinicians to test the performance of stimulation settings obtained by the PSO algorithm or similar algorithms. Other symptoms such as gait and balance dysfunction remain time consuming to test and often have prolonged wash-in periods. Improving our understanding of the neural elements involved in the therapeutic effects of DBS on individual motor signs will be important and help programming algorithms such as the PSO approaches described in this dissertation to gain traction in clinical settings.

References

[1] Tysnes O-B and Storstein A 2017 Epidemiology of Parkinson's disease *J. Neural Transm.* **124** 901–5

[2] Chaudhuri K R, Healy D G and Schapira A H 2006 Non-motor symptoms of Parkinson's disease: diagnosis and management *Lancet Neurol.* **5** 235–45

[3] George S and Brundin P 2017 Solving the conundrum of insoluble protein aggregates *Lancet Neurol.* **16** 258–9

[4] Kalia L V, Lang A E, Hazrati L-N, Fujioka S, Wszolek Z K, Dickson D W, Ross O A, Deerlin V M V, Trojanowski J Q, Hurtig H I, Alcalay R N, Marder K S, Clark L N, Gaig C, Tolosa E, Ruiz-Martínez J, Marti-Masso J F, Ferrer I, Munain A L de, Goldman S M, Schüle B, Langston J W, Aasly J O, Giordana M T, Bonifati V, Puschmann A, Canesi M, Pezzoli G, Paula A M D, Hasegawa K, Duyckaerts C, Brice A, Stoessl A J and Marras C 2015 Clinical Correlations With Lewy Body Pathology in LRRK2-Related Parkinson Disease *JAMA Neurol.* **72** 100–5

[5] Oertel W and Schulz J B 2016 Current and experimental treatments of Parkinson disease: A guide for neuroscientists *J. Neurochem.* **139** 325–37

[6] Krack P, Martinez-Fernandez R, del Alamo M and Obeso J A 2017 Current applications and limitations of surgical treatments for movement disorders *Mov. Disord.* **32** 36–52

[7] Laitinen L V, Bergenheim A T and Hariz M I 2009 Leksell's posteroventral pallidotomy in the treatment of Parkinson's disease *Collections* **112** 53–61

[8] Svennilson E, Torvik A, Lowe R and Leksell L 1960 TREATMENT OF PARKINSONISM BY STEREOTACTIC THERMOLESIONS IN THE PALLIDAL REGION. A clinical evaluation of 81 cases. *Acta Psychiatr. Scand.* **35** 358–77

[9] Nutt, M.D. J G 1990 Levodopa-induced dyskinesia Review, observations, and speculations *Neurology* **40** 340–340

[10] Benabid A L, Pollak P, Louveau A, Henry S and Rougemont J de 1987 Combined (Thalamotomy and Stimulation) Stereotactic Surgery of the VIM Thalamic Nucleus for Bilateral Parkinson Disease *Stereotact. Funct. Neurosurg.* **50** 344–6

[11] Benabid A L, Pollak P, Hoffmann D, Gervason C, Hommel M, Perret J E, de Rougemont J and Gao D M 1991 Long-term suppression of tremor by chronic stimulation of the ventral intermediate thalamic nucleus *The Lancet* **337** 403–6

[12] Bakay R A, Starr P A, Vitek J L and DeLong M R 1997 Posterior ventral pallidotomy: techniques and theoretical considerations *Clin. Neurosurg.* **44** 197–210

[13] Bergman H, Wichmann T and DeLong M R 1990 Reversal of experimental parkinsonism by lesions of the subthalamic nucleus *Science* **249** 1436–8

[14] Obeso J A, Olanow C W, Rodriguez-Oroz M C, Krack P, Kumar R and Lang A E 2001 Deep-Brain Stimulation of the Subthalamic Nucleus or the Pars Interna of the Globus Pallidus in Parkinson's Disease *N. Engl. J. Med.* **345** 956–63

[15] Deuschl G, Schade-Brittinger C, Krack P, Volkmann J, Schäfer H, Bötzel K, Daniels C, Deutschländer A, Dillmann U, Eisner W, Gruber D, Hamel W, Herzog J, Hilker R, Klebe S, Kloß M, Koy J, Krause M, Kupsch A, Lorenz D, Lorenzl S, Mehdorn H M, Moringlane J R, Oertel W, Pinsker M O, Reichmann H, Reuß A, Schneider G-H, Schnitzler A, Steude U, Sturm V, Timmermann L, Tronnier V, Trottenberg T, Wojtecki L, Wolf E, Poewe W and Voges J 2006 A Randomized Trial of Deep-Brain Stimulation for Parkinson's Disease *N. Engl. J. Med.* **355** 896–908

[16] Weaver F M, Follett K, Stern M, Hur K, Harris C, Marks W J, Rothlind J, Sagher O, Reda D, Moy C S, Pahwa R, Burchiel K, Hogarth P, Lai E C, Duda J E, Holloway K, Samii A, Horn S, Bronstein J, Stoner G, Heemskerk J, Huang G D and Group for the C 468 S 2009 Bilateral Deep Brain Stimulation vs Best Medical Therapy for Patients With Advanced Parkinson Disease: A Randomized Controlled Trial *JAMA* **301** 63–73

[17] Lyons K E and Pahwa R 2004 Deep brain stimulation and essential tremor *J. Clin. Neurophysiol. Off. Publ. Am. Electroencephalogr. Soc.* **21** 2–5

[18] Krauss J K, Yianni J, Loher T J and Aziz T Z 2004 Deep brain stimulation for dystonia *J. Clin. Neurophysiol. Off. Publ. Am. Electroencephalogr. Soc.* **21** 18–30

[19] de Koning P P, Figee M, Munckhof P van den, Schuurman P R and Denys D 2011 Current Status of Deep Brain Stimulation for Obsessive-Compulsive Disorder: A Clinical Review of Different Targets *Curr. Psychiatry Rep.* **13** 274–82

[20] Pereira E A, Green A L, Nandi D and Aziz T Z 2007 Deep brain stimulation: indications and evidence *Expert Rev. Med. Devices* **4** 591–603

[21] Vitek J L 2002 Mechanisms of deep brain stimulation: excitation or inhibition *Mov. Disord. Off. J. Mov. Disord. Soc.* **17 Suppl 3** S69-72

[22] Golestanirad L, Elahi B, Graham S J, Das S and Wald L L 2016 Efficacy and Safety of Pedunculopontine Nuclei (PPN) Deep Brain Stimulation in the Treatment of Gait Disorders: A Meta-Analysis of Clinical Studies *Can. J. Neurol. Sci.* **43** 120–6

[23] Hamani C, Lozano A M, Mazzone P A M, Moro E, Hutchison W, Silburn P A, Zrinzo L, Alam M, Goetz L, Pereira E, Rughani A, Thevathasan W, Aziz T, Bloem B R, Brown P, Chabardes S, Coyne T, Foote K, Garcia-Rill E, Hirsch E C, Okun M S and Krauss J K 2016 Pedunculopontine Nucleus Region Deep Brain Stimulation in Parkinson Disease: Surgical Techniques, Side Effects, and Postoperative Imaging *Stereotact. Funct. Neurosurg.* **94** 307–19

[24] Yousif N, Bhatt H, Bain P G, Nandi D and Seemungal B M 2016 The effect of pedunculopontine nucleus deep brain stimulation on postural sway and vestibular perception *Eur. J. Neurol.* **23** 668–70

[25] Weiss D, Wächter T, Meisner C, Fritz M, Gharabaghi A, Plewnia C, Breit S and Krüger R 2011 Combined STN/SNr-DBS for the treatment of refractory gait disturbances in Parkinson's disease: study protocol for a randomized controlled trial *Trials* **12** 222

[26] Weiss D, Walach M, Meisner C, Fritz M, Scholten M, Breit S, Plewnia C, Bender B, Gharabaghi A, Wächter T and Krüger R 2013 Nigral stimulation for resistant axial motor impairment in Parkinson's disease? A randomized controlled trial *Brain* **136** 2098–108

[27] Contarino M F, Bour L J, Verhagen R, Lourens M A J, Bie R M A de, Munckhof P van den and Schuurman P R 2014 Directional steering A novel approach to deep brain stimulation *Neurology* **83** 1163–9

[28] Hoover J E and Strick P L 1993 Multiple output channels in the basal ganglia *Science* **259** 819–21

[29] Inase M, Tokuno H, Nambu A, Akazawa T and Takada M 1999 Corticostriatal and corticosubthalamic input zones from the presupplementary motor area in the macaque monkey: comparison with the input zones from the supplementary motor area *Brain Res.* **833** 191–201

[30] Nambu A, Takada M, Inase M and Tokuno H 1996 Dual somatotopical representations in the primate subthalamic nucleus: evidence for ordered but reversed body-map transformations from the primary motor cortex and the supplementary motor area *J. Neurosci.* **16** 2671–83

[31] Parent A and Hazrati L N 1995 Functional anatomy of the basal ganglia. II. The place of subthalamic nucleus and external pallidum in basal ganglia circuitry *Brain Res. Brain Res. Rev.* **20** 128–54

[32] Bevan M D, Magill P J, Terman D, Bolam J P and Wilson C J 2002 Move to the rhythm: oscillations in the subthalamic nucleus-external globus pallidus network *Trends Neurosci.* **25** 525–31

[33] Brown P, Oliviero A, Mazzone P, Insola A, Tonali P and Di Lazzaro V 2001 Dopamine dependency of oscillations between subthalamic nucleus and pallidum in Parkinson's disease *J. Neurosci. Off. J. Soc. Neurosci.* **21** 1033–8

[34] Foffani G, Priori A, Egidi M, Rampini P, Tamma F, Caputo E, Moxon K A, Cerutti S and Barbieri S 2003 300-Hz subthalamic oscillations in Parkinson's disease *Brain J. Neurol.* **126** 2153–63

[35] Levy R, Ashby P, Hutchison W D, Lang A E, Lozano A M and Dostrovsky J O 2002 Dependence of subthalamic nucleus oscillations on movement and dopamine in Parkinson's disease *Brain J. Neurol.* **125** 1196–209

[36] Mallet N, Pogosyan A, Márton L F, Bolam J P, Brown P and Magill P J 2008 Parkinsonian beta oscillations in the external globus pallidus and their relationship with subthalamic nucleus activity *J. Neurosci. Off. J. Soc. Neurosci.* **28** 14245–58

[37] Moran A, Bergman H, Israel Z and Bar-Gad I 2008 Subthalamic nucleus functional organization revealed by parkinsonian neuronal oscillations and synchrony *Brain* **131** 3395–409

[38] Plenz D and Kital S T 1999 A basal ganglia pacemaker formed by the subthalamic nucleus and external globus pallidus *Nature* **400** 677–82

[39] Shimamoto S A, Ryapolova-Webb E S, Ostrem J L, Galifianakis N B, Miller K J and Starr P A 2013 Subthalamic nucleus neurons are synchronized to primary motor cortex local field potentials in Parkinson's disease *J. Neurosci. Off. J. Soc. Neurosci.* **33** 7220–33

[40] Halpern C H, Danish S F, Baltuch G H and Jaggi J L 2008 Brain Shift during Deep Brain Stimulation Surgery for Parkinson's Disease *Stereotact. Funct. Neurosurg.* **86** 37–43

[41] Khan M F, Mewes K, Gross R E and Škrinjar O 2008 Assessment of Brain Shift Related to Deep Brain Stimulation Surgery *Stereotact. Funct. Neurosurg.* **86** 44–53

[42] Miyagi Y, Shima F and Sasaki T 2007 Brain shift: an error factor during implantation of deep brain stimulation electrodes *Collections* **117** 989–97

[43] Hunka K, Suchowersky O, Wood S, Derwent L and Kiss Z H T 2005 Nursing time to program and assess deep brain stimulators in movement disorder patients *J. Neurosci. Nurs. J. Am. Assoc. Neurosci. Nurses* **37** 204–10

[44] Cooper S E, Driesslein K G, Noecker A M, McIntyre C C, Machado A M and Butson C R 2014 Anatomical targets associated with abrupt versus gradual washout of subthalamic deep brain stimulation effects on bradykinesia *PloS One* **9** e99663

[45] Cooper S E, Noecker A M, Abboud H, Vitek J L and McIntyre C C 2011 Return of bradykinesia after subthalamic stimulation ceases: Relationship to electrode location *Exp. Neurol.* **231** 207–13

[46] Lopiano L, Torre E, Benedetti F, Bergamasco B, Perozzo P, Pollo A, Rizzone M, Tavella A and Lanotte M 2003 Temporal changes in movement time during the switch of the stimulators in Parkinson's disease patients treated by subthalamic nucleus stimulation *Eur. Neurol.* **50** 94–9

[47] Firszt J B, Koch D B, Downing M and Litvak L 2007 Current steering creates additional pitch percepts in adult cochlear implant recipients *Otol. Neurotol. Off. Publ. Am. Otol. Soc. Am. Neurotol. Soc. Eur. Acad. Otol. Neurotol.* **28** 629–36

[48] Steigerwald F, Müller L, Johannes S, Matthies C and Volkmann J 2016 Directional deep brain stimulation of the subthalamic nucleus: A pilot study using a novel neurostimulation device *Mov. Disord.* **31** 1240–3

[49] Connolly A T, Jensen A L, Bello E M, Netoff T I, Baker K B, Johnson M D and Vitek J L 2015 Modulations in oscillatory frequency and coupling in globus pallidus with increasing parkinsonian severity *J. Neurosci. Off. J. Soc. Neurosci.* **35** 6231–40

[50] Teplitzky B A, Zitella L M, Xiao Y and Johnson M D 2016 Model-Based Comparison of Deep Brain Stimulation Array Functionality with Varying Number of Radial Electrodes and Machine Learning Feature Sets *Front. Comput. Neurosci.* **10**

[51] Connolly A T, Vetter R J, Hetke J F, Teplitzky B A, Kipke D R, Pellinen D S, Anderson D J, Baker K B, Vitek J L and Johnson M D 2016 A Novel Lead Design for Modulation and Sensing of Deep Brain Structures *IEEE Trans. Biomed. Eng.* **63** 148–57

[52] Warman E N, Grill W M and Durand D 1992 Modeling the effects of electric fields on nerve fibers: determination of excitation thresholds *IEEE Trans. Biomed. Eng.* **39** 1244–54

[53] McIntyre C C, Grill W M, Sherman D L and Thakor N V 2004 Cellular Effects of Deep Brain Stimulation: Model-Based Analysis of Activation and Inhibition *J. Neurophysiol.* **91** 1457–69

[54] Butson C R, Cooper S E, Henderson J M, Wolgamuth B and McIntyre C C 2011 Probabilistic analysis of activation volumes generated during deep brain stimulation *NeuroImage* **54** 2096–104

[55] Chaturvedi A, Butson C R, Lempka S F, Cooper S E and McIntyre C C 2010 Patient-specific models of deep brain stimulation: influence of field model complexity on neural activation predictions *Brain Stimulat.* **3** 65–7

[56] Lujan J L, Chaturvedi A, Malone D A, Rezai A R, Machado A G and McIntyre C C 2012 Axonal pathways linked to therapeutic and nontherapeutic outcomes during psychiatric deep brain stimulation *Hum. Brain Mapp.* **33** 958–68

[57] Riva-Posse P, Choi K S, Holtzheimer P E, McIntyre C C, Gross R E, Chaturvedi A, Crowell A L, Garlow S J, Rajendra J K and Mayberg H S 2014 Defining Critical White Matter Pathways Mediating Successful Subcallosal Cingulate Deep Brain Stimulation for Treatment-Resistant Depression *Biol. Psychiatry* **76** 963–9

[58] Xiao Y, Pena E and Johnson M D 2016 Theoretical Optimization of Stimulation Strategies for a Directionally Segmented Deep Brain Stimulation Electrode Array *IEEE Trans. Biomed. Eng.* **63** 359–71

[59] Chaturvedi A, Luján J L and McIntyre C C 2013 Artificial neural network based characterization of the volume of tissue activated during deep brain stimulation *J. Neural Eng.* **10** 056023

[60] McIntyre C C and Grill W M 2002 Extracellular Stimulation of Central Neurons: Influence of Stimulus Waveform and Frequency on Neuronal Output *J. Neurophysiol.* **88** 1592–604

[61] Rattay F 1986 Analysis of Models for External Stimulation of Axons *IEEE Trans. Biomed. Eng.* **BME-33** 974–7

[62] Xiao Y, Peña E and Johnson M D 2016 Theoretical Optimization of Stimulation Strategies for a Directionally Segmented Deep Brain Stimulation Electrode Array *IEEE Trans. Biomed. Eng.* **63** 359–71

[63] Leopold D A, Murayama Y and Logothetis N K 2003 Very Slow Activity Fluctuations in Monkey Visual Cortex: Implications for Functional Brain Imaging *Cereb. Cortex* **13** 422–33

[64] Kajikawa Y and Schroeder C E 2011 How Local Is the Local Field Potential? *Neuron* **72** 847–58

[65] Logothetis N K 2002 The neural basis of the blood–oxygen–level–dependent functional magnetic resonance imaging signal *Philos. Trans. R. Soc. Lond. B Biol. Sci.* **357** 1003–37

[66] Belitski A, Panzeri S, Magri C, Logothetis N K and Kayser C 2010 Sensory information in local field potentials and spikes from visual and auditory cortices: time scales and frequency bands *J. Comput. Neurosci.* **29** 533–45

[67] Okun M, Naim A and Lampl I 2010 The Subthreshold Relation between Cortical Local Field Potential and Neuronal Firing Unveiled by Intracellular Recordings in Awake Rats *J. Neurosci.* **30** 4440–8

[68] Buzsáki G, Anastassiou C A and Koch C 2012 The origin of extracellular fields and currents — EEG, ECoG, LFP and spikes *Nat. Rev. Neurosci.* **13** 407–20

[69] Mitzdorf U 1985 Current source-density method and application in cat cerebral cortex: investigation of evoked potentials and EEG phenomena *Physiol. Rev.* **65** 37–100

[70] Pesaran B 2009 Uncovering the Mysterious Origins of Local Field Potentials *Neuron* **61** 1–2

[71] Lempka S F and McIntyre C C 2013 Theoretical Analysis of the Local Field Potential in Deep Brain Stimulation Applications *PLOS ONE* **8** e59839

[72] Zhuang J, Truccolo W, Vargas-Irwin C and Donoghue J P 2010 Decoding 3-D reach and grasp kinematics from high-frequency local field potentials in primate primary motor cortex *IEEE Trans. Biomed. Eng.* **57** 1774–84

[73] Mehring C, Rickert J, Vaadia E, de Oliveira S C, Aertsen A and Rotter S 2003 Inference of hand movements from local field potentials in monkey motor cortex *Nat. Neurosci.* **6** 1253–4

[74] Asher I, Stark E, Abeles M and Prut Y 2007 Comparison of Direction and Object Selectivity of Local Field Potentials and Single Units in Macaque Posterior Parietal Cortex During Prehension *J. Neurophysiol.* **97** 3684–95

[75] Wichmann T and Delong M 2006 Deep Brain Stimulation for Neurologic and Neuropsychiatric Disorders *Neuron* **52** 197–204

[76] Contarino M F, Bour L J, Verhagen R, Lourens M A, de Bie R M, van den Munckhof P and Schuurman P R 2014 Directional steering: A novel approach to deep brain stimulation *Neurology* **83** 1163–9

[77] Martens H C, Toader E, Decre M M, Anderson D J, Vetter R, Kipke D R, Baker K B, Johnson M D and Vitek J L 2011 Spatial steering of deep brain stimulation volumes using a novel lead design *Clin Neurophysiol* **122** 558–66

[78] Pollo C, Kaelin-Lang A, Oertel M F, Stieglitz L, Taub E, Fuhr P, Lozano A M, Raabe A and Schupbach M 2014 Directional deep brain stimulation: an intraoperative double-blind pilot study *Brain* **137** 2015–26

[79] Connolly A T, Jensen A L, Baker K B, Vitek J L and Johnson M D 2015 Classification of pallidal oscillations with increasing parkinsonian severity *J. Neurophysiol.* **114** 209–18

[80] Keane M, Deyo S, Abosch A, Bajwa J A and Johnson M D 2012 Improved spatial targeting with directionally segmented deep brain stimulation leads for treating essential tremor *J. Neural Eng.* **9** 046005

[81] Dijk K J van, Verhagen R, Chaturvedi A, McIntyre C C, Bour L J, Heida C and Veltink P H 2015 A novel lead design enables selective deep brain stimulation of neural populations in the subthalamic region *J. Neural Eng.* **12** 046003

[82] Zitella L M, Mohsenian K, Pahwa M, Gloeckner C and Johnson M D 2013 Computational modeling of pedunculopontine nucleus deep brain stimulation *J Neural Eng* **10** 045005

[83] Hunka K, Suchowersky O, Wood S, Derwent L and Kiss Z H T 2005 Nursing time to program and assess deep brain stimulators in movement disorder patients *J. Neurosci. Nurs. J. Am. Assoc. Neurosci. Nurses* **37** 204–10

[84] Butson C R, Cooper S E, Henderson J M, Wolgamuth B and McIntyre C C 2011 Probabilistic analysis of activation volumes generated during deep brain stimulation *Neuroimage* **54** 2096–104

[85] Chaturvedi A, Butson C R, Lempka S F, Cooper S E and McIntyre C C 2010 Patient-specific models of deep brain stimulation: Influence of field model complexity on neural activation predictions *Brain Stimulat.* **3** 65–77

[86] Lujan J L, Chaturvedi A, Malone D A, Rezai A R, Machado A G and McIntyre C C 2012 Axonal pathways linked to therapeutic and nontherapeutic outcomes during psychiatric deep brain stimulation *Hum. Brain Mapp.* **33** 958–68

[87] Riva-Posse P, Choi K S, Holtzheimer P E, McIntyre C C, Gross R E, Chaturvedi A, Crowell A L, Garlow S J, Rajendra J K and Mayberg H S 2014 Defining Critical White Matter Pathways Mediating Successful Subcallosal Cingulate Deep Brain Stimulation for Treatment-Resistant Depression *Biol. Psychiatry* **76** 963–9

[88] Chaturvedi A, Luján J L and McIntyre C C 2013 Artificial neural network based characterization of the volume of tissue activated during deep brain stimulation *J. Neural Eng.* **10** 056023

[89] McIntyre C C and Grill W M 2002 Extracellular stimulation of central neurons: influence of stimulus waveform and frequency on neuronal output *J. Neurophysiol.* **88** 1592–604

[90] Wei X F and Grill W M 2005 Current density distributions, field distributions and impedance analysis of segmented deep brain stimulation electrodes *J. Neural Eng.* **2** 139–47

[91] Butson C R and McIntyre C C 2008 Current steering to control the volume of tissue activated during deep brain stimulation *Brain Stimul* **1** 7–15

[92] Rattay F 1986 Analysis of models for external stimulation of axons *IEEE Trans. Biomed. Eng.* **33** 974–7

[93] Peterson E, Izad O and Tyler D 2011 Predicting myelinated axon activation using spatial characteristics of the extracellular field *J. Neural Eng.* **8** 046030

[94] Brill N and Tyler D 2011 Optimizing nerve cuff stimulation of targeted regions through use of genetic algorithms *Conf. Proc. Annu. Int. Conf. IEEE Eng. Med. Biol. Soc. IEEE Eng. Med. Biol. Soc. Annu. Conf.* **2011** 5811–4

[95] Parsopoulos K E and Vrahatis M N 2002 Recent approaches to global optimization problems through Particle Swarm Optimization *Nat. Comput.* **1** 235–306

[96] Huang K-W, Yang C-S and Tsai C-W 2012 A Two-Phase Hybrid Particle Swarm Optimization Algorithm for Solving Permutation Flow-Shop Scheduling Problem *Int. J. Comput. Appl.* **48** 11–8

[97] Slade W 2004 Computational Intelligence Approaches to Ocean Color Inversion *Electron. Theses Diss.*

[98] Santos S M, Valença M J S and Bastos-Filho C J A 2012 Comparing Particle Swarm Optimization Approaches for Training Multi-Layer Perceptron Neural Networks for Forecasting *Intelligent Data Engineering and Automated Learning - IDEAL 2012* Lecture Notes in Computer Science ed H Yin, J A F Costa and G Barreto (Springer Berlin Heidelberg) pp 344–51

[99] Wu D, Warwick K, Ma Z, Gasson M N, Burgess J G, Pan S and Aziz T Z 2010 Prediction of Parkinson's disease tremor onset using a radial basis function neural network based on particle swarm optimization *Int. J. Neural Syst.* **20** 109–16

[100] Saini S, Zakaria N, Rambli D R A and Sulaiman S 2015 Markerless Human Motion Tracking Using Hierarchical Multi-Swarm Cooperative Particle Swarm Optimization *PLoS ONE* **10** e0127833

[101] Connolly A T, Vetter R J, Hetke J F, Teplitzky B A, Kipke D R, Pellinen D S, Anderson D J, Baker K B, Vitek J L and Johnson M D 2016 A Novel Lead Design for Modulation and Sensing of Deep Brain Structures *IEEE Trans. Biomed. Eng.* **63** 148–57

[102] Yousif N and Liu X 2009 Investigating the depth electrode–brain interface in deep brain stimulation using finite element models with graded complexity in structure and solution *J. Neurosci. Methods* **184** 142–51

[103] Miocinovic S, Lempka S F, Russo G S, Maks C B, Butson C R, Sakaie K E, Vitek J L and McIntyre C C 2009 Experimental and theoretical characterization of the voltage distribution generated by deep brain stimulation *Exp Neurol* **216** 166–76

[104] Schmidt C and van Rienen U 2012 Modeling the field distribution in deep brain stimulation: the influence of anisotropy of brain tissue *IEEE Trans. Biomed. Eng.* **59** 1583–92

[105] Howell B and McIntyre C C 2016 Analyzing the tradeoff between electrical complexity and accuracy in patient-specific computational models of deep brain stimulation *J. Neural Eng.* **13** 36023–39

[106] Grill W M and Mortimer J T Electrical properties of implant encapsulation tissue *Ann. Biomed. Eng.* **22** 23–33

[107] Ranck J B 1963 Specific impedance of rabbit cerebral cortex *Exp. Neurol.* **7** 144–52

[108] Teplitzky B A, Zitella L M, Xiao Y and Johnson M D 2016 Model-Based Comparison of Deep Brain Stimulation Array Functionality with Varying Number of Radial Electrodes and Machine Learning Feature Sets *Front. Comput. Neurosci.* **10** 58

[109] Kuncel A M, Cooper S E, Wolgamuth B R, Clyde M A, Snyder S A, Montgomery E B, Rezai A R and Grill W M 2006 Clinical response to varying the stimulus parameters in deep brain stimulation for essential tremor *Mov. Disord.* **21** 1920–8

[110] Xiao Y, Zitella L M, Duchin Y, Teplitzky B A, Kastl D, Adriany G, Yacoub E, Harel N and Johnson M D 2016 Multimodal 7T Imaging of Thalamic Nuclei for Preclinical Deep Brain Stimulation Applications *Brain Imaging Methods* 264

[111] Crouch R L 1934 The nuclear configuration of the hypothalamus and the subthalamus of Macacus rhesus *J. Comp. Neurol.* **59** 431–49

[112] Rattay F 1989 Analysis of models for extracellular fiber stimulation *IEEE Trans. Biomed. Eng.* **36** 676–82

[113] Plonsey R 1969 *Bioelectric Phenomena* (New York u.a.: McGraw-Hill Inc.,US)

[114] SASMOR L and SMITH E D 1988 Chapter 17 - Artificial Intelligence in Medicine A2 - KLINE, JACOB *Handbook of Biomedical Engineering* (Academic Press) pp 417–37

[115] Teplitzky B A, Connolly A T, Bajwa J A and Johnson M D 2014 Computational modeling of an endovascular approach to deep brain stimulation *J. Neural Eng.* **11** 026011

[116] Lempka S F, Johnson M D, Miocinovic S, Vitek J L and McIntyre C C 2010 Current-controlled deep brain stimulation reduces in vivo voltage fluctuations observed during voltage-controlled stimulation *Clin. Neurophysiol. Off. J. Int. Fed. Clin. Neurophysiol.* **121** 2128–33

[117] Kennedy J and Eberhart R 1995 Particle swarm optimization vol 4 (IEEE) pp 1942–8

[118] Shi Y and Eberhart R 1998 A modified particle swarm optimizer , *The 1998 IEEE International Conference on Evolutionary Computation Proceedings, 1998. IEEE World Congress on Computational Intelligence* , The 1998 IEEE International Conference on Evolutionary Computation Proceedings, 1998. IEEE World Congress on Computational Intelligence pp 69–73

[119] Holland J H 1992 *Adaptation in natural and artificial systems: an introductory analysis with applications to biology, control, and artificial intelligence* (Cambridge, Mass: MIT Press)

[120] Engelbrecht A P 2005 *Fundamentals of computational swarm intelligence* (Hoboken, NJ: Wiley)

[121] Reyes-sierra M and Coello C A C 2006 Multi-Objective particle swarm optimizers: A survey of the state-of-the-art *Int. J. Comput. INTELLIGENCE Res.* **2** 287–308

[122] Kennedy J 1999 Small worlds and mega-minds: effects of neighborhood topology on particle swarm performance *Proceedings of the 1999 Congress on Evolutionary Computation, 1999. CEC 99* Proceedings of the 1999 Congress on Evolutionary Computation, 1999. CEC 99 vol 3 p 1938 Vol. 3

[123] Kennedy J and Mendes R 2002 Population structure and particle swarm performance *Proceedings of the 2002 Congress on Evolutionary Computation, 2002. CEC '02* Proceedings of the 2002 Congress on Evolutionary Computation, 2002. CEC '02 vol 2 pp 1671–6

[124] Altman K W and Plonsey R 1990 Analysis of excitable cell activation: relative effects of external electrical stimuli *Med. Biol. Eng. Comput.* **28** 574–80

[125] Groppa S, Herzog J, Falk D, Riedel C, Deuschl G and Volkmann J 2014 Physiological and anatomical decomposition of subthalamic neurostimulation effects in essential tremor *Brain J. Neurol.* **137** 109–21

[126] Miocinovic S, Parent M, Butson C R, Hahn P J, Russo G S, Vitek J L and McIntyre C C 2006 Computational analysis of subthalamic nucleus and lenticular fasciculus activation during therapeutic deep brain stimulation *J Neurophysiol* **96** 1569–80

[127] Johnson M D and McIntyre C C 2008 Quantifying the neural elements activated and inhibited by globus pallidus deep brain stimulation *J. Neurophysiol.* **100** 2549–63

[128] Johnson M D, Zhang J, Ghosh D, McIntyre C C and Vitek J L 2012 Neural targets for relieving parkinsonian rigidity and bradykinesia with pallidal deep brain stimulation *J. Neurophysiol.* **108** 567–77

[129] Zitella L M, Teplitzky B A, Yager P, Hudson H M, Brintz K, Duchin Y, Harel N, Vitek J L, Baker K B and Johnson M D 2015 Subject-specific computational modeling of DBS in the PPTg area *Front. Comput. Neurosci.* **9** 93

[130] Butson C R, Cooper S E, Henderson J M and McIntyre C C 2007 Patient-specific analysis of the volume of tissue activated during deep brain stimulation *NeuroImage* **34** 661–70

[131] Frankemolle A M M, Wu J, Noecker A M, Voelcker-Rehage C, Ho J C, Vitek J L, McIntyre C C and Alberts J L 2010 Reversing cognitive–motor impairments in Parkinson's disease patients using a computational modelling approach to deep brain stimulation programming *Brain* **133** 746–61

[132] Ballanger B, van Eimeren T, Moro E, Lozano A M, Hamani C, Boulinguez P, Pellecchia G, Houle S, Poon Y Y, Lang A E and Strafella A P 2009 Stimulation of the subthalamic nucleus and impulsivity: release your horses *Ann. Neurol.* **66** 817–24

[133] Pollo C, Stieglitz L, Oertel M, Kaelin-Lang A and Schüpbach M 2013 Improved intraoperative therapeutic window with directional DBS compared to omnidirectional DBS using a novel lead design *J. Neurol. Sci.* **333** e79–80

[134] Bour L J, Verhagen R, Contarino F, Bie R M a D, Elswijk G V, Martens H C f, Munckhof P V den and Schuurman R 2013 A new DBS lead: Simultaneous 32-contact local field potential recording in the Parkinsonian Stn: 1264 *Mov. Disord.* **28**

[135] Connolly A T, Muralidharan A, Hendrix C, Johnson L, Gupta R, Stanslaski S, Denison T, Baker K B, Vitek J L and Johnson M D 2015 Local field potential recordings in a non-human primate model of Parkinsons disease using the Activa PC + S neurostimulator *J. Neural Eng.* **12** 066012

[136] Johnson M D, Lim H H, Netoff T I, Connolly A T, Johnson N, Roy A, Holt A, Lim K O, Carey J R, Vitek J L and He B 2013 Neuromodulation for brain disorders: challenges and opportunities *IEEE Trans. Biomed. Eng.* **60** 610–24

[137] Peña E, Zhang S, Deyo S, Xiao Y and Johnson M D 2017 Particle swarm optimization for programming deep brain stimulation arrays *J. Neural Eng.* **14** 016014

[138] Hoover J E and Strick P L 1993 Multiple output channels in the basal ganglia *Science* **259** 819–21

[139] Inase M, Tokuno H, Nambu A, Akazawa T and Takada M 1999 Corticostriatal and corticosubthalamic input zones from the presupplementary motor area in the macaque monkey: comparison with the input zones from the supplementary motor area *Brain Res.* **833** 191–201

[140] Nambu A, Takada M, Inase M and Tokuno H 1996 Dual somatotopical representations in the primate subthalamic nucleus: evidence for ordered but reversed body-map transformations from the primary motor cortex and the supplementary motor area *J. Neurosci. Off. J. Soc. Neurosci.* **16** 2671–83

[141] Parent A and Hazrati L N 1995 Functional anatomy of the basal ganglia. I. The cortico-basal ganglia-thalamo-cortical loop *Brain Res. Brain Res. Rev.* **20** 91–127

[142] Bevan M D, Magill P J, Terman D, Bolam J P and Wilson C J 2002 Move to the rhythm: oscillations in the subthalamic nucleus-external globus pallidus network *Trends Neurosci.* **25** 525–31

[143] Brown P, Oliviero A, Mazzone P, Insola A, Tonali P and Di Lazzaro V 2001 Dopamine dependency of oscillations between subthalamic nucleus and pallidum in Parkinson's disease *J. Neurosci. Off. J. Soc. Neurosci.* **21** 1033–8

[144] Foffani G, Priori A, Egidi M, Rampini P, Tamma F, Caputo E, Moxon K A, Cerutti S and Barbieri S 2003 300-Hz subthalamic oscillations in Parkinson's disease *Brain J. Neurol.* **126** 2153–63

[145] Levy R, Ashby P, Hutchison W D, Lang A E, Lozano A M and Dostrovsky J O 2002 Dependence of subthalamic nucleus oscillations on movement and dopamine in Parkinson's disease *Brain* **125** 1196–209

[146] Mallet N, Pogosyan A, Márton L F, Bolam J P, Brown P and Magill P J 2008 Parkinsonian beta oscillations in the external globus pallidus and their relationship with subthalamic nucleus activity *J. Neurosci. Off. J. Soc. Neurosci.* **28** 14245–58

[147] Moran A, Bergman H, Israel Z and Bar-Gad I 2008 Subthalamic nucleus functional organization revealed by parkinsonian neuronal oscillations and synchrony *Brain* **131** 3395–409

[148] Plenz D and Kital S T 1999 A basal ganglia pacemaker formed by the subthalamic nucleus and external globus pallidus *Nature* **400** 677–82

[149] Shimamoto S A, Ryapolova-Webb E S, Ostrem J L, Galifianakis N B, Miller K J and Starr P A 2013 Subthalamic nucleus neurons are synchronized to primary motor cortex local field potentials in Parkinson's disease *J. Neurosci. Off. J. Soc. Neurosci.* **33** 7220–33

[150] Gradinaru V, Mogri M, Thompson K R, Henderson J M and Deisseroth K 2009 Optical deconstruction of parkinsonian neural circuitry *Science* **324** 354–9

[151] Johnson M D, Miocinovic S, McIntyre C C and Vitek J L 2008 Mechanisms and Targets of Deep Brain Stimulation in Movement Disorders *Neurotherapeutics* **5** 294–308

[152] Kravitz A V, Freeze B S, Parker P R L, Kay K, Thwin M T, Deisseroth K and Kreitzer A C 2010 Regulation of parkinsonian motor behaviours by optogenetic control of basal ganglia circuitry *Nature* **466** 622–6

[153] Mallet L, Schüpbach M, N'Diaye K, Remy P, Bardinet E, Czernecki V, Welter M-L, Pelissolo A, Ruberg M, Agid Y and Yelnik J 2007 Stimulation of subterritories of the subthalamic nucleus reveals its role in the integration of the emotional and motor aspects of behavior *Proc. Natl. Acad. Sci. U. S. A.* **104** 10661–6

[154] Miocinovic S, Parent M, Butson C R, Hahn P J, Russo G S, Vitek J L and McIntyre C C 2006 Computational analysis of subthalamic nucleus and lenticular fasciculus activation during therapeutic deep brain stimulation *J Neurophysiol* **96** 1569–80

[155] Zaidel A, Spivak A, Shpigelman L, Bergman H and Israel Z 2009 Delimiting subterritories of the human subthalamic nucleus by means of microelectrode recordings and a Hidden Markov Model *Mov. Disord.* **24** 1785–93

[156] Zhang J, Wang Z I, Baker K B and Vitek J L 2012 Effect of globus pallidus internus stimulation on neuronal activity in the pedunculopontine tegmental nucleus in the primate model of Parkinson's disease *Exp. Neurol.* **233** 575–80

[157] Moore J and Chapman R Application of Particle Swarm to Multiobjective Optimization

[158] Obeso J A, Rodriguez-Oroz M C, Rodriguez M, Lanciego J L, Artieda J, Gonzalo N and Olanow C W 2000 Pathophysiology of the basal ganglia in Parkinson's disease *Trends Neurosci.* **23** S8–19

[159] Coenen V A, Prescher A, Schmidt T, Picozzi P and Gielen F L H 2008 What is dorso-lateral in the subthalamic Nucleus (STN)?--a topographic and anatomical consideration on the ambiguous description of today's primary target for deep brain stimulation (DBS) surgery *Acta Neurochir. (Wien)* **150** 1163–1165; discussion 1165

[160] Johnson D 2016 Development of a Python-based, Open-Source Stereotactic Neurosurgical Planning Software Tool

[161] Duchin Y, Abosch A, Yacoub E, Sapiro G and Harel N 2012 Feasibility of Using Ultra-High Field (7 T) MRI for Clinical Surgical Targeting *PLOS ONE* **7** e37328

[162] Morel A 2007 *Stereotactic Atlas of the Human Thalamus and Basal Ganglia* (New York: CRC Press)

[163] George P, Huang X-F, Petrides M and Toga A 2009 *The Rhesus monkey brain : in stereotaxic coordinates* (San Diego, California, USA: Academic Press)

[164] Schmahmann J and Pandya D 2009 *Fiber Pathways of the Brain* (Oxford, New York: Oxford University Press)

[165] Johnson M D and McIntyre C C 2008 Quantifying the Neural Elements Activated and Inhibited by Globus Pallidus Deep Brain Stimulation *J. Neurophysiol.* **100** 2549–63

[166] Miocinovic S, Noecker A M, Maks C B, Butson C R and McIntyre C C 2007 Cicerone: stereotactic neurophysiological recording and deep brain stimulation electrode placement software system *Acta Neurochir. Suppl.* **97** 561–7

[167] Kamiya K, Hori M, Miyajima M, Nakajima M, Suzuki Y, Kamagata K, Suzuki M, Arai H, Ohtomo K and Aoki S 2014 Axon Diameter and Intra-Axonal Volume Fraction of the Corticospinal Tract in Idiopathic Normal Pressure Hydrocephalus Measured by Q-Space Imaging *PLOS ONE* **9** e103842

[168] Gabriel S, Lau R W and Gabriel C 1996 The dielectric properties of biological tissues: III. Parametric models for the dielectric spectrum of tissues *Phys. Med. Biol.* **41** 2271

[169] Baumann S B, Wozny D R, Kelly S K and Meno F M 1997 The electrical conductivity of human cerebrospinal fluid at body temperature *IEEE Trans. Biomed. Eng.* **44** 220–3

[170] Rattay F 1989 Analysis of models for extracellular fiber stimulation *IEEE Trans. Biomed. Eng.* **36** 676–82

[171] Cogan S F, Ludwig K A, Welle C G and Takmakov P 2016 Tissue damage thresholds during therapeutic electrical stimulation *J. Neural Eng.* **13** 021001

[172] Slopsema J P 2016 Directional axonal activation for deep brain stimulation applications

[173] Lehto L J, Slopsema J P, Johnson M D, Shatillo A, Teplitzky B A, Lynn Utecht, Adriany G, Mangia S, Sierra A, Low W C, Gröhn O and Michaeli S 2017 Orientation selective deep brain stimulation *J. Neural Eng.* **14** 016016

[174] Parent M and Parent A 2004 The pallidofugal motor fiber system in primates *Parkinsonism Relat. Disord.* **10** 203–11

[175] Bejjani B-P, Damier P, Arnulf I, Papadopoulos S, Bonnet A-M, Vidailhet M, Agid Y, Pidoux B, Cornu P, Dormont D and Marsault C 1998 Deep brain stimulation in Parkinson's disease: Opposite effects of stimulation in the pallidum *Mov. Disord.* **13** 969–70

[176] Fytagoridis A, Åström M, Wårdell K and Blomstedt P 2013 Stimulation-induced side effects in the posterior subthalamic area: Distribution, characteristics and visualization *Clin. Neurol. Neurosurg.* **115** 65–71

[177] Krack P, Pollak P, Limousin P, Hoffmann D, Benazzouz A, Le Bas J F, Koudsie A and Benabid A L 1998 Opposite motor effects of pallidal stimulation in Parkinson's disease *Ann. Neurol.* **43** 180–92

[178] Xu W, Miocinovic S, Zhang J, Baker K B, McIntyre C C and Vitek J L 2011 Dissociation of motor symptoms during deep brain stimulation of the subthalamic nucleus in the region of the internal capsule *Exp. Neurol.* **228** 294–7

[179] Yelnik J, Damier P, Bejjani B P, Francois C, Gervais D, Dormont D, Arnulf I, M. Bonnet A, Cornu P, Pidoux B and Agid Y 2000 Functional mapping of the human globus pallidus: contrasting effect of stimulation in the internal and external pallidum in Parkinson's disease *Neuroscience* **101** 77–87

[180] Huang H, Watts R L and Montgomery E B 2014 Effects of deep brain stimulation frequency on bradykinesia of Parkinson's disease *Mov. Disord.* **29** 203–6

[181] Vitek J L, Zhang J, Hashimoto T, Russo G S and Baker K B 2012 External pallidal stimulation improves parkinsonian motor signs and modulates neuronal activity throughout the basal ganglia thalamic network *Exp. Neurol.* **233** 581–6

[182] Nandi D, Jenkinson N, Stein J and Aziz T 2008 The pedunculopontine nucleus in Parkinson's disease: primate studies *Br. J. Neurosurg.* **22** 4–8

[183] Pahapill P A and Lozano A M 2000 The pedunculopontine nucleus and Parkinson's disease *Brain* **123** 1767–83

[184] Karachi C, Grabli D, Bernard F A, Tandé D, Wattiez N, Belaid H, Bardinet E, Prigent A, Nothacker H-P, Hunot S, Hartmann A, Lehéricy S, Hirsch E C and François C 2010 Cholinergic mesencephalic neurons are involved in gait and postural disorders in Parkinson disease *J. Clin. Invest.* **120** 2745–54

[185] Parihar R, Alterman R, Papavassiliou E, Tarsy D and Shih L C 2015 Comparison of VIM and STN DBS for Parkinsonian Resting and Postural/Action Tremor *Tremor Hyperkinetic Mov.* **5**

[186] Smulders K, Dale M L, Carlson-Kuhta P, Nutt J G and Horak F B 2016 Pharmacological treatment in Parkinson's disease: Effects on gait *Parkinsonism Relat. Disord.* **31** 3–13

[187] Bohnen N I, Albin R L, Müller M L T . and Chou K 2011 Advances in Therapeutic Options for Gait and Balance in Parkinson's Disease *US Neurol.* **7** 100–8

[188] Uebelacker L A, Epstein-Lubow G, Lewis T, Broughton M K and Friedman J H 2014 A Survey of Parkinson's Disease Patients: Most Bothersome Symptoms and Coping Preferences *J. Park. Dis.* **4** 717–23

[189] Gómez-Esteban J C, Zarranz J J, Lezcano E, Tijero B, Luna A, Velasco F, Rouco I and Garamendi I 2007 Influence of Motor Symptoms upon the Quality of Life of Patients with Parkinson's Disease *Eur. Neurol.* **57** 161–5

[190] Kemoun G and Defebvre L 2001 Gait disorders in Parkinson disease. Clinical description, analysis of posture, initiation of stabilized gait *Presse Medicale Paris Fr. 1983* **30** 452—459

[191] Hausdorff J M, Cudkowicz M E, Firtion R, Wei J Y and Goldberger A L 1998 Gait variability and basal ganglia disorders: Stride-to-stride variations of gait cycle timing in parkinson's disease and Huntington's disease *Mov. Disord.* **13** 428–37

[192] Schaafsma J D, Giladi N, Balash Y, Bartels A L, Gurevich T and Hausdorff J M 2003 Gait dynamics in Parkinson's disease: relationship to Parkinsonian features, falls and response to levodopa *J. Neurol. Sci.* **212** 47–53

[193] Okuma Y 2014 Freezing of gait and falls in Parkinson's disease *J. Park. Dis.* **4** 255–60

[194] Grabli D, Karachi C, Folgoas E, Monfort M, Tande D, Clark S, Civelli O, Hirsch E C and François C 2013 Gait Disorders in Parkinsonian Monkeys with Pedunculopontine Nucleus Lesions: A Tale of Two Systems *J. Neurosci.* **33** 11986–93

[195] Roper J A, Kang N, Ben J, Cauraugh J H, Okun M S and Hass C J 2016 Deep brain stimulation improves gait velocity in Parkinson's disease: a systematic review and meta-analysis *J. Neurol.* **263** 1195–203

[196] Beuter A and Modolo J 2009 Delayed and lasting effects of deep brain stimulation on locomotion in Parkinson's disease *Chaos Interdiscip. J. Nonlinear Sci.* **19** 026114

[197] Graf von Keyserlingk D and Schramm U 1984 Diameter of axons and thickness of myelin sheaths of the pyramidal tract fibres in the adult human medullary pyramid *Anat. Anz.* **157** 97–111

[198] Ashby P, Kim Y J, Kumar R, Lang A E and Lozano A M 1999 Neurophysiological effects of stimulation through electrodes in the human subthalamic nucleus *Brain J. Neurol.* **122 (Pt 10)** 1919–31

[199] Baker K B, Montgomery E B, Rezai A R, Burgess R and Lüders H O 2002 Subthalamic nucleus deep brain stimulus evoked potentials: physiological and therapeutic implications *Mov. Disord. Off. J. Mov. Disord. Soc.* **17** 969–83

[200] Costa J, Valls-Solé J, Valldeoriola F, Rumià J and Tolosa E 2007 Motor responses of muscles supplied by cranial nerves to subthalamic nucleus deep brain stimuli *Brain J. Neurol.* **130** 245–55

[201] MacKinnon C D, Webb R M, Silberstein P, Tisch S, Asselman P, Limousin P and Rothwell J C 2005 Stimulation through electrodes implanted near the subthalamic nucleus activates projections to motor areas of cerebral cortex in patients with Parkinson's disease *Eur. J. Neurosci.* **21** 1394–402

[202] Tommasi G, Krack P, Fraix V, Le Bas J-F, Chabardes S, Benabid A-L and Pollak P 2008 Pyramidal tract side effects induced by deep brain stimulation of the subthalamic nucleus *J. Neurol. Neurosurg. Psychiatry* **79** 813–9

[203] Little S, Pogosyan A, Neal S, Zavala B, Zrinzo L, Hariz M, Foltynie T, Limousin P, Ashkan K, FitzGerald J, Green A L, Aziz T Z and Brown P 2013 Adaptive deep brain stimulation in advanced Parkinson disease *Ann. Neurol.* **74** 449–57

[204] Little S, Beudel M, Zrinzo L, Foltynie T, Limousin P, Hariz M, Neal S, Cheeran B, Cagnan H, Gratwicke J, Aziz T Z, Pogosyan A and Brown P 2016 Bilateral adaptive deep brain stimulation is effective in Parkinson's disease *J. Neurol. Neurosurg. Psychiatry* **87** 717–21

[205] Herron J A, Thompson M C, Brown T, Chizeck H J, Ojemann J G and Ko A L 2016 Chronic electrocorticography for sensing movement intention and closed-loop deep brain stimulation with wearable sensors in an essential tremor patient *J. Neurosurg.* 1–8

[206] Lindén H, Tetzlaff T, Potjans T C, Pettersen K H, Grün S, Diesmann M and Einevoll G T 2011 Modeling the spatial reach of the LFP *Neuron* **72** 859–72

[207] Zaidel A, Spivak A, Grieb B, Bergman H and Israel Z 2010 Subthalamic span of beta oscillations predicts deep brain stimulation efficacy for patients with Parkinson's disease *Brain J. Neurol.* **133** 2007–21

[208] Berke J D, Okatan M, Skurski J and Eichenbaum H B 2004 Oscillatory entrainment of striatal neurons in freely moving rats *Neuron* **43** 883–96

[209] Connolly A T, Jensen A L, Bello E M, Netoff T I, Baker K B, Johnson M D and Vitek J L 2015 Modulations in oscillatory frequency and coupling in globus pallidus with increasing parkinsonian severity *J. Neurosci. Off. J. Soc. Neurosci.* **35** 6231–40

[210] Courtemanche R, Fujii N and Graybiel A M 2003 Synchronous, focally modulated beta-band oscillations characterize local field potential activity in the striatum of awake behaving monkeys *J. Neurosci. Off. J. Soc. Neurosci.* **23** 11741–52

[211] Jensen O, Goel P, Kopell N, Pohja M, Hari R and Ermentrout B 2005 On the human sensorimotor-cortex beta rhythm: sources and modeling *NeuroImage* **26** 347–55

[212] Leventhal D K, Gage G J, Schmidt R, Pettibone J R, Case A C and Berke J D 2012 Basal ganglia beta oscillations accompany cue utilization *Neuron* **73** 523–36

[213] Murthy V N and Fetz E E 1992 Coherent 25- to 35-Hz oscillations in the sensorimotor cortex of awake behaving monkeys. *Proc. Natl. Acad. Sci. U. S. A.* **89** 5670–4

[214] Bour L J, Lourens M A J, Verhagen R, de Bie R M A, van den Munckhof P, Schuurman P R and Contarino M F 2015 Directional Recording of Subthalamic Spectral Power Densities in Parkinson's Disease and the Effect of Steering Deep Brain Stimulation *Brain Stimulat.* **8** 730–41

[215] Bergman H, Wichmann T, Karmon B and DeLong M R 1994 The primate subthalamic nucleus. II. Neuronal activity in the MPTP model of parkinsonism *J. Neurophysiol.* **72** 507–20

[216] Brown P 2007 Abnormal oscillatory synchronisation in the motor system leads to impaired movement *Curr. Opin. Neurobiol.* **17** 656–64

[217] de Solages C, Hill B C, Koop M M, Henderson J M and Bronte-Stewart H 2010 Bilateral symmetry and coherence of subthalamic nuclei beta band activity in Parkinson's disease *Exp. Neurol.* **221** 260–6

[218] Kühn A A, Trottenberg T, Kivi A, Kupsch A, Schneider G-H and Brown P 2005 The relationship between local field potential and neuronal discharge in the subthalamic nucleus of patients with Parkinson's disease *Exp. Neurol.* **194** 212–20

[219] Rosa M, Giannicola G, Servello D, Marceglia S, Pacchetti C, Porta M, Sassi M, Scelzo E, Barbieri S and Priori A 2011 Subthalamic local field beta oscillations during ongoing deep brain stimulation in Parkinson's disease in hyperacute and chronic phases *Neurosignals* **19** 151–62

[220] Wichmann T and DeLong M R 2003 Pathophysiology of Parkinson's disease: the MPTP primate model of the human disorder *Ann. N. Y. Acad. Sci.* **991** 199–213

[221] Goldberg J A, Rokni U, Boraud T, Vaadia E and Bergman H 2004 Spike synchronization in the cortex/basal-ganglia networks of Parkinsonian primates reflects global dynamics of the local field potentials *J. Neurosci. Off. J. Soc. Neurosci.* **24** 6003–10

[222] Devergnas A, Pittard D, Bliwise D and Wichmann T 2014 Relationship between oscillatory activity in the cortico-basal ganglia network and parkinsonism in MPTP-treated monkeys *Neurobiol. Dis.* **68** 156–66

[223] Leblois A, Meissner W, Bioulac B, Gross C E, Hansel D and Boraud T 2007 Late emergence of synchronized oscillatory activity in the pallidum during progressive parkinsonism *Eur. J. Neurosci.* **26** 1701–13

[224] Marmor O, Valsky D, Joshua M, Bick A S, Arkadir D, Tamir I, Bergman H, Israel Z and Eitan R 2017 Local vs. volume conductance activity of field potentials in the human subthalamic nucleus *J. Neurophysiol.* **117** 2140–51

[225] Nunez P L and Srinivasan R 2006 *Electric Fields of the Brain: The Neurophysics of EEG* (Oxford University Press)

[226] Lambert C, Zrinzo L, Nagy Z, Lutti A, Hariz M, Foltynie T, Draganski B, Ashburner J and Frackowiak R 2012 Confirmation of functional zones within the

human subthalamic nucleus: patterns of connectivity and sub-parcellation using diffusion weighted imaging *NeuroImage* **60** 83–94

[227] Draganski B, Kherif F, Klöppel S, Cook P A, Alexander D C, Parker G J M, Deichmann R, Ashburner J and Frackowiak R S J 2008 Evidence for Segregated and Integrative Connectivity Patterns in the Human Basal Ganglia *J. Neurosci.* **28** 7143–52

[228] Lehéricy S, Ducros M, Van de Moortele P-F, Francois C, Thivard L, Poupon C, Swindale N, Ugurbil K and Kim D-S 2004 Diffusion tensor fiber tracking shows distinct corticostriatal circuits in humans *Ann. Neurol.* **55** 522–9

[229] Langston J W, Forno L S, Rebert C S and Irwin I 1984 Selective nigral toxicity after systemic administration of 1-methyl-4-phenyl-1,2,5,6-tetrahydropyrine (MPTP) in the squirrel monkey *Brain Res.* **292** 390–4

[230] Karachi C, Grabli D, Bernard F A, Tandé D, Wattiez N, Belaid H, Bardinet E, Prigent A, Nothacker H-P, Hunot S, Hartmann A, Lehéricy S, Hirsch E C and François C 2010 Cholinergic mesencephalic neurons are involved in gait and postural disorders in Parkinson disease *J. Clin. Invest.* **120** 2745–54

[231] Villalba R M, Wichmann T and Smith Y 2014 Neuronal loss in the caudal intralaminar thalamic nuclei in a primate model of Parkinson's disease *Brain Struct. Funct.* **219**

[232] Bokil H, Andrews P, Kulkarni J E, Mehta S and Mitra P P 2010 Chronux: a platform for analyzing neural signals *J. Neurosci. Methods* **192** 146–51

[233] Donnelly N A, Holtzman T, Rich P D, Nevado-Holgado A J, Fernando A B P, Dijck G V, Holzhammer T, Paul O, Ruther P, Paulsen O, Robbins T W and Dalley J W 2014 Oscillatory Activity in the Medial Prefrontal Cortex and Nucleus Accumbens Correlates with Impulsivity and Reward Outcome *PLOS ONE* **9** e111300

[234] Elder C M, Hashimoto T, Zhang J and Vitek J L 2005 Chronic implantation of deep brain stimulation leads in animal models of neurological disorders *J. Neurosci. Methods* **142** 11–6

[235] Nambu A, Tokuno H, Inase M and Takada M 1997 Corticosubthalamic input zones from forelimb representations of the dorsal and ventral divisions of the premotor cortex in the macaque monkey: comparison with the input zones from the primary motor cortex and the supplementary motor area *Neurosci. Lett.* **239** 13–6

[236] Parent A and Hazrati L N 1995 Functional anatomy of the basal ganglia. II. The place of subthalamic nucleus and external pallidum in basal ganglia circuitry *Brain Res. Brain Res. Rev.* **20** 128–54

[237] Meissner W, Ravenscroft P, Reese R, Harnack D, Morgenstern R, Kupsch A, Klitgaard H, Bioulac B, Gross C E, Bezard E and Boraud T 2006 Increased slow oscillatory activity in substantia nigra pars reticulata triggers abnormal involuntary movements in the 6-OHDA-lesioned rat in the presence of excessive extracelullar striatal dopamine *Neurobiol. Dis.* **22** 586–98

[238] Kolb R, Abosch A, Felsen G and Thompson J A 2017 Use of intraoperative local field potential spectral analysis to differentiate basal ganglia structures in Parkinson9s disease patients *Physiol. Rep.* **5** e13322

[239] Kühn A A, Williams D, Kupsch A, Limousin P, Hariz M, Schneider G-H, Yarrow K and Brown P 2004 Event-related beta desynchronization in human subthalamic nucleus correlates with motor performance *Brain* **127** 735–46

[240] Doyle L M F, Kühn A A, Hariz M, Kupsch A, Schneider G-H and Brown P 2005 Levodopa-induced modulation of subthalamic beta oscillations during self-paced movements in patients with Parkinson's disease *Eur. J. Neurosci.* **21** 1403–12

[241] Levy R, Ashby P, Hutchison W D, Lang A E, Lozano A M and Dostrovsky J O 2002 Dependence of subthalamic nucleus oscillations on movement and dopamine in Parkinson's disease *Brain J. Neurol.* **125** 1196–209

[242] Alegre M, Alonso-Frech F, Rodríguez-Oroz M C, Guridi J, Zamarbide I, Valencia M, Manrique M, Obeso J A and Artieda J 2005 Movement-related changes in oscillatory activity in the human subthalamic nucleus: ipsilateral vs. contralateral movements *Eur. J. Neurosci.* **22** 2315–24

[243] Williams D, Kühn A, Kupsch A, Tijssen M, van Bruggen G, Speelman H, Hotton G, Yarrow K and Brown P 2003 Behavioural cues are associated with modulations of synchronous oscillations in the human subthalamic nucleus *Brain* **126** 1975–85

[244] Brown P 2003 Oscillatory nature of human basal ganglia activity: relationship to the pathophysiology of Parkinson's disease *Mov. Disord. Off. J. Mov. Disord. Soc.* **18** 357–63

[245] Murthy V N and Fetz E E 1996 Oscillatory activity in sensorimotor cortex of awake monkeys: synchronization of local field potentials and relation to behavior *J. Neurophysiol.* **76** 3949–67

[246] Sanes J N and Donoghue J P 1993 Oscillations in Local Field Potentials of the Primate Motor Cortex During Voluntary Movement *Proc. Natl. Acad. Sci. U. S. A.* **90** 4470–4

[247] Grill W M and Mortimer J T 1994 Electrical properties of implant encapsulation tissue *Ann. Biomed. Eng.* **22** 23–33

[248] Johnson M D, Otto K J and Kipke D R 2005 Repeated voltage biasing improves unit recordings by reducing resistive tissue impedances *IEEE Trans. Neural Syst. Rehabil. Eng.* **13** 160–5

[249] Williams J C, Hippensteel J A, Dilgen J, Shain W and Kipke D R 2007 Complex impedance spectroscopy for monitoring tissue responses to inserted neural implants *J. Neural Eng.* **4** 410–23

[250] Xu J, Shepherd R K, Millard R E and Clark G M 1997 Chronic electrical stimulation of the auditory nerve at high stimulus rates: a physiological and histopathological study *Hear. Res.* **105** 1–29

[251] Haberler C, Alesch F, Mazal P R, Pilz P, Jellinger K, Pinter M M, Hainfellner J A and Budka H 2000 No tissue damage by chronic deep brain stimulation in Parkinson's disease *Ann. Neurol.* **48** 372–6

[252] Szarowski D H, Andersen M D, Retterer S, Spence A J, Isaacson M, Craighead H G, Turner J N and Shain W 2003 Brain responses to micro-machined silicon devices *Brain Res.* **983** 23–35

[253] Moss J, Ryder T, Aziz T Z, Graeber M B and Bain P G 2004 Electron microscopy of tissue adherent to explanted electrodes in dystonia and Parkinson's disease *Brain J. Neurol.* **127** 2755–63

[254] Biran R, Martin D C and Tresco P A 2005 Neuronal cell loss accompanies the brain tissue response to chronically implanted silicon microelectrode arrays *Exp. Neurol.* **195** 115–26

[255] Otto K J, Johnson M D and Kipke D R 2006 Voltage pulses change neural interface properties and improve unit recordings with chronically implanted microelectrodes *IEEE Trans. Biomed. Eng.* **53** 333–40

[256] Kappenman E S and Luck S J 2010 The Effects of Electrode Impedance on Data Quality and Statistical Significance in ERP Recordings *Psychophysiology* **47** 888–904

[257] Rolston J D, Englot D J, Starr P A and Larson P S 2016 An unexpectedly high rate of revisions and removals in deep brain stimulation surgery: Analysis of multiple databases *Parkinsonism Relat. Disord.* **33** 72–7

[258] Bronte-Stewart H, Barberini C, Koop M M, Hill B C, Henderson J M and Wingeier B 2009 The STN beta-band profile in Parkinson's disease is stationary and shows prolonged attenuation after deep brain stimulation *Exp. Neurol.* **215** 20–8

[259] Kühn A A, Tsui A, Aziz T, Ray N, Brücke C, Kupsch A, Schneider G-H and Brown P 2009 Pathological synchronisation in the subthalamic nucleus of patients with Parkinson's disease relates to both bradykinesia and rigidity *Exp. Neurol.* **215** 380–7

[260] Priori A, Foffani G, Pesenti A, Bianchi A, Chiesa V, Baselli G, Caputo E, Tamma F, Rampini P, Egidi M, Locatelli M, Barbieri S and Scarlato G 2002 Movement-related modulation of neural activity in human basal ganglia and its L-DOPA dependency: recordings from deep brain stimulation electrodes in patients with Parkinson's disease *Neurol. Sci. Off. J. Ital. Neurol. Soc. Ital. Soc. Clin. Neurophysiol.* **23 Suppl 2** S101-102

[261] Brown P, Mazzone P, Oliviero A, Altibrandi M G, Pilato F, Tonali P A and Di Lazzaro V 2004 Effects of stimulation of the subthalamic area on oscillatory pallidal activity in Parkinson's disease *Exp. Neurol.* **188** 480–90

[262] Kühn A A, Kempf F, Brücke C, Gaynor Doyle L, Martinez-Torres I, Pogosyan A, Trottenberg T, Kupsch A, Schneider G-H, Hariz M I, Vandenberghe W, Nuttin B and Brown P 2008 High-frequency stimulation of the subthalamic nucleus suppresses oscillatory beta activity in patients with Parkinson's disease in parallel with improvement in motor performance *J. Neurosci. Off. J. Soc. Neurosci.* **28** 6165–73

[263] Silberstein P, Kühn A A, Kupsch A, Trottenberg T, Krauss J K, Wöhrle J C, Mazzone P, Insola A, Di Lazzaro V, Oliviero A, Aziz T and Brown P 2003 Patterning of globus pallidus local field potentials differs between Parkinson's disease and dystonia *Brain J. Neurol.* **126** 2597–608

[264] Wingeier B, Tcheng T, Koop M M, Hill B C, Heit G and Bronte-Stewart H M 2006 Intra-operative STN DBS attenuates the prominent beta rhythm in the STN in Parkinson's disease *Exp. Neurol.* **197** 244–51

[265] Eusebio A, Thevathasan W, Doyle Gaynor L, Pogosyan A, Bye E, Foltynie T, Zrinzo L, Ashkan K, Aziz T and Brown P 2011 Deep brain stimulation can suppress pathological synchronisation in parkinsonian patients *J. Neurol. Neurosurg. Psychiatry* **82** 569–73